Doctoral School in Environmental Engineering

A new Lagrangian method for transport in porous media

(to model chemotaxis in porous media)

Avesani Diego

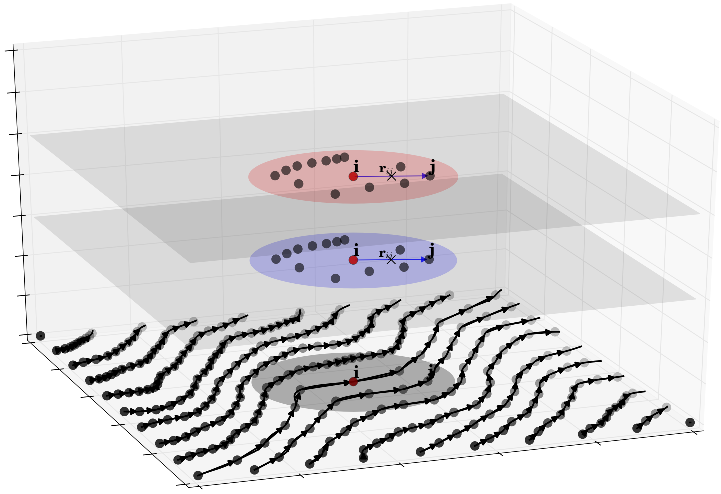

UNIVERSITÀ DEGLI STUDI DI TRENTO
Dipartimento di Ingegneria Civile,
Ambientale e Meccanica

2014

Doctoral thesis in **Environmental Engineering** (XXV cycle)
Department of Civil, Environmental and Mechanical Engineering, **University of Trento**
Year: **2014**
Supervisors: **Prof. Alberto Bellin, Prof. Michael Dumbser**

On the cover: MWSPH scheme snapshot
Università degli Studi di Trento, Italy
Trento, Italy
2014

A Chiara
Alla Vigolana
Al Bondone
Alla Paganella
08 Marzo 2014

That is the exploration that awaits you;
not mapping stars and studying nebulae,
but charting the unknown possibilities of existence
(Star Trek, All Good Things...)

Abstract- *As recently shown in laboratory bench scale experiments, chemotaxis, i.e. the movement of microorganisms toward or away from the concentration gradient of a chemical species, could have a fundamental role in the transport of bacteria through saturated porous media. Chemotactic bacteria could enhance bioremediation by directing their own motions to residual contaminants in less conductive zones in aquifers. The aim of the present work is to develop a proper numerical scheme to define and to quantify the magnitude and the role of chemotaxis in the complex groundwater system framework.*

We present a new class of meshless Lagrangian particle methods based on the Smooth Particle Hydrodinamics (SPH) formulation of Vila & Ben Moussa, combined with a new Weighted Essentially Non-Oscillatory (WENO) reconstruction technique on moving point clouds in multiple space dimensions. The purpose of this new scheme is to fully exploit the advantages of SPH among traditional meshbased and meshfree schemes and to overcome its inapplicability for modeling chemotaxis in porous media.

The key idea is to produce for each particle first a set of high order accurate Moving Least Squares (MLS) reconstructions on a set of different reconstruction stencils. Then, these reconstructions are combined with each other using a nonlinear WENO technique in order to capture at the same time discontinuities and to maintain accuracy and low numerical dissipation in smooth regions. The numerical fluxes between interacting particles are subsequently evaluated using this MLS-WENO reconstruction at the midpoint between two particles, in combination with a Riemann solver that provides the necessary stabilization of the scheme based on the underlying physics of the governing equations. We propose the use of two different Riemann solvers: the Rusanov flux and an Osher-type flux. The use of monotone fluxes together with a WENO reconstruction ensures accuracy, stability, robustness and an essentially non oscillatory solution without the artificial viscosity term usually employed in conventional SPH schemes. To our knowledge, this is the first time that the WENO method, which has originally been developed for mesh-based schemes in the Eulerian framework on fixed grids, is extended to meshfree Lagrangian particle methods like SPH in multiple space dimensions.

In the first part, we test the new algorithm on two dimensional blast wave problems and on the classical one-dimensional Sod shock tube problem for the Euler equations of compressible gas dynamics. We obtain a good agreement with the exact or numerical reference solution in all cases and an improved accuracy and robustness compared to existing standard SPH schemes.

In the second part, the new SPH scheme is applied to advection-diffusion equation in heterogeneous porous media with anisotropic diffusion tensor. Several numerical test case shows that the new scheme is accurate. Unlike standard SPH, it reduces the occurrence of negative concentration.

In the third part, we show the applicability of the new scheme for modeling chemotaxis in porous media. We test the new scheme against analytical reference solutions. Under the assumption of complete mixing at the Darcy scale, we perform different two-dimensional conservative solute transport simulations under steady-state conditions with instant injection showing that chemotaxis significantly affect the quantification of field-scale mixing processes.

Contents

1 Introduction 1

1.1 Mathematical model 4

1.2 Numerical model 6

1.3 Objectives 8

1.4 Organization 8

2 A New Class of Moving-Least-Squares WENO-SPH Schemes 11

2.1 Governing equations 14

2.2 SPH formulations 15

2.2.1 The standard SPH formulation 15

2.2.2 The SPH formulation of Vila and Ben Moussa 17

2.2.3 Numerical Fluxes 18

2.3 Moving-Least-Squares WENO reconstruction 22

2.4 Numerical Test Cases 27

2.4.1 Assessment of the MLS-WENO reconstruction 27

2.4.1.1 Reconstruction of a smooth function 28

2.4.1.2 Reconstruction of a piecewise smooth function 33

2.4.2 Circular blast wave problems 37

2.4.3 1D Sod shock tube problem 59

2.5 Conclusions 61

3 MWSPH schemes for Advection Diffusion transport in porous media 63

3.1 Smooth Particle Hydrodynamics 65

3.1.1 Monaghan's formulation 65

    3.1.2 The MWSPH formulation of advection-diffusion equation 66
  3.2 Moving-Least-Square and WENO fluxes reconstruction 67
  3.3 Gradient reconstruction 71
    3.3.1 Smooth case 72
    3.3.2 Piecewise smooth test case with discontinuity 78
  3.4 Test case 82
    3.4.1 Homogeneous 82
    3.4.2 Heterogeneous 92
  3.5 Conclusion 98

4 An alternative SPH formulation to model chemotaxis in porous media 99
  4.1 Mathematical Modeling 101
  4.2 SPH formulation 103
  4.3 The new SPH approach 108
  4.4 Test cases 112
    4.4.1 1D chemotaxis test case 112
    4.4.2 2D diffusion chemotaxis 116
    4.4.3 2D advection-diffusion chemotaxis 120
      4.4.3.1 2D advection-diffusion chemotaxis, case 2 126
  4.5 Conclusion 128

5 Conclusion 129

Bibliography 131

Acknowledgments 148

List of Figures

1.1 Aggregation of chemotactic bacteria in regions of high attractant concentration as originally shown by *Pfeffer* [1887]. 2

1.2 Chemotatic velocity for different attractant concentrations and attractant gradients according to *Rivero et al.* [1989]'s formulation. 3

1.3 Spatial concentration distribution at dimensionless for $Pe = \infty$. TVD solver (top), HMOC solver (middle), and SPH (bottom). Courtesy of *Herrera et al.* [2009] 7

2.1 Examples of central reconstruction stencils S_0^i and S_0^j for a generic pair of interacting particles $\mathcal{P}_i$ and $\mathcal{P}_j$ (left). One-dimensional cut through the reconstruction polynomials $Q_i(\mathbf{r})$ and $Q_j(\mathbf{r})$ along the line connecting $\mathcal{P}_i$ and $\mathcal{P}_j$, as well as the states Q_{ij}^- and Q_{ij}^+ extrapolated to the midpoint $\bar{\mathbf{r}}_{ij}$ between the interacting particles (right). 21

2.2 Sketch of the central and one-sided WENO reconstruction stencils for a random particle distribution. The particle $\mathcal{P}_i$ is shown in red color. 26

2.3 Equidistant particle distribution on the left panel and non-equidistant particle distribution on the right panel. Particles are in black. The regular Cartesian lattice used for verification of the reconstruction is shown in red. 28

2.4 Comparison of the exact function and the reconstruction for the smooth case computed with standard SPH and with the new MLS-WENO. Particle values on computational domain with equidistant distribution **(a)** and non-equidistant distribution **(b)**. Cut through the reconstruction at $y = 0$ for equidistant particles **(c)** and non-equidistant particles **(d)**. 32

2.5 Comparison of the exact function and the reconstruction for the piecewise smooth case computed with standard SPH and with the new MLS-WENO. Particle values on computational domain with equidistant distribution **(a)** and non-equidistant distribution **(b)**. Cut through the reconstruction at $y = 0$ for equidistant particles **(c)** and non-equidistant particles **(d)**. 36

2.6 Computational domain and initial particle distribution for the cylindrical explosion problem. 38

2.7 Two dimensional numerical results of the blast wave problem with initial data given by Table 2.2 computed with V-B-SPH (Rusanov flux, $\sigma = 2$) at time $t = 0.2s$. Density and pressure **(a)**, **(b)**. Cut at $y = 0$ compared with 1D reference solution (continuous line) **(c)**, **(d)**. 42

2.8 Two dimensional numerical results of the blast wave problem EP1 with initial data given by Table 2.2 computed with MWSPH (Rusanov flux, $\sigma = 2$, $\sigma_{mls} = 4$, M=3) at time $t = 0.2s$. Density and pressure **(a)**, **(b)**. Cut at $y = 0$ compared with 1D reference solution (continuous line) **(c)**, **(d)**. . 44

2.9 Numerical results for EP1 obtained with the standard SPH at time $t = 0.2s$, $\sigma = 2$. 45

2.10 Two dimensional numerical results of the blast wave problem EP1 with initial data given by Table 2.2 computed with MWSPH (Osher flux, $\sigma = 2$, $\sigma_{mls} = 4$, M=3) at time $t = 0.2s$. Density and pressure **(a)**, **(b)**. Cut at $y = 0$ compared with 1D reference solution (continuous line) **(c)**, **(d)**. . . . 48

2.11 Comparison of the Lagrangian MWSPH simulation with *moving* particles (top) and an Eulerian MWSPH simulation with *fixed* particles (bottom). . 49

2.12 Two dimensional particle positions for the blast wave problem EP1 at the final time $t = 0.2s$. Standard SPH (2.12a) $\sigma = 2$, V-B-SPH (2.12b) $\sigma = 2$, MWSPH with Rusanov flux (2.12c) and MWSPH with Osher flux (2.12d) with polynomial degree $M = 3$, $\sigma = 2$ and $\sigma_{mls} = 4$). 50

2.13 Two dimensional numerical results of the blast wave problem EP2 with initial data given by Table 2.3 computed with V-B-SPH (Rusanov, $\sigma = 2$) and MWSPH (Osher flux, $\sigma = 2$, $\sigma_{mls} = 4$, M=3) at time $t = 0.2s$. Two dimensional pressure profile for V-B-SPH (Rusanov) and MWSPH (Osher) the top. Cut at $y = 0$ compared with 1D reference solution (continuous line) for pressure and density. 54

2.14 Unstructured triangular mesh used for the assessment of initial particle disorder in the case of blast wave problem EP2. 55
2.15 Numerical results for the blast wave problem EP2 with initial particles distributed on an unstructured triangular grid. Rusanov-type flux **(a)**, **(c)**. Osher-type flux **(b)**, **(d)**. 58
2.16 Numerical results for 1D Sod's problem compared with exact solution at the time t = 0.2s computed with 1D MWSPH: Rusanov flux on the top and Osher flux on the bottom. Polynomial degree $M = 2$, $\sigma = 2$. 60

3.1 Particle central stencils and recontructions polynomials. 68
3.2 Comparison of exact and numerical gradient reconstruction for the case of a smooth solution, obtained with standard SPH approach and with the MLS-WENO reconstruction. Equispaced particles and the cut of at y=0 evaluating the reconstructed polynomials on 100 equispaced points **(a)**, **(c)**. Not-equispaced particles and the cut of at y=0 evaluating the reconstructed polynomials on 100 equispaced points **(b)**, **(d)**. Polynomial reconstruction order $M = 3$, $\sigma = 1.5$, $\sigma_{mls} = 3$. 75
3.3 Piecewise smooth test case with discontinuity: gradient reconstruction, comparison of exact and numerical solutions obtained with standard SPH approach and with the MLS-WENO reconstruction. Equispaced particles and the cut of at y=0 evaluating the reconstructed polynomials on 100 equispaced points **(a)**, **(c)**. Non-equispaced particles and the cut of at y=0 evaluating the reconstructed polynomials on 100 equispaced points **(b)**, **(d)**. Polynomial reconstruction order $M = 3$, $\sigma = 1.5$, $\sigma_{mls} = 3$. 81
3.4 Comparison of exact and numerical solutions for equispaced particles at time $t = 1000$ obtained with standard SPH and different MWSPH with different reconstruction order. Three cuts along different sections (see Fig. 3.4a) are shown evaluating the numerical solution on 200×200 not-equispaced particles after 61 time step. $\sigma = 2.5$, $\sigma_{mls} = 4.5$, $CFL = 0.9$ and $\beta = 30°$. 85

3.5 Comparison of exact and numerical solutions for not-equispaced particles at time $t = 1000$ obtained with standard SPH and different MWSPH with different reconstruction order. Three cuts along different sections (see Fig. 3.4a) are shown evaluating the numerical solution on 200×200 not-equispaced particles after 61 time step. $\sigma = 2.5$, $\sigma_{mls} = 4.5$, $CFL = 0.9$ and $\beta = 30°$. 86
3.6 Difference between maximum concentration values of numerical (C_N) and analytical (C_A) solutions as function of time for equispaced particles (on the left) and not-equispaced particles (on the right), for different σ, comparing standard SPH and MWSPH with different reconstruction order M, $\sigma_{mls} = 4.5$ and $CFL = 0.9$. 87
3.7 Dilution index for equispaced particles and not-equispaced particles, $\alpha_T/\alpha_L = 0.1$ (on the left) and $\alpha_T/\alpha_L = 0.01$ (on the right), comparing standard SPH and MWSPH with different reconstruction order M, $\sigma_{mls} = 4.5$, $CFL = 0.9$ and $\sigma = 3$. 87
3.8 Dissipation rate rate for equispaced particles and not-equispaced particles, $\alpha_T/\alpha_L = 0.1$ (on the left) and $\alpha_T/\alpha_L = 0.01$ (on the right), comparing standard SPH and MWSPH with different reconstruction order M, $\sigma_{mls} = 4.5$, $CFL = 0.9$ and $\sigma = 3$. 88
3.9 Minimum concentration for different anisotropic ratio, $\alpha_T/\alpha_L = 0.1$ (on the left) and $\alpha_T/\alpha_L = 0.01$ (on the right), for different σ. Standard SPH and MWSPH with different reconstruction order M, $\sigma_{mls} = 4.5$ and $CFL = 0.9$. 88
3.10 Concentration distribution at time t=10 obtained with standard SPH scheme and different MWSPH orders, for different anisotropic ratio on 200×200 equispaced particles after 74 time step. $\sigma = 3.0$, $\sigma_{mls} = 4.5$, $CFL = 0.9$ and $\beta = 30°$. All cases exhibit negative concentrations (gray bands). . . . 89
3.11 Error norm L_1 computed for homogeneous test case with equispaced particles, $\sigma = 3$, $CFL = 0.9$. 91
3.12 Error norm L_1 computed for homogeneous test case with equispaced particles and computational time on a single processor Intel(R) Core(TM) i7-2640M CPU 2.80GHz. 91

3.13 Initial conditions on the left and velocity field on the right for heterogeneous test cases. 93
3.14 Concentration distribution at time $t = 1000$ obtained with standard SPH scheme and different MWSPH orders, for different anisotropic ratio with 200×200 particles after 32 time step for heterogeneous test cases. $\sigma = 3.0$, $\sigma_{mls} = 4.5$, $CFL = 0.9$. All cases exhibit negative concentrations (gray bands). 94
3.15 Negative concentration distribution for heterogeneous case at final simulation time. Comparison of the standard SPH with the MWSPH scheme for different reconstruction order of accuracy, $\sigma = 3.0$, $\sigma_{mls} = 4.5$, $CFL = 0.9$. 95
3.16 Negative concentration distribution for heterogeneous case. Comparison of the standard SPH with the MWSPH scheme with third reconstruction order of accuracy, $\sigma = 3.0$, $\sigma_{mls} = 4.5$, $CFL = 0.9$. 96
3.17 Maximum concentration in time for standard SPH and MWSPH scheme with third and fourth flux reconstruction order of accuracy, $\sigma = 3.0$, $\sigma_{mls} = 4.5$, $CFL = 0.9$. 96
3.18 Dilution index, heterogeneous case, $\sigma = 3$, $\sigma_{mls} = 4$, $CFL = 0.9$. 97

4.1 Standard SPH applied to chemotaxis, explicative test case. 107
4.2 Meshless MWSPH method extended to chemotaxis. Particle move along instantaneous streamlines carrying both bacteria and attractant concentrations. They exchange solute mass with particles that are within its kernel support both for dispersion and chemotaxis. One dimension cut through the reconstruction polynomials along the line connecting particles $\mathcal{P}_i$ and $\mathcal{P}_j$ as well states Q_{ij}^{-},$\nabla Q_{ij}^{-}$and Q_{ij}^{+},∇Q_{ij}^{+}extrapolated to the midpoint and chemotactic velocity computed form the extrapolated states. 111
4.3 Numerical solution for one dimensional test case at different time step, $CLF = 0.8$ $\sigma = 2$ and $M = 2$. 115
4.4 Diffusion test case, initial concentration for attractant and bacteria. 117
4.5 Numeral results for diffusion test case at time $T = 3.76$, $CFL = 0.9$, $\sigma = 3$, $\sigma_{mls} = 4$. Attractant concentration and chemotactic velocity field, bacteria concentration with or without the chemotactic. 118

4.6 Numeral results for diffusion test case, $CFL = 0.9$, $\sigma = 3$, $\sigma_{mls} = 4$. Bacteria concentration and snapshots at different time steps at section $sec - x$ for bacteria with or without chemotaxis. 119
4.7 Dual layers numerical set up, 250×150 particles $CFL = 0.9$, $\sigma = 3$ and $\sigma_{mls} = 4$. 122
4.8 Numerical results for advection-diffusion-chemotactic test case, $CFL = 9$, $\sigma = 3$, $\sigma_{mls} = 4$. 123
4.9 Dual layers numerical results for bacteria concentration at time $1225s$, 250×150 particles $CFL = 0.9$, $\sigma = 3$ and $\sigma_{mls} = 4$. 124
4.10 Dissipation rate and dilution index for bacteria with or without the contribution of chemotaxis. 125
4.11 Numerical results for advection-diffusion-chemotactic with intruction test case, $CFL = 0.9$, $\sigma = 3$, $\sigma_{mls} = 4$. 127

List of Tables

2.1 Numerical convergence results for smooth function reconstruction with second, third and fourth order version of the MLS-WENO scheme. In the first row the particles distance dx. The second, third and fourth columns contain the error measured in L_1, L_2 and L_∞ norms, followed by three columns giving the measured order of accuracy between the respective particles and the previous particles distributions. The last row gives the CPU time needed by the serial code on one Intel(R) Core(TM) i7-2640M CPU with 2.80GHz and 8 GB of RAM. 30
2.2 Initial states $\mathbf{Q}_{in}$ (inner) and $\mathbf{Q}_{out}$ (outer) for the first 2D explosion problem (EP1). 37
2.3 Initial states $\mathbf{Q}_{in}$ (inner) and $\mathbf{Q}_{out}$ (outer) for the second 2D explosion problem (EP2). 37

3.1 Numerical convergence results for Gaussian gradient reconstruction with second, third and fourth order version of the MLS-WENO scheme. In the first row the particles distance dx. The second, third and fourth columns contain the error measured in L_1, L_2 and L_∞ norms, followed by three columns giving the measured order of accuracy between the respective particles and the previous particles distributions. The last row gives the CPU time needed by the serial code on Intel(R) Core(TM) i7-2640M CPU 2.80GHz with 8 GB of RAM. The error norms refer to the concentration considering equispaced particles for the smooth case. 73

3.2 Numerical convergence results for Gaussian gradient reconstruction with second, third and fourth order version of the MLS-WENO scheme. In the first row the particles distance dx. The second, third and fourth columns contain the error measured in L_1, L_2 and L_∞ norms, followed by three columns giving the measured order of accuracy between the respective particles and the previous particles distributions. The last row gives the CPU time needed by the serial code on Intel(R) Core(TM) i7-2640M CPU 2.80GHz with 8 GB of RAM. The error norms refer to the concentration considering not equispaced particles for the smooth case. 76

3.3 Numerical convergence results for Gaussian gradient reconstruction with standard SPH. In the first row the particles distance dx. The second, third and fourth columns contain the error measured in L_1, L_2 and L_∞ norms, followed by three columns giving the measured order of accuracy between the respective particles and the previous particles distributions. The last row gives the CPU time needed by the serial code on Intel(R) Core(TM) i7-2640M CPU 2.80GHz with 8 GB of RAM. The error norms refer to the concentration considering not equispaced particles for the smooth case. . 77

3.4 Homogeneous test case parameters. 83

3.5 Numerical convergence result for anisotropic diffusion test case with standard SPH, third and fourth order fluxes reconstruction order.In the first row the particles distance dx. The second, third and fourth columns contain the error measured in L_1 , L_2 and L_∞, followed by three columns giving the measured order of accuracy between the respective particles and the previous particles distributions. The last row gives the CPU time needed by the serial code on Intel(R) Core(TM) i7-2640M CPU 2.80GHz with 8 GB of RAM. The error norms refer to the concentration considering equispaced particles for the homogeneous test case at time $t = 200$. 90

4.1 Parameters for the explicative standard SPH test case. 106

4.2 Parameters for one-dimensional test case. 114

4.3 Parameters for two dimensional diffusion test case. 116

4.4 The parameters for advection-diffusion-chemotaxis test case. 121

1 Introduction

Chemotaxis is the orientation or movement of cells, bacteria or multicellular organisms along a chemical concentration gradient (attractants) either toward or away from the chemical stimulus (chemorepellents) [*Eisenbach and Lengeler*, 2004]. In human biology chemoattaction have a fundamental role in vascular patterns development[*Serini et al.*, 2003], in tumor angiogenesis [*Roussos et al.*, 2011] or in atherogenesis [*Ibragimov et al.*, 2005] and even in neural network grouth and self-organization [*Segev and Ben-Jacob*, 2000]. Chemotaxis has been observed as in simple animal behavioral mechanism [*Ward*, 1973] [*Zuckerman and Jansson*, 1984] as in plants and big animals reproductive system [*Zimmera and Riffellc*, 2011]. A complete chemotaxis theory was reported for the first time at the end of the nineteenth century when *Pfeffer* [1887] and *Engelmann* [1881] analyzed chemotactic aggregation of bacteria in regions of high attractant concentration (see Fig. 1.1).

In the last century, bacterial chemotaxis has been an area of increasing interest to both experimentalists and theoreticians [*Tindall et al.*, 2008]; chemotactic behaviour was observed in many bacteria, such as Escherichia coli, Rhodobacter sphaeroides and Bacillus subtilus [*Tindall et al.*, 2008][1]; and in acqueos system bacteria chemotaxis is well documented and charaterized [*Mesibov R. and Adler*, 1973],[*Tindall et al.*, 2008].

In contrast, chemotaxis in porous media was distinguished and documented only recently [*Wang and Ford*, 2009]. For the first time, applying magnetic resonance imaging, *Olson* [2004] quantifies bacterial chemotactic parameters within a packed column suggesting that chemotaxis biodegradation in low permeability areas. *Long and Ford* [2009] reported enhancements in bacteria migration due to attractant gradient under groundwater

---

[1] For a comprehensive list of chemotactic bacterial species and the differences between them see [*Eisenbach and Lengeler*, 2004]

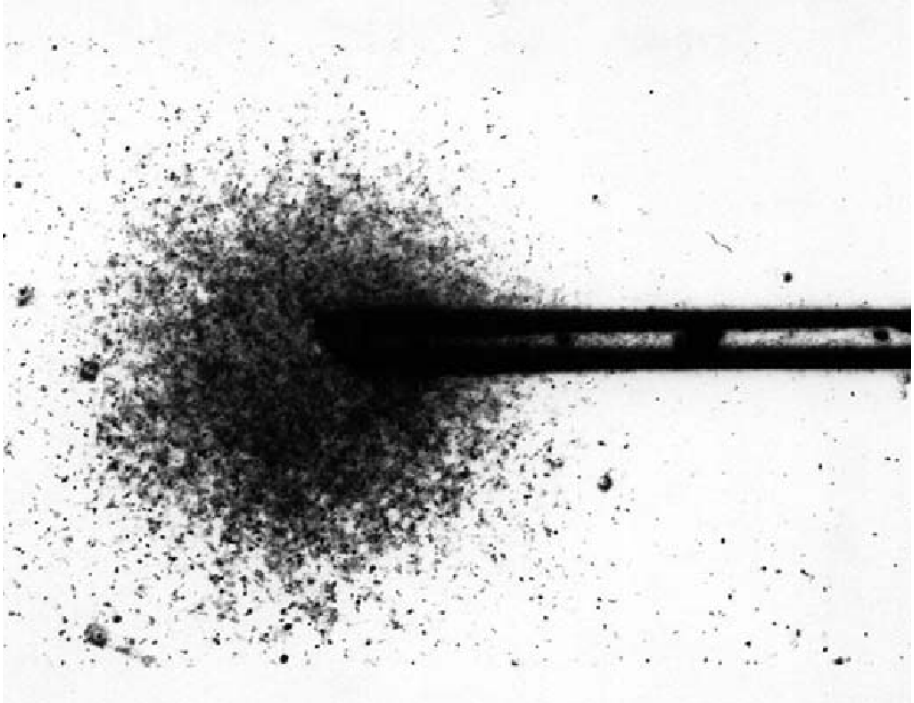

Figure 1.1: *Aggregation of chemotactic bacteria in regions of high attractant concentration as originally shown by Pfeffer [1887].*

flow condition both in homogeneous and heterogeneous laboratory test cases [*Wang and Ford*, 2009]. Pore scale simulations suggest that traveling bacteria bands may potentially reach velocity comparable to groundwater flow velocity [*Long and Hilpert*, 2008].

These experimental and theoretical researches clearly suggest chemotaxis as important process in microbial dynamics in porous media, and recently studies on role of chemotaxis in the transport and dynamics of bacteria at field scales are starting to take place (see for instance [*Long and Ford*, 2009],[*Valdés-Parada et al.*, 2009b],[*Wang et al.*, 2008]). However, the complexity of field scale, i.e. groundwater flow variability, heterogenety, biologial dynamics and spacial and temporal scale, has not yet allowed to define the magnitude and effect of chemotaxis.

The motile motion of a single bacteria relies on series of run and trumbles [*Tindalla et al.*, 2008] resulting in a random walk as the Brownian motion of particles in fluid [*Valdés-Parada et al.*, 2009b]. In presence of attractant this random walk is distorted so that the movement towards a better environment is favored [*Tindalla et al.*, 2008]. Starting from this single bacteria motion *Keller and Segel* [1971a] proposed a mathematical models for bacterial populations flux N_b in homogeneous fluid phase containing an attractanta as:

$$N_b = -\mathcal{D}_b \nabla c_b + \mathbf{v}_c c_b \tag{1.1}$$

The first term in expression (1.1) is the diffusive bacteria flux and represents the random component of bacteria motion. It is proportional to the bacteria concentration c_b where $\mathcal{D}_b$ is the the random mobility coefficient that quantifies the diffusive behavior of bacterial populations [*Ford and Harvey*, 2007b]. The second component is the adventive flux and it represents the bacterial population response to the attractant in term of chemotatic velocity [*Ford and Harvey*, 2007b] [*Valdés-Parada et al.*, 2009b]. The mathematical formulation of chemotaxis velocity was derived by *Chen et al.* [1998] starting from experimental observations on individual bacteria movement and then generalized by *Rivero et al.* [1989] as:

$$\mathbf{v}_c = \frac{2}{3} v_s tanh \left(\frac{\chi_0}{2v_s} \frac{k_d \|\nabla c_a\|}{(k_d + c_a)^2} \right) \frac{\nabla c_a}{\|\nabla c_a\|} \tag{1.2}$$

where k_d is the dissociation constant that represents the propensity of bacteria to sense gradient, v_s is the mean bacteria velocity speed, χ_0 is the sensitivity coefficients taking into account the bacteria response to attractants or repellents [*Ford and Harvey*, 2007b] [*Valdés-Parada et al.*, 2009b] and c_a is the attractant concentration. According to Eqn.(1.2) chemotatic bacteria concentration could have velocities comparable to groundwater flow velocity (Fig. 1). Although equations (1.1) and (1.2) are a complete model to describe

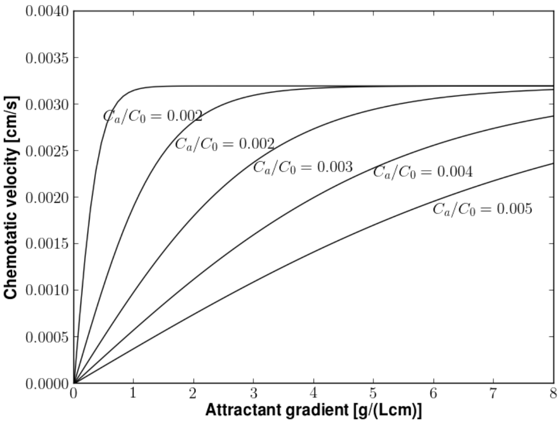

Figure 1.2: *Chemotatic velocity for different attractant concentrations and attractant gradients according to Rivero et al. [1989]'s formulation.*

bacteria chemotaxis, bacteria transport in porous media involves many other chemical, physical and biological processes which not only are closely linked but also strongly depend on porous media structure and on multiple time and space scales [*Murphy and Ginn*, 2000]. As a matter of fact the role and magnitude of chemotaxis can only be evaluated in this complex framework.

1.1 Mathematical model

The governing pore scale equation for the system under consideration are:

$$\mu\nabla^2\mathbf{v}_f(\mathbf{r}) = \nabla p(\mathbf{r}) - \rho_f\mathbf{g}, \tag{1.3a}$$

$$\nabla\cdot\mathbf{v}_f(\mathbf{r}) = 0, \tag{1.3b}$$

$$\frac{\partial c_{a,i}(\mathbf{r},t)}{\partial t} + \nabla\cdot\left(\mathbf{v}_f(\mathbf{r})c_{a,i}(\mathbf{r},t)\right) = \nabla\left(\mathcal{D}_{a,i}\nabla c_{a,i}(\mathbf{r},t)\right) + s_{a,i}, \tag{1.3c}$$

$$\frac{\partial c_{b,i}(\mathbf{r},t)}{\partial t} + \nabla\cdot\left(\left(\mathbf{v}_f(\mathbf{r}) + \mathbf{v}_{i,c}(\mathbf{r},t)\right)c_{b,i}(\mathbf{r},t)\right) = \nabla\left(\mathcal{D}_{b,i}\nabla c_{b,i}(\mathbf{r},t)\right) + s_{b,i}. \tag{1.3d}$$

Eqns. (1.3a) and (1.3b) are the momentum and continuity equation for fluid phase respectively, both in case of stationary flow [*Bear*, 1988], where the term $\mathbf{v}_f$ is the fluid velocity, μ is fluid viscosity, ρ_f the fluid density, p the fluid pressure and $\mathbf{g}$ is the gravity acceleration. Eqn. (1.3c) and (1.3d) represent the attractant solutes and bacteria species mass conservation equations respectively. The reader can note that bacteria transport is driven not only by convection and diffusion but also by chemotactic, where $\mathbf{v}_{c,i}$ is the is the bacteria chemotactic velocity for $i-th$ bacteria species [*Valdés-Parada et al.*, 2009b]. This mathematical model states that the attractant and bacteria concentration has no influence on fluid density and that solid are impermeable to bacteria. The term $\mathcal{D}_{a,i}$ is the attractant molecular diffusion and $\mathcal{D}_{b,eff,i}$ is the effective random mobility coefficient which is the analog of the diffusion coefficient of molecules *Valdés-Parada et al.* [2009b].

However, the solution of the pore scale model is not feasible to study and to understand chemotaxis at laboratory or more important at field scale [*Valdés-Parada et al.*, 2009b; *Porter et al.*, 2011]. As a matter of fact, by an up-scaling procedure, usually based on volume averaging [*Whitaker*, 1999], the pore scale continuum equations are referred to a Reference Elementary Volume (REV). The REV, often called Darcy's scale, has a length scale equal to many pore lengths [*Bear*, 1988; *Steefel et al.*, 2005], where we consider effective hydraulic properties and where the concentration are computed [*Herrera*, 2009].

The resulting macro scale model transport model is expressed as:

$$\mathbf{V}_f(\mathbf{r}) = -\frac{\mathbf{K}(\mathbf{r})}{\phi}\nabla h(\mathbf{r}), \tag{1.4a}$$

$$\nabla \cdot (\mathbf{K}(\mathbf{r})h(\mathbf{r})) = 0, \tag{1.4b}$$

where Eqns (1.4a) and (1.4b) are the flows equations in case of stationary flow with $\mathbf{V}_f$ the Darcy's velocity, $\mathbf{K}$ the hydraulic conductivity tensor, ϕ the porosity, and $h(\mathbf{r})$ the total hydraulic head [*Bear*, 1988].

The governing equation for the attractants is the well known advection diffusion reactions equation, that reads as:

$$\frac{\partial C_{a,i}}{\partial t} + \nabla \cdot \left(\mathbf{V}_f C_{a,i}\right) = \nabla \cdot \left(\mathbf{D}_{a,i}\left(\nabla C_{a,i}\right)\right) + R_{a,i} \tag{1.5}$$

Eqn. (1.5) is referred to the continuum scale where $C_{a,i}$ is the $i-th$ solute concentration which is regarded as homogeneous over the REV, where is the total reaction rate for $i-th$ component and $\mathbf{D}_{a,i}$ is the total hydrodynamic dispersion tensor. The term $\mathbf{D}_{a,i}$ is the sum of molecular diffusion and dispersion and it takes into account in the up-scaled model of pore scale flow fluctuations on diffusion [*Luo et al.*, 2008].

Similarly, the macroscale transport model for bacteria reads as follows[*Valdés-Parada et al.*, 2009b]:

$$\frac{\partial C_{b,i}}{\partial t} + \nabla \cdot \left(\left(\mathbf{V}_f + \mathbf{V}_c\right) C_{b,i}\right) = \nabla \cdot \left(\mathbf{D}_{b,i,eff}\left(\nabla C_{b,i}\right)\right) + R_{b,i} \tag{1.6}$$

where $C_{b,i}$ is the $i-th$ bacteria species concentration at Darcy's scale and $R_{b,i}$ is the total reaction rate for bacteria species $i-th$. The term $\mathbf{D}_{b,i,eff}$ is the total dispersion tensor for bacteria which is the sum of the effective bacteria mobility, the hydrodynamic dispersion and the contribution of chemotactic velocity to bacteria dispersion [*Porter et al.*, 2011; *Valdés-Parada et al.*, 2009b]. In Eqn. (1.6), $\mathbf{V}_c$ is the effective chemotactic velocity at Darcy' scale, which depends on bacteria transport properties as well on porous media structure [*Porter et al.*, 2011; *Valdés-Parada et al.*, 2009b]. In this contest, both $\mathbf{V}_c$ and $\mathbf{D}_{b,i,eff}$ are usually quantified by adopting an empirical approach [*Porter et al.*, 2011] based on fitting attractant and bacteria measured data scaling bacteria random mobility and chemotactic velocity with porous medium tortuosity or porosity [*Ford and Harvey*, 2007b; *Wang et al.*, 2008; *Long and Ford*, 2009; *Wang and Ford*, 2009]. *Valdés-Parada et al.* [2009b], by volume averaging, derives the effective chemotactic parameters under the assumptions on pore structure and attractant concentrations.

1.2 Numerical model

The chemotaxis add unique challenges to the particularities of flow and transport in porous media. As reported by *Sudicky* [1986], the hydraulic conductivity varies by several orders of magnitudes within short distances which implies a heterogeneous flow field both in magnitude and direction. As a result, the solute transport produces large variations of concentration within short distances. Due to the strongly and non-linearly dependence of chemotaxis velocity on attractant concentrations and attractant gradient, a correct representation of concentration and concentration gradient became fundamental and decisive in studying chemotaxis. Unfortunately, most of the standard numerical scheme add artificial numerical diffusion [*Herrera et al.*, 2009, 2010; *Boso et al.*, 2013]. This implies that the gradient are underestimate inhibiting the real bacteria chemotactic response. Similarly, particular attention should be paid to the low attractant concentration modeling where the chemotactic response is greater.

Recently *Herrera et al.* [2009, 2010] and *Boso et al.* [2013] show the advantages of the Smooth Particle hydrodynamics (SPH) [*Monaghan*, 2012] in modeling solute transport in porous media. The SPH is a fully meshfree scheme, it is free from grid orientation and with low numerical diffusion. Unlike standard particle based scheme, for example Random Walk Particle Tracking, particles carry solute concentration and not solute mass, implying twofold advantages: it can represent concentration values up to hardware precision and it is possible to compute reactions at individual particles without remapping.

The example (1.2) *Herrera et al.* [2009] gives an illustrative comparison of SPH against TVD solver and HMOC scheme in case of only advection. It is clear that, TVD and HMOC can not avoid numerical dispersion, smoothing sharp interfaces at the fringes of the plume and inhibiting artificially a possible chemotaxis response.

Unfortunately, there are some limitation in SPH extension to simulate chemotaxis: It can not handle multiple advection fields like in case of chemotaxis velocities and flow field velocity and it is very sensitive to particle disorder especially in gradient computation.

Moreover in case of anisotropic dispersion it produce negative concentrations.

These limitations of the standard SPH for the simulation of the advection diffusion plus chemotaxis transport in porous media provide the motivation for the research in this thesis.

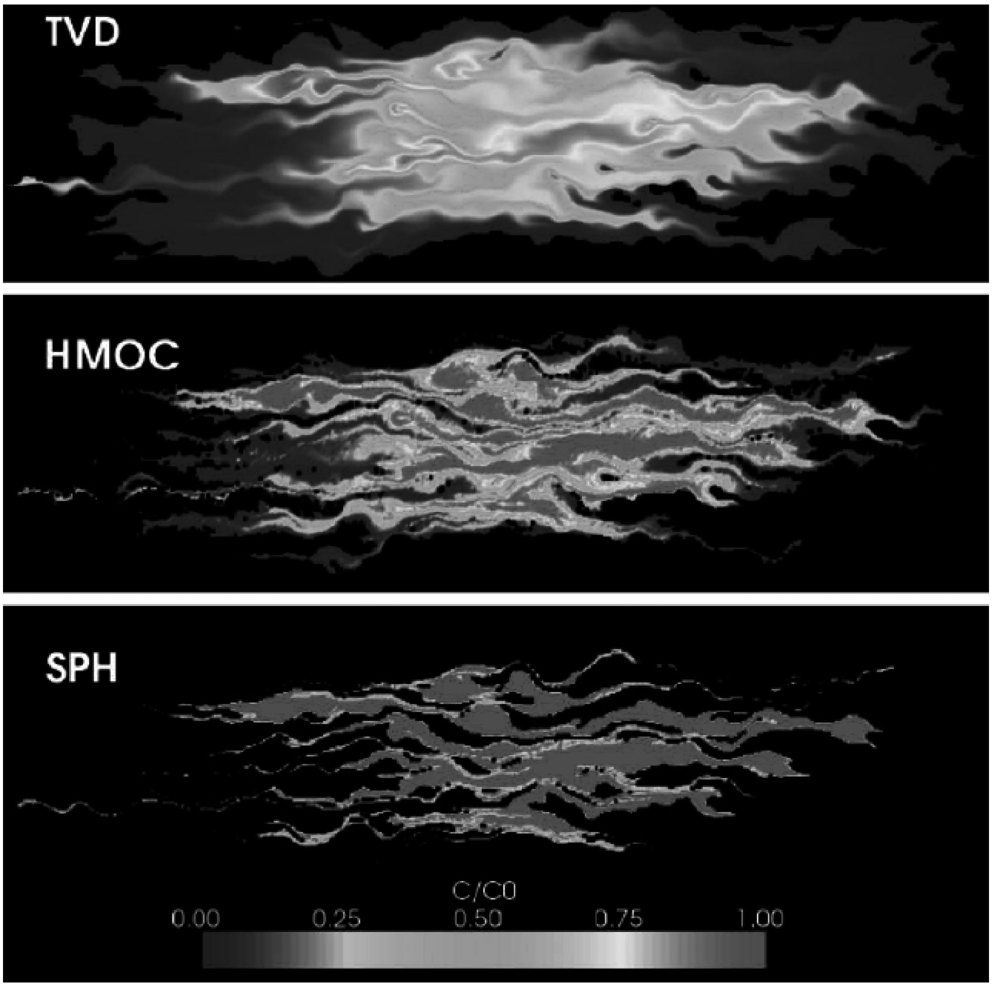

Figure 1.3: *Spatial concentration distribution at dimensionless for Pe = ∞. TVD solver (top), HMOC solver (middle), and SPH (bottom). Courtesy of Herrera et al. [2009]*

1.3 Objectives

The objective of this thesis is to develop, implement, and evaluate new numerical meshless methods scheme to correctly simulate the chemotaxis in porous media. We have the following specific objectives:

1. To derive and implement a new meshless scheme and test it with well known test cases;
2. To apply the new scheme in passive solute transport in porous media;
3. To compare the new scheme with traditional particle Lagrangian scheme;
4. To evaluate the suitability of using the new meshless in order to simulate chemotaxis in porous media;

1.4 Organization

Chapter 2 presents the derivation of a new numerical scheme focusing on the numerical solutions of Euler equations. The purpose of this Chapter is to introduce the new numerical Lagrangian scheme rather than to solve a specific problem and the solution of the inviscid flow problem is an appropriate test case providing both shock and rarefaction waves with reference and exact solutions. We develop a new class of meshless Lagrangian particle methods based on the SPH formulation of Vila & Ben Moussa [*Ben Moussa et al.*, 1999; *Ben Moussa*, 2006], combined with a new Weighted Essentially Non-Oscillatory (WENO) [*Dumbser et al.*, 2007, 2008a,b] reconstruction technique on moving point clouds in multiple space dimensions. The key idea is to produce for each particle first a set of high order accurate Moving Least Squares (MLS) [*Breitkopf et al.*, 2005] reconstructions on a set of different reconstruction stencils. Then, these reconstructions are combined with each other using a nonlinear WENO technique in order to capture at the same time discontinuities and to maintain accuracy and low numerical dissipation in smooth regions. The numerical fluxes between interacting particles are subsequently evaluated using this MLS-WENO reconstruction at the midpoint between two particles, in combination with a Riemann solver [*Toro*, 1997] that provides the necessary stabilization of the scheme based on the underlying physics of the governing equations. We propose the use of two different

Riemann solvers: the Rusanov flux and an Osher-type flux [*Dumbser and Toro*, 2011a]. The use of monotone fluxes together with a WENO reconstruction ensures accuracy, stability, robustness and an essentially non oscillatory solution without the artificial viscosity term usually employed in conventional SPH schemes. To our knowledge, this is the first time that the WENO method, which has originally been developed for mesh-based schemes in the Eulerian framework on fixed grids, is extended to meshfree Lagrangian particle methods like SPH in multiple space dimensions. We test the new algorithm on two dimensional blast wave problems and on the classical one-dimensional Sod shock tube problem [*Sod*, 1978] for the Euler equations of compressible gas dynamics [*Toro*, 1997]. We obtain a good agreement with the exact or numerical reference solution in all cases and an improved accuracy and robustness compared to existing standard SPH schemes.

We extend the MWSPH to approximate advection diffusion equations with anisotropic diffusion tensor. We demonstrate that the MWSPH, is stable and accurate and that it reduces the occurrence of negative concentrations. We compare then the new MWSPH with standard SPH scheme in modeling advection-diffusion equations in case of anisotropic dispersion. The comparison is performed by considering analytical solutions and some indicators such as minimum concentration, maximum concentration, dilution index and dissipation rate.

Chapter 4 analyzes the limits of standard SPH in modeling chemotaxis. Then we presents the numerical strategy to model the chemotaxis with the MWSPH. A key element of the proposed approach is that the advection chemotactic flux is appropriated in a relative moving frame with fluid motion using Riemann solvers in complete meshfree framework. The MWSPH solutions of bacteria chemotaxis are compared with reference solutions, obtaining a satisfactory agreement. We perform some numerical experiments in order to analyze the effect of chemotaxis on bacteria transport

Finally, a summary of the results and main findings are given in Chapter 5. In this work, the each Chapter is stand-alone piece of work including individual introduction, methodology and results. Thus, for sake of clarity, equations and notations are independently redefined.

2 A New Class of Moving-Least-Squares WENO-SPH Schemes

[1]

Smooth Particle Hydrodynamics (SPH) is a *truly* [*Liu and Liu*, 2010] meshfree Lagrangian scheme developed by *Lucy* [1977]; *Gingold and Monaghan* [1977] for astrophysical applications and successively extended to solid mechanics [*Libersky and Petschek*, 1991; *Libersky et al.*, 1993; *Johnson and Beissel*, 1996], free surface flow [*Monaghan*, 1994, 2005; *Ferrari et al.*, 2009], multiphase transport [*Hu and Adams*, 2006; *Deng et al.*, 2013; *Adami et al.*, 2010b] and diffusive transport problems [*Cleary and Monaghan*, 1999; *Español and Revenga*, 2003; *Herrera et al.*, 2009, 2010; *Boso et al.*, 2013]. Comprehensive reviews of different SPH schemes that have been developed so far can be found in *Vignjevic and Campbell* [2009]; *Liu and Liu* [2010] and *Monaghan* [2012].

In SPH the continuum is discretized by a finite set of interpolation points, which are particles that carry physical properties such as mass, density, pressure and velocity [*Fang et al.*, 2009; *Monaghan*, 1994]. Since SPH is a Lagrangian particle method, the particles move with the local fluid velocity. This makes SPH suitable for advection- dominated dynamics [*Fang et al.*, 2009; *Liu et al.*, 2003b,a] and complex flow problems [*Adami et al.*, 2010a; *Colagrossi and Landrini*, 2003; *Ferrari et al.*, 2009]. Moreover, the meshfree particle nature of SPH has opened also applications to molecular dynamics at nano and microscale [*Ellero*, 2009; *Gholami et al.*, 2013] and microrheology [*Vauez-Quesada et al.*, 2012].

In its original formulation SPH suffers from the lack of consistency [*Belytschko et al.*, 1998], low order of accuracy and the so-called tensile instability [*Swegle et al.*, 1995].

---

[1] A version of this chapter has been accepted for publication in Journal of Computational Physics

Consequently, many modifications and improvements have been proposed over the years. A set of papers (see for example [*Liu et al.*, 1995; *Dilts*, 1999; *Zhang and Batra*, 2004; *Monaghan*, 2005; *Liu and Liu*, 2006]) have addressed the consistency problem by improving the interpolation kernel function and its derivative. However, satisfying the consistency condition for the kernel at the continuous level does not necessary lead to consistency in the SPH scheme at the discrete level *Liu and Liu* [2010]. On the other hand, solving the compressible Euler equations with the original SPH scheme may lead to unphysical oscillations, such as the so-called tensile instability [*Monaghan*, 2000]. *Monaghan* [2000] introduced artificial viscosity and velocity smoothing terms to handle both tensile instability and discontinuities in the solution. However, even with these modifications a spike may appear in the pressure field at the location of the contact discontinuity and additional numerical diffusion is added also in regions away from shocks. To attenuate these problems, *Balsara* [1995] introduced an upper bound for the artificial viscosity, while *Gingold and Monaghan* [1977] used a variable viscosity coefficient to reduce numerical diffusion in smooth regions.

Regarding incompressible fluid dynamics different modifications have been proposed to reduce tensile instability and unphysical oscillations. The ISPH (Incompressible-SPH) formulation solves the Poisson equation for the pressure and enforces the divergence condition for the velocity field, see e.g. [*Hu and Adams*, 2009; *Xu et al.*, 2009]. *Ellero et al.* [2007] instead achieve incompressibility by imposing that particle volumes do not change. In the WCSPH (Weakly Compressible Smooth Particle Hydrodynamics) the fluid is considered weakly compressible and a constant background pressure field ensures non-negative pressures and reduces tensile instability, see e.g. [*Colagrossi and Landrini*, 2003; *Adami et al.*, 2010a]. However the background pressure can introduce additional numerical viscosity. Recently *Adami et al.* [2013] proposed an alternative WCSPH based on a different formulation of particle momentum velocity and the particle advection velocity.

Vila [1999] and *Ben Moussa* [2006] introduced a different SPH formulation that is very close to the finite volume formalism and is based on Riemann solvers. It does not require any artificial viscosity terms for stabilization. In this formulation the artificial viscosity is replaced by the intrinsic numerical viscosity of the Riemann solver. This completely avoids the use of the artificial viscosity term and its cumbersome calibration. In addition Vila and Ben Moussa showed that their scheme is L_∞ stable under CFL condition for monotone fluxes. For example, *Ferrari et al.* [2009] obtained monotone pressure fields for free surface flows by using a monotone Rusanov flux in contrast to standard SPH. Unfortunately, despite its advantages, this alternative formulation is excessively diffusive even when applying Gudonov's flux based on the exact Riemann solver [*Ferrari et al.*, 2009]. Similarly, *Inutsuka* [2002] reformulates the SPH with Riemann solvers in the so called Godunov-SPH schemes (GSPH) where the Riemann solvers are based on kernel interpolation and Taylor series kernel interpolation of primitive variables in the region of interacting particles. Recently, in a review on SPH schemes applied to the compressible Euler equations [*Puri and Ramachandran*, 2014] the authors show that also GSPH may produce unphysical oscillations and does not eliminate the spike of the pressure field at the contact wave in the one-dimensional case. One also should mention the recently developed rpSPH method *Abel* [2011], which improves the behavior of the pressure field in the presence of shear waves.

The motivation of this chapter is therefore to develop and to apply a new SPH scheme that is not affected by the tensile instability or other known SPH instabilities and which does not produce excessive numerical dissipation. Our method is based on the approach of Vila & Ben Moussa and achieves at the same time higher accuracy and more robustness than standard SPH schemes. The key difference with respect to the existing SPH schemes is the introduction of a new high order accurate nonlinear meshfree MLS-WENO reconstruction operator into SPH and to use this higher order non-oscillatory data in combination with a Riemann solver to compute the particle interactions.

Preliminary investigations about the use of high order reconstructions within the SPH framework have been carried out in one space dimension in [*Renaut et al.*, 2013; *Xueying et al.*, 2013]. However, to the best knowledge of the authors, such techniques have never been used in multiple space dimensions, which is the declared scope of the present chapter. A further limitation of the method presented in [*Xueying et al.*, 2013] is that the particle volumes do not evolve in time and that the particles do not move, i.e. the scheme essentially reduces to a one-dimensional Eulerian approach on fixed grids. In contrast, the new method presented in this article is a meshless Lagrangian particle method based on MLS-WENO reconstruction on moving point clouds in multiple space dimensions. For the use of higher order ENO and WENO reconstructions in mesh-based cell-centered Lagrangian finite volume schemes see *Cheng and Shu* [2007]; *Liu et al.* [2009]; *Boscheri and Dumbser* [2013b]; *Dumbser and Boscheri* [2013]; *Boscheri et al.* [2014].

The rest of the Chapter is organized as follows. In Section 3.1 we introduce the Euler equations of compressible gas dynamics in conservative and non-conservative form. In Section 2.2.1 we briefly describe the standard SPH scheme and in Section 2.2.2 we present the SPH approach based on Riemann solvers proposed by Vila & Ben Moussa. The Riemann solvers used in this chapter are explained in Section 2.2.3, while in Section 2.3 we introduce our new meshfree MLS-WENO reconstruction giving all details of the reconstruction procedure. In Section 2.4.1, the MLS-WENO SPH scheme (in the following denoted by MWSPH) is compared with the standard SPH method and, in particular, its robustness with respect to particle disorder is assessed. In Section 2.4.2 the new MWSPH scheme is applied to inviscid compressible gas dynamics and comparisons with standard SPH and the SPH of Vila & Ben Moussa are made. Finally, Section 2.5 gives some concluding remarks and an outlook to future research.

2.1 Governing equations

In a Lagrangian frame the two-dimensional Euler equations for an ideal compressible fluid assume the following non-conservative form:

$$\frac{d\rho}{dt} = -\rho\nabla\cdot\mathbf{v}, \tag{2.1a}$$

$$\frac{d\mathbf{v}}{dt} = -\frac{\nabla p}{\rho}, \tag{2.1b}$$

$$\frac{de}{dt} = -\frac{p}{\rho}\nabla\cdot\mathbf{v}, \tag{2.1c}$$

where (2.1a) is the continuity equation, (2.1b) is the momentum balance equation and (2.1c) is the energy conservation equation. Here $\frac{d}{dt}$ denotes the total derivative, ρ is the density of the fluid, $\mathbf{v} = (u, v)$ the velocity vector, p the pressure and e is the specific internal energy per unit mass. For ideal gases the following constitutive equation is typically adopted:

$$e = \frac{p}{(\gamma-1)\rho}, \tag{2.2}$$

in which γ is a constant representing the ratio of specific heat capacities of the fluid [*Toro*, 1997]. System (2.1) in completed by the equation of motion which reads

$$\frac{d\mathbf{r}}{dt} = \mathbf{v}, \tag{2.3}$$

where $\mathbf{r} = (x, y)$ is the position of a given infinitesimal control volume. According to Vila's formalism it is useful to rewrite the system (2.1) in the following compact conservative form

$$\frac{\partial \mathbf{Q}}{\partial t} + \nabla \cdot \mathbf{F}(\mathbf{Q}) = 0, \tag{2.4}$$

where $\mathbf{Q}$ is the vector of conservative variables and $\mathbf{F} = (\mathbf{f}, \mathbf{g})$ is the flux tensor. For the compressible Euler equations they read

$$\mathbf{Q} = \begin{pmatrix} \rho \\ \rho u \\ \rho v \\ E \end{pmatrix}, \qquad \mathbf{f} = \begin{pmatrix} \rho u \\ \rho u^2 + p \\ \rho u v \\ u(E+p) \end{pmatrix}, \qquad \mathbf{g} = \begin{pmatrix} \rho v \\ \rho u v \\ \rho v^2 + p \\ v(E+p) \end{pmatrix}. \tag{2.5}$$

Here, E is the total energy density defined as

$$E = \rho e + \frac{1}{2}\rho\left(u^2 + v^2\right), \tag{2.6}$$

hence the pressure can be written as follows:

$$p = (\gamma - 1)\left(E - \frac{1}{2}\rho\left(u^2 + v^2\right)\right). \tag{2.7}$$

2.2 SPH formulations

2.2.1 The standard SPH formulation

Following the SPH formalism the computational domain Ω is discretized by a finite set of N particles $\mathcal{P}_i$ $(i \leq 1 \leq N)$, with positions $\mathbf{r}_i$ and mass m_i. The original SPH form presented by *Gingold and Monaghan* [1977] discretizes the Euler equations (2.1a)-(2.1c) and (2.3) as follows:

$$\rho_i = \sum_{j=1}^{N} m_j W_{ij}, \tag{2.8a}$$

$$\frac{d\mathbf{v}_i}{dt} = -\sum_{j=1}^{N} m_j \left(\frac{p_i}{\rho_i^2} + \frac{p_j}{\rho_j^2} + \Pi_{ij} \right) \cdot \nabla W_{ij}, \tag{2.8b}$$

$$\frac{de_i}{dt} = -\sum_{j=1}^{N} m_j \left(\frac{p_i}{\rho_i^2} + \frac{p_j}{\rho_j^2} + \Pi_{ij} \right) \left(\mathbf{v}_j - \mathbf{v}_i \right) \cdot \nabla W_{ij}, \tag{2.8c}$$

$$\frac{d\mathbf{r}_i}{dt} = \mathbf{v}_i, \tag{2.8d}$$

where the subscript i denotes the number of particle $\mathcal{P}_i$. The term $W_{ij} = W(\mathbf{r}_i, \mathbf{r}_j)$ is the interpolation kernel centered in $\mathbf{r}_i$ and ∇W_{ij} is its gradient with respect to $\mathbf{r}_i$. Among the available kernel functions we choose the cubic spline kernel [*Monaghan*, 2005]:

$$W_{ij} = \frac{\kappa}{h_{ij}^{\nu}} \begin{cases} 1/3 - q_{ij}^2 + q_{ij}^3/2, & \text{if } 0 \leq q_{ij} < 1, \\ (2 - q_{ij})^2 + q_{ij}^3, & \text{if } 1 \leq q_{ij} \leq 2, \\ 0, & \text{if } q_{ij} > 0, \end{cases} \tag{2.9}$$

because it is less demanding in terms of computational time than other possible choices such as the standard Gaussian kernel [*Ferrari et al.*, 2009]. In Eqn. (4.13), q_{ij} is defined as $q_{ij} = \left\| \mathbf{r}_j - \mathbf{r}_i \right\| / h_{ij}$, κ is a normalization constant so that $\int_{\mathbb{R}^{\nu}} W dV = 1$ and ν is the number of space dimensions, i.e. $\nu = 2$ in our applications. The term h_{ij} is the smoothing length [*Monaghan*, 1994, 2005] and it can be locally variable according to the following expressions:

$$h_{ij} = \frac{1}{2} \left(h_i + h_j \right), \qquad \text{with} \qquad h_i = \sigma \sqrt[\nu]{\frac{m_j}{\rho_j}}, \tag{2.10}$$

where σ is a suitable constant chosen in such a way that enough particles are in within the compact support of each kernel. We usually choose $\sigma \in [1.5; 2.0]$, which leads to approximately 40-50 interpolation particles in the compact support of each kernel. The term Π_{ij} is an artificial viscosity added to the momentum equation and to the energy equation in order to reduce unphysical oscillations at discontinuities. It is given by:

$$\Pi_{ij} = \begin{cases} \mu_{ij} \frac{\beta \mu_{ij} - \alpha \bar{\rho}_{ij}}{\bar{\rho}_{ij}}, & \text{if } \mathbf{v}_{ij} \cdot \mathbf{n}_{ij} \leq 0, \\ 0, & \text{if } \mathbf{v}_{ij} \cdot \mathbf{n}_{ij} > 0, \end{cases} \tag{2.11}$$

$$\mu_{ij} = h_{ij} \frac{\mathbf{v}_{ij} \cdot \mathbf{n}_{ij}}{\left\| \mathbf{r}_j - \mathbf{r}_i \right\|}, \qquad \text{with} \qquad \mathbf{v}_{ij} = \mathbf{v}_j - \mathbf{v}_i. \tag{2.12}$$

We emphasize that, according to Eqn. (2.12), the artificial viscosity vanishes as the distance between the particles increases and it depends on the parameters α and β which require a specific numerical calibration for each case.

2.2.2 The SPH formulation of Vila and Ben Moussa

The semi-discrete form of the Vila & Ben Moussa approach discretizes the Euler equations (Eqn. 2.4) as

$$\frac{dV_i \mathbf{Q}_i}{dt} = -\sum_j^N V_i V_j 2 \mathbf{G}_{ij} \cdot \nabla W_{ij}, \tag{2.13}$$

$$\frac{dV_i}{dt} = \sum_j^N V_i V_j 2 (\bar{\mathbf{v}}_{ij} - \mathbf{v}_i) \nabla W_{ij}, \tag{2.14}$$

$$\frac{d\mathbf{r}_i}{dt} = \mathbf{v}_i, \tag{2.15}$$

where V_i is the volume of each particle that evolves according to Eqn (2.14), $\mathbf{G}_{ij}$ is the numerical flux tensor and $\bar{\mathbf{v}}_{ij} = \frac{1}{2}(\mathbf{v}_i + \mathbf{v}_j)$ is the velocity at the interface between the two interacting particles $\mathcal{P}_i$ and $\mathcal{P}_j$. Similar to the finite volume formalism, Eqn (2.13) describes the interaction between pairs of control volumes V_i and V_j along the direction $\mathbf{n}_{ij}$ with a discontinuity at the midpoint. The flux $\mathbf{G}_{ij}$ is given by an exact or approximate Riemann solver in the co-moving frame. For example in *Vila* [1999] Vila proposes to use a first order Godunov method that assumes piecewise constant initial data for the Riemann problem and that reads as:

$$\mathbf{G}_{ij} = \mathbf{G}_{ij}(\mathbf{Q}_i, \mathbf{Q}_j) = \mathbf{F}_{ij}(\mathbf{Q}_E) - \mathbf{Q}_E \otimes \bar{\mathbf{v}}_{ij}, \tag{2.16}$$

where $\mathbf{F}_{ij}(\mathbf{Q}_E)$ is the flux tensor evaluated at the state $\mathbf{Q}_E = \mathbf{Q}_E(\mathbf{Q}_i, \mathbf{Q}_j)$, which is the exact solution of the associated one-dimensional Riemann problem between two interacting particles $\mathcal{P}_i$ and $\mathcal{P}_j$, i.e. the so-called Godunov state. In this approach also the interface velocity $\bar{\mathbf{v}}_{ij}$ could be computed by the exact solution of the one-dimensional Riemann problem. In the same work *Vila* [1999] also introduces a second order MUSCL-type scheme in the SPH framework, based on linear kernel interpolation of the derivative and the use of TVD slope limiters.

The new SPH formulation proposed in this chapter evaluates the numerical fluxes at the midpoint between two interacting particles $\mathcal{P}_i$ and $\mathcal{P}_j$ using high order WENO reconstruction polynomials as $\mathbf{G}_{ij} = \mathbf{G}_{ij}(\mathbf{Q}_{ij}^-, \mathbf{Q}_{ij}^+)$. The general idea is to perform a piecewise high order accurate essentially non-oscillatory reconstruction around each particle's position $\mathbf{r}_i$ knowing the point values $\mathbf{Q}_j$ of particles in its surrounding. As summarized in Fig. 3.1.2 we first define local high order reconstruction polynomials $\mathbf{Q}_i(\mathbf{r})$ and $\mathbf{Q}_j(\mathbf{r})$ for each couple of interacting particles $\mathcal{P}_i$ and $\mathcal{P}_j$ and then we evaluate these reconstruction polynomials at the midpoint $\bar{\mathbf{r}}_{ij} = \frac{1}{2}(\mathbf{r}_i + \mathbf{r}_j)$. The left state $\mathbf{Q}_{ij}^- = \mathbf{Q}_i(\bar{\mathbf{r}}_{ij})$ is obtained by extrapolating the reconstruction around particle $\mathcal{P}_i$ to the midpoint and the right state $\mathbf{Q}_{ij}^+ = \mathbf{Q}_j(\bar{\mathbf{r}}_{ij})$ by extrapolating the reconstruction around particle $\mathcal{P}_j$ to the midpoint. The approach combines the Moving Least Squares (MLS) method of reconstructing continuous functions from known points values with a nonlinear WENO technique in order to avoid spurious oscillations in the presence of strong gradients or discontinuities.

In its essence our scheme is the combination of MLS with WENO within the more general SPH formulation of Vila & Ben Moussa. In the following we denote the resulting scheme by MWSPH. We emphasize that the MWSPH does not use kernel interpolation or the kernel convolution integral to introduce Riemann solvers in SPH as in GSPH schemes. For the sake of clarity, we call hereafter the original Vila & Ben Moussa SPH formulation V-B-SPH.

2.2.3 Numerical Fluxes

In this work we use two Riemann solvers to define the numerical flux $\mathbf{G}_{ij}$: the simple Rusanov flux [*Toro*, 1997] and the Osher-type solver proposed in *Dumbser and Toro* [2011b,a]. Both solvers can be applied to the V-B-SPH and to the new MWSPH presented here. The only difference lies in the fact that the former method uses the particle states $\mathbf{Q}_i$ and $\mathbf{Q}_j$, while the latter uses the reconstructed states $\mathbf{Q}_{ij}^-$ and $\mathbf{Q}_{ij}^+$ extrapolated to the particle interface located at the midpoint $\bar{\mathbf{r}}_{ij}$.

The Rusanov flux assumes the following expression:

$$\mathbf{G}_{ij} = \frac{1}{2}\left(\mathbf{H}\left(\mathbf{Q}_{ij}^+, \bar{\mathbf{v}}_{ij}\right) + \mathbf{H}\left(\mathbf{Q}_{ij}^-, \bar{\mathbf{v}}_{ij}\right)\right) - \frac{c_{ij}}{2}\left(\mathbf{Q}_{ij}^+ - \mathbf{Q}_{ij}^-\right) \otimes \mathbf{n}_{ij}, \qquad \bar{\mathbf{v}}_{ij} = \frac{1}{2}(\mathbf{v}_{ij}^- + \mathbf{v}_{ij}^+), \tag{2.17}$$

where $\mathbf{H}$ is the flux tensor of the Euler equations in a reference frame moving with velocity $\mathbf{v}$:

$$\mathbf{H}(\mathbf{Q}, \mathbf{v}) = \mathbf{F}(\mathbf{Q}) - \mathbf{Q} \otimes \mathbf{v}. \tag{2.18}$$

We remark that the translation velocity itself is computed from the reconstructed variables, see Eqn (3.10). The term c_{ij} is instead the maximum absolute value of the eigenvalues of the Jacobian matrix $\mathbf{A_n} = \mathbf{A_n}(\mathbf{Q}, \mathbf{v}) = \partial \mathbf{H}/\partial \mathbf{Q} \cdot \mathbf{n}_{ij}$, evaluated along the direction $\mathbf{n}_{ij}$ in a moving frame, which reads as:

$$c_{ij} = \max(|\Lambda(\mathbf{Q}_{ij}^-)|, |\Lambda(\mathbf{Q}_{ij}^+)|), \tag{2.19}$$

with Λ being the diagonal matrix of the eigenvalues of $\mathbf{A_n}(\mathbf{Q}, \mathbf{v})$.

The second flux is an Osher-type flux [*Dumbser and Toro*, 2011b,a] and reads

$$\mathbf{G}_{ij} = \frac{1}{2}\left(\mathbf{H}\left(\mathbf{Q}_j^+ \bar{\mathbf{v}}_{ij}\right) + \mathbf{H}\left(\mathbf{Q}_i^-, \bar{\mathbf{v}}_{ij}\right)\right) - \Theta\left(\mathbf{Q}_j^+ - \mathbf{Q}_i^-\right) \otimes \mathbf{n}_{ij}, \qquad \bar{\mathbf{v}}_{ij} = \frac{1}{2}(\mathbf{v}_{ij}^- + \mathbf{v}_{ij}^+), \tag{2.20}$$

where Θ is the dissipation matrix in the reference frame moving with velocity $\bar{\mathbf{v}}_{ij}$. Following [*Dumbser and Toro*, 2011b,a; *Boscheri and Dumbser*, 2013a] Θ is written as

$$\Theta = \frac{1}{2} \int_0^1 \left|\mathbf{A_n}(\Psi(s), \bar{\mathbf{v}}_{ij})\right| ds, \tag{2.21}$$

with $\mathbf{A_n}$ evaluated along $\mathbf{n}_{ij}$ and Ψ being the straight-line segment path connecting the left and right state in phase-space:

$$\Psi(s) = \Psi(s, \mathbf{Q}_{ij}^+, \mathbf{Q}_{ij}^-) = \mathbf{Q}_{ij}^- + s(\mathbf{Q}_{ij}^+ - \mathbf{Q}_{ij}^-). \tag{2.22}$$

The integral Θ is approximated using a three point Gauss-Legendre quadrature with points

s_k and associated weights ω_k^g, namely:

$$\Theta \approx \frac{1}{2}\sum_{k=1}^{G} \omega_k^g \left|(\mathbf{A_n}(\Psi(s_k), \bar{\mathbf{v}}_{ij})\right|, \tag{2.23}$$

where the absolute value of the matrix $\mathbf{A_n}$ is defined as usual as

$$|\mathbf{A_n}| = \mathbf{R}|\Lambda|\mathbf{R}^{-1}, \tag{2.24}$$

where $\mathbf{R}$ is the matrix of right-eigenvectors of $\mathbf{A_n}$ and $\mathbf{R}^{-1}$ is its inverse.

In a second step we introduce two fundamental changes into the original V-B-SPH formulation. We add an additional term in Eqn. (2.13), which at the continuous level has a null contribution:

$$\frac{dV_i\mathbf{Q}_i}{dt} = -\sum_{j}^{N} V_i V_j 2\left(\mathbf{G}_{ij} - \mathbf{H}_i\right) \cdot \nabla W_{ij} \tag{2.25}$$

This additional term, $\mathbf{H}_i(\mathbf{Q}_i, \mathbf{v}_i) = \mathbf{F}(\mathbf{Q}_i) - \mathbf{Q}_i \otimes \mathbf{v}_i$ is the Lagrangian flux tensor computed at the state of the i-th particle and leads to a *flux-difference* formulation of the SPH scheme, which is similar to the idea of flux-difference formulations used in the finite volume context. According to general SPH derivative rules this term has a null contribution at the continuous level ($\int \mathbf{H}_i \nabla W dV = \mathbf{H}_i \int \nabla W dV = 0$), but it has in general a non-zero contribution at the discrete level ($\sum_j \mathbf{H}_i \nabla W_{ij} \neq 0$). However, at the discrete level it ensures at least zeroth order consistency, i.e. it allows the scheme to maintain a constant solution exactly.

Furthermore, instead of using Eqn. (2.15) we decide to move the particles according to the rule

$$\frac{d\mathbf{r}_i}{dt} = \frac{\sum_{j}^{N} \bar{\mathbf{v}}_{ij} V_j W_{ij}}{\sum_{j}^{N} V_j W_{ij}}. \tag{2.26}$$

Eqn. (2.26) uses a *smoothed* velocity field for the particle motion, which is based on the interface velocities $\bar{\mathbf{v}}_{ij}$. In this manner the final particle velocity is chosen consistently with the interface velocities $\bar{\mathbf{v}}_{ij}$ used in the ALE fluxes (2.18).

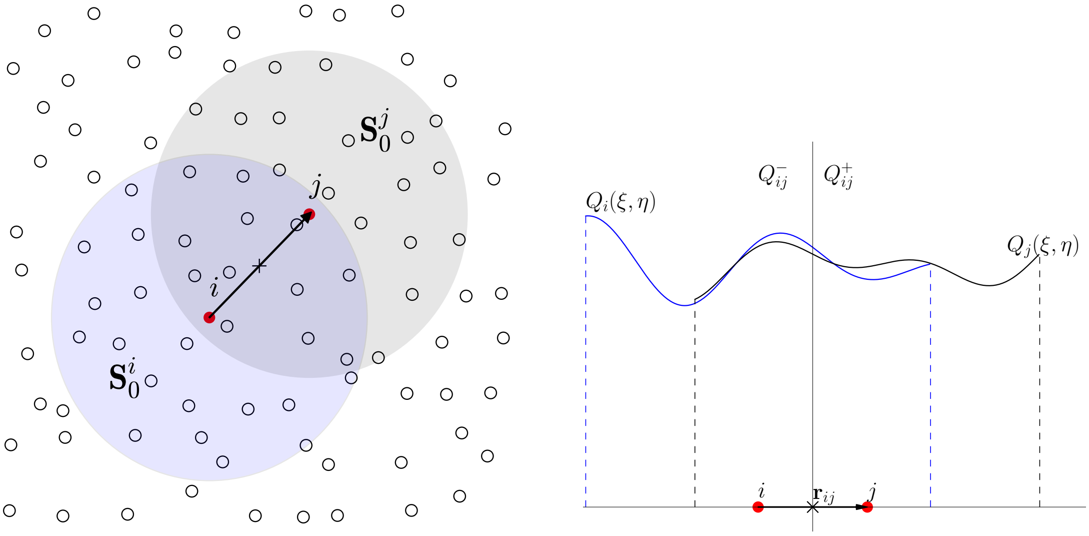

(a) **(b)**

Figure 2.1: *Examples of central reconstruction stencils* S_0^i *and* S_0^j *for a generic pair of interacting particles* $\mathcal{P}_i$ *and* $\mathcal{P}_j$ *(left). One-dimensional cut through the reconstruction polynomials* $Q_i(\mathbf{r})$ *and* $Q_j(\mathbf{r})$ *along the line connecting* $\mathcal{P}_i$ *and* $\mathcal{P}_j$*, as well as the states* Q_{ij}^- *and* Q_{ij}^+ *extrapolated to the midpoint* $\bar{\mathbf{r}}_{ij}$ *between the interacting particles (right).*

2.3 Moving-Least-Squares WENO reconstruction

The main ingredient of the nonlinear spatial reconstruction operator is the polynomial WENO method developed by *Friedrich* [1998], *Käser and Iske* [2005] and *Dumbser et al.* [2007] as an alternative to the classical point-wise WENO reconstruction [*Jiang and Shu*, 1996; *Hu and Shu*, 1999]. Following the general guidelines given in [*Dumbser and Kaëser*, 2007; *Dumbser et al.*, 2007] we first construct a set of reconstruction stencils for each particle as follows:

$$\mathcal{S}_s^i = \bigcup_k^{ne_s} \mathcal{P}_{j(k)}, \tag{2.27}$$

where k with $1 \leq k \leq ne_s$ is a local index, counting the particles $\mathcal{P}_j$ in each stencil, $j = j(k)$ is the mapping from the local index k to the global indexation of the particles in the computational domain Ω, ne_s is the number of particles in each stencil and n_s is the number of stencils. As in the mesh-based WENO scheme [*Dumbser and Kaëser*, 2007; *Dumbser et al.*, 2007] the set of stencils consists of one central stencil $\mathcal{S}_0^i$ and a set of one-sided stencils ($1 \leq s \leq 8$). We choose 8 one-sided stencils to cover all possible directions. Fig. 2.2 shows a sketch of the stencils associated to the particle $\mathcal{P}_i$. The first stencil, i.e. the central stencil, is obtained by the union of the central particle $\mathcal{P}_i$ and its surrounding particles $\mathcal{P}_j$ as

$$\mathcal{S}_0^i = \bigcup_k^{ne_s} \mathcal{P}_{j(k)}, \qquad \|\mathbf{r}_{ij}\| \leq h_{i,mls}, \tag{2.28}$$

while the one-sided stencils are defined as :

$$\mathcal{S}_s^i = \bigcup_k^{ne_s} \mathcal{P}_{j(k)}, \quad \|\mathbf{r}_{ij}\| \leq 2h_{i,mls} \quad \text{and} \quad \theta \in [(s-1)\pi/4, s\pi/4], \tag{2.29}$$

where $h_{i,mls}$ is a characteristic length scale defined later and θ is the angle formed by the vector $\mathbf{r}_{ij} = \mathbf{r}_j - \mathbf{r}_i$ connecting the two particles $\mathcal{P}_i$ and $\mathcal{P}_j$ and the x-axis,

$$\tan(\theta) = \frac{y_j - y_i}{x_j - x_i}. \tag{2.30}$$

In practice, the particle search algorithm for defining the reconstruction stencils $\mathcal{S}_s^i$ is implemented as follows. The computational domain is covered by a fixed virtual Cartesian background grid of size $2\max(h_{i,mls})$, the so-called book-keeping cells or macro-cells, see e.g. *Hockney and Eastwood* [1981]; *Monaghan* [1992, 1994, 2005]; *Ferrari et al.* [2009]. At the beginning of each Runge-Kutta substage, each particle can be easily located on this background grid and is added into a linked list associated with the corresponding Cartesian macro-cell containing the particle. Then, the stencil search algorithm for particle $\mathcal{P}_i$ loops over the linked list associated with the macro-cell containing particle $\mathcal{P}_i$ and over the linked lists of the neighbors of the book-keeping cell containing $\mathcal{P}_i$. It stops when the necessary number of particles ne_s has been found. In cases where it is not possible to find enough particles for a stencil (e.g. on the boundary of the computational domain), the corresponding stencil is simply deactivated.

After this definition of several candidate stencils, which is in common with mesh-based WENO schemes, we apply a Moving-Least-Squares interpolation. In particular, for each particle the reconstruction polynomials assume the following form:

$$\mathbf{Q}_i^s(\xi,\eta) = \mathbf{Q}_i + \sum_{1\leq|m|\leq M} \widehat{\mathbf{w}}_{m,s}\phi_m(\xi,\eta), \tag{2.31}$$

for each of the nine stencils $\mathcal{S}_s^i$ (Fig. 2.2). In Eqn. (3.16) ξ and η are normalized spatial coordinates in a 2D reference coordinate system defined as $\xi = (x-x_i)/h_{i,mls}$ and $\eta = (y-y_i)/h_{i,mls}$, where x_i and y_i denote the position of the *i-th* particle in the global coordinate system while $\widehat{\mathbf{w}}_{m,s}$ denotes the set of unknown coefficients of the reconstruction polynomial on stencil number s and ϕ_m are the associated basis functions. With the basis functions given in Eqn. (3.18) below, the series in Eqn. (3.16) is a Taylor series expansion of order M around the position of the particle $\mathcal{P}_i$. The number of unknown coefficients and basis functions in Eqn. (3.16) is given by $nc-1$. In two space dimensions nc is defined as

$$nc = \frac{(M+2)(M+1)}{2}. \tag{2.32}$$

Finally, the basis functions $\phi_m(\xi,\eta)$ in Eqn. (3.16) are defined as

$$\phi_m(\xi,\eta) = \xi^m, \tag{2.33}$$

with $\xi = (\xi,\eta)$ and the multi-index m with $0 < |m| \leq M$. The use of reference coordinates ξ and η helps to avoid ill-conditioned reconstruction matrices. The unknown coefficients

$\widehat{\mathbf{w}}_{m,s}$ are computed on each stencil $\mathcal{S}_s^i$ from the following set of reconstruction equations:

$$\sum_{m=1}^{nc-1} \phi_m\left(\xi_j,\eta_j\right)\widehat{\mathbf{w}}_{m,s} = \mathbf{Q}_j - \mathbf{Q}_i, \qquad \forall \mathcal{P}_j \in \mathcal{S}_s^i. \tag{2.34}$$

According to eqn. (3.19) we interpret the SPH data as local point-values, i.e. in a finite-difference manner. Although eqn. (2.13) would suggest a finite-volume type interpretation, it is not clear how to define the control volumes in a meshless particle method, and even a kernel-weighted volume integral would be very difficult and expensive to carry out. We therefore opted for the expression (3.19) above, which is easy to implement and in which data are well-defined as local point values. Further investigations concerning a finite-volume type reconstruction are still necessary, but are beyond the scope of this chapter. The number of particles ne_s in each stencil $\mathcal{S}_s^i$ is chosen in such a way that the number of equations in the system (3.19) is *larger* that the number of unknown degrees of freedom, hence $ne_s > nc$. Therefore, Eqn. (3.19) constitutes an overdetermined linear algebraic system for the coefficients, which is solved using a least square technique [*Barth and Frederickson*, 1990; *Agossler Albert*, 2001; *Dumbser et al.*, 2008a,b]. In order to ensure linear stability, we suggest to use at least $ne_s = 2nc$ particles in each stencil for linear stability purposes [*Dumbser and Kaëser*, 2007; *Dumbser et al.*, 2007].

As in mesh-based WENO schemes, see for example [*Jiang and Shu*, 1996; *Hu and Shu*, 1999; *Balsara and Shu*, 2000; *Titarev et al.*, 2010; *Tsoutsanis et al.*, 2011], the final non-linear WENO reconstruction polynomial $Q_i(\xi,\eta)$ of degree M is obtained by a non-linear combination of the nine polynomials $Q_i^s(\xi,\eta)$ of degree M reconstructed on the n_s stencils:

$$\mathbf{Q}_i(\xi,\eta) = \sum_{s=0}^{n_s-1} \omega_s \mathbf{Q}_i^s(\xi,\eta), \tag{2.35}$$

with the normalized nonlinear weights

$$\omega_s = \frac{\tilde{\omega}_s}{\sum\limits_{r=1}^{n_s} \tilde{\omega}_r}, \tag{2.36}$$

with $\tilde{\omega}_s$ that assume the following form [*Dumbser et al.*, 2008a,b]:

$$\tilde{\omega}_s = \frac{\lambda_s}{\left(\varepsilon+\sigma_s\right)^r}, \tag{2.37}$$

where $\varepsilon = 10^{-14}$, $r = 4$ and the linear weights are set to $\lambda_0 = 10^5$ for the central stencil and $\lambda_s = 1$ for the one-sided stencils $(1 \leq s \leq 8)$. Finally, due to the complexity of mesh-free methods we propose to compute the smoothness indicator in a very simple manner that is independent of the current particle distribution:

$$\sigma_s = \sum_{1 \leq |m| \leq M} \widehat{\mathbf{w}}_{m,s}^2. \tag{2.38}$$

As for standard WENO schemes, the reconstruction can be carried out either in conservative variables or in local characteristic variables [*Jiang and Shu*, 1996; *Titarev and Toro*, 2004]. In the first case the expressions (3.16)-(2.38) are used for each component of the vector of conservative variables $\mathbf{Q}$. In the second case we first transform conservative variables to characteristic variables along the velocity vector $\mathbf{v}_i$ (since there is no preferred direction in SPH schemes) and then we transform back to conservative variables.

Finally, as for the smoothing length in the kernel interpolation, we introduce a variable stencil length h_{mls} for each particle $\mathcal{P}_i$:

$$h_{i,mls} = \sigma_{mls} \sqrt[\nu]{V_i} \tag{2.39}$$

with σ_{mls} a suitable constant. This ensures that enough particles are found in at least one of the nine stencils also where particle density is low. In our numerical experiments we found also that a lower bound ensures robustness to the meshfree WENO reconstruction, although more numerical experiments in this direction would be desirable.

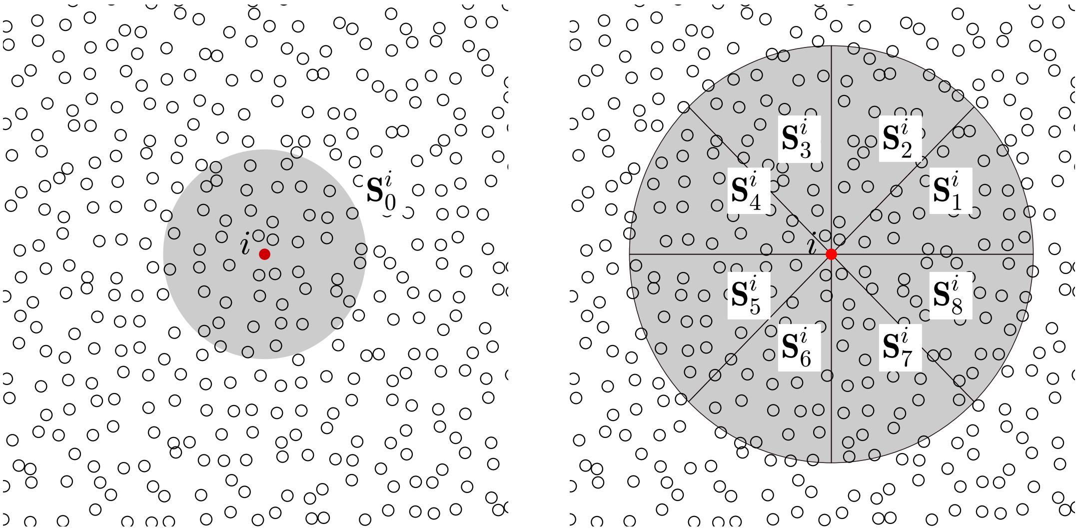

(a) *Central stencil.* **(b)** *One-sided stencils.*

Figure 2.2: *Sketch of the central and one-sided WENO reconstruction stencils for a random particle distribution. The particle* $\mathcal{P}_i$ *is shown in red color.*

2.4 Numerical Test Cases

In the following section we first verify the effectiveness of the Moving-Least-Squares WENO reconstruction in approximating a function from given point values, and successively we compare MWSPH with the standard SPH scheme and the V-B-SPH scheme. Furthermore, comparisons against exact or numerical reference solutions are provided in one- and two-dimensional setups. As discussed in [*Ferrari et al.*, 2009] the semi-discrete form of SPH reduces the original PDE system (2.1) to a set of nonlinear ordinary differential equations (ODEs), which can be solved by using any stable time integration algorithm [*Ferrari et al.*, 2009; *Monaghan*, 2005]. In the present work we adopt the third order TVD Runge-Kutta scheme [*Gottlieb and wang Shu*, 1998].

2.4.1 Assessment of the MLS-WENO reconstruction

The high order MLS reconstruction is the most important step in our MWSPH scheme and represents the main novelty with respect to existing SPH schemes. Therefore, the accuracy of the new Moving-Least-Squares-WENO (MLS-WENO) method in reconstructing a known function from given point values is first verified for the case of a continuous and then for a piecewise continuous function. We point out that here we focus on WENO combined with Moving-Least-Squares, here referred as MLS-WENO, and not on the entire MWSPH scheme. The numerical results from the standard SPH are given for comparison. Also in this case we use SPH only to compute reconstructed point values. The assessment is carried out by assigning a point value of a known function to each particle and then obtaining reconstructed values on a different regular Cartesian lattice. The particles are distributed in a circle of radius $R = 1.0$, with the center located at $(0,0)$. We consider both, equidistant and non-equidistant particle distributions within the computational domain (see Figs. 2.3a and 2.3b). The latter case is obtained by perturbing the initial position of the particles, at the nodes of a regular grid with spacing $\Delta x = \Delta y$, with pseudo-random numbers from the uniform distribution within the range $[0,1]\Delta x$. Testing the MLS-WENO scheme with an irregular particle distribution is important because in SPH schemes particles move according to the local fluid velocity field resulting in the distortion of initially regular positions. Fig. 2.3 shows the regular lattice where the reconstructed values are computed and compared with the exact solution as well as the particle positions for both equidistant and non-equidistant cases.

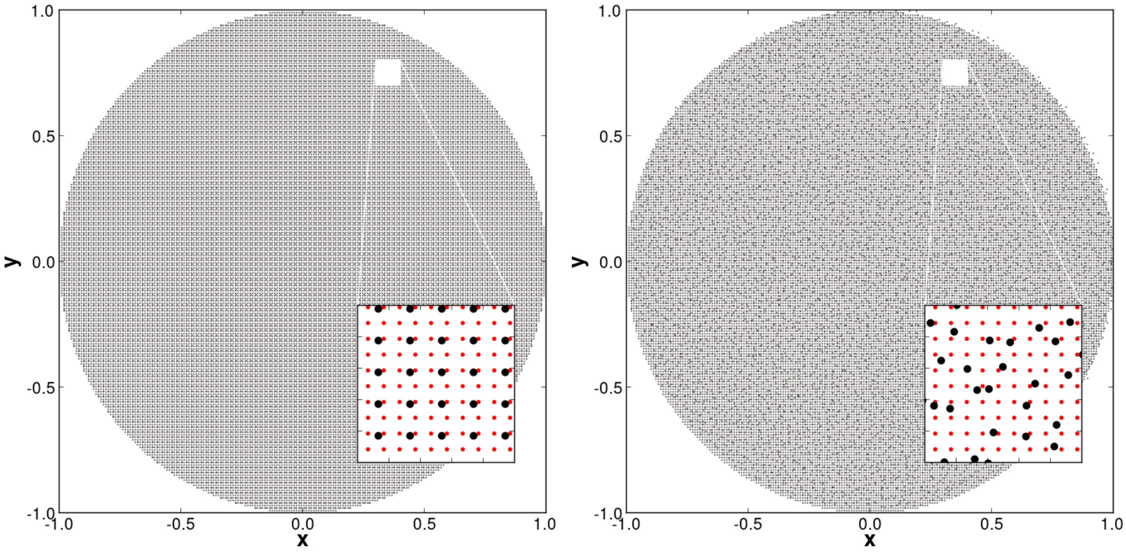

(a) *Equidistant particle distribution.* **(b)** *Random particle distribution.*

Figure 2.3: *Equidistant particle distribution on the left panel and non-equidistant particle distribution on the right panel. Particles are in black. The regular Cartesian lattice used for verification of the reconstruction is shown in red.*

2.4.1.1 Reconstruction of a smooth function

In this test case we perform the reconstruction of a smooth function on the grid shown in Fig. 2.3 where particle $\mathcal{P}_i$ takes the value $Q_i(x_i, y_i) = Q_e(x_i, y_i)$, with

$$Q_e(x,y) = e^{-0.2(x+y)} \left(\cos(4x) + \sin(4y)\right), \tag{2.40}$$

and where (x_i, y_i) denotes the particle position within the computational domain. Fig. 2.4 shows the reconstructed results for the function for both equidistant and non-equidistant particle distributions. In all cases MLS-WENO produces excellent approximations while SPH shows significant deviations from the original function. In the case of equidistant particles SPH underestimates the exact solution and spurious oscillations emerge when the particles are not equidistant. A quantitative comparison of the accuracy of the schemes is offered by the L_p norm:

$$L_q = \left(\sum_{j=1}^{N} \left| Q_i(x'_j, y'_j) - Q_e(x'_j, y'_j) \right|^q \right)^{(1/q)} /N, \tag{2.41}$$

where $Q_e(x'_j, y'_j)$ is the given exact solution at (x'_j, y'_j) and $Q_i(x'_j, y'_j)$ is the reconstructed value. Notice that the (x'_j, y'_j) are the coordinates of the regular lattice used for verification of the reconstruction and is not identical with the original particle positions. The L_∞ norm is computed by taking the maximum error among all vertices. As expected, MLS-WENO reaches the nominal order $M+1$, regardless of the distribution of the particles (Table 2.1). This is in agreement with mesh-based WENO scheme developed in [*Dumbser and Kaëser*, 2007] and [*Dumbser et al.*, 2007] and here extended to the meshfree case. On the contrary, SPH exhibits a convergence rate $O(h^2)$ in case of equidistant particles and lower order convergence for non-equidistant particles.

dx	ε_{L_1}	ε_{L_2}	ε_{L_2}	$O(L_1)$	$O(L_2)$	$O(L_\infty)$	$t_{CPU}(s)$
SPH $\sigma = 2$ *equidistant particles*							
0.40E-01	0.52E-01	0.66E-01	0.16E+00	-	-	-	0.50
0.20E-01	0.13E-01	0.17E-01	0.41E-01	1.98	1.98	1.98	2.24
0.10E-01	0.34E-02	0.42E-02	0.11E-01	2.00	2.00	1.98	8.49
0.50E-02	0.84E-03	0.11E-02	0.27E-02	2.01	2.00	1.95	33.01
0.25E-02	0.21E-03	0.27E-03	0.79E-03	2.02	1.99	1.80	133.76
SPH $\sigma = 2$ *non-equidistant particles*							
0.40E-01	0.65E-01	0.97E-01	0.39E+00	-	-	-	0.42
0.20E-01	0.41E-01	0.63E-01	0.39E+00	0.67	0.62	0.01	1.72
0.10E-01	0.39E-01	0.61E-01	0.40E+00	0.09	0.04	-0.04	7.75
0.50E-02	0.39E-01	0.62E-01	0.53E+00	-0.01	-0.02	-0.39	31.89
0.25E-02	0.39E-01	0.62E-01	0.55E+00	0.01	0.00	-0.07	137.50
$MW-WENO\ (O3)\ \sigma_{mls} = 4$ *equidistant particles*							
0.40E-01	0.70E-03	0.91E-03	0.42E-02	-	-	-	1.42
0.20E-01	0.43E-04	0.59E-04	0.32E-03	4.04	3.99	3.73	6.02
0.10E-01	0.23E-05	0.35E-05	0.37E-04	4.23	4.07	3.16	24.20
0.50E-02	0.11E-06	0.17E-06	0.21E-05	4.40	4.39	4.10	97.12
0.25E-02	0.56E-08	0.88E-08	0.13E-06	4.30	4.28	4.03	398.68
$MW-WENO\ (O3)\ \sigma_{mls} = 4$ *non-equidistant particles*							
0.40E-01	0.74E-03	0.11E-02	0.66E-02	-	-	-	1.39
0.20E-01	0.44E-04	0.68E-04	0.77E-03	4.09	4.03	3.13	5.83
0.10E-01	0.27E-05	0.42E-05	0.52E-04	4.05	4.03	3.91	23.03
0.50E-02	0.17E-06	0.26E-06	0.33E-05	4.02	4.02	3.98	93.77
0.25E-02	0.10E-07	0.16E-07	0.23E-06	4.01	4.01	3.84	412.10

Table 2.1: *Numerical convergence results for smooth function reconstruction with second, third and fourth order version of the MLS-WENO scheme. In the first row the particles distance dx. The second, third and fourth columns contain the error measured in* L_1*,* L_2 *and* L_∞ *norms, followed by three columns giving the measured order of accuracy between the respective particles and the previous particles distributions. The last row gives the CPU time needed by the serial code on one Intel(R) Core(TM) i7-2640M CPU with 2.80GHz and 8 GB of RAM.*

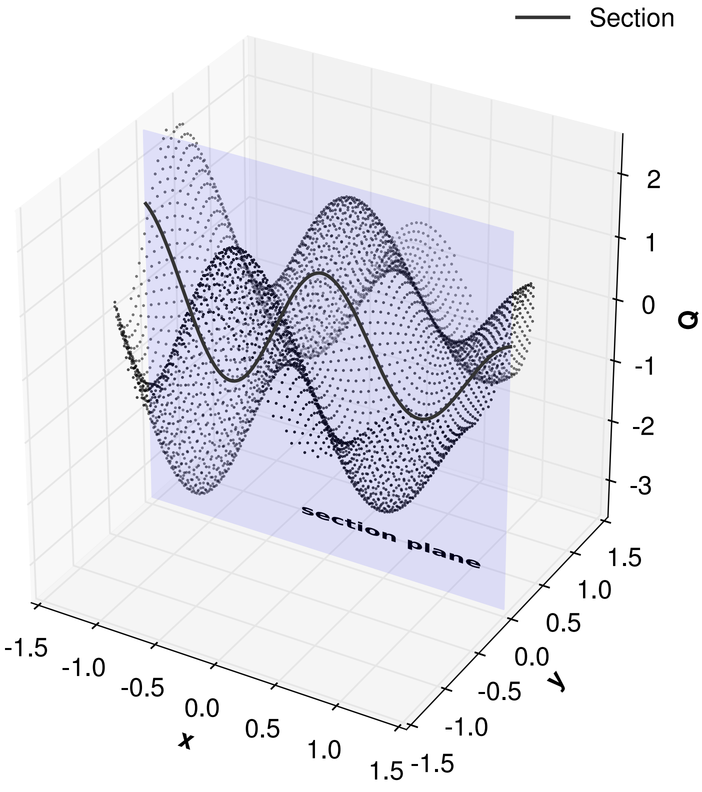
Section
section plane
2
1
0
-1
-2
-3
Q
-1.5
-1.0
-0.5
0.0
0.5
1.0
1.5
x
-1.5
-1.0
-0.5
0.0
0.5
1.0
1.5
y

(a)

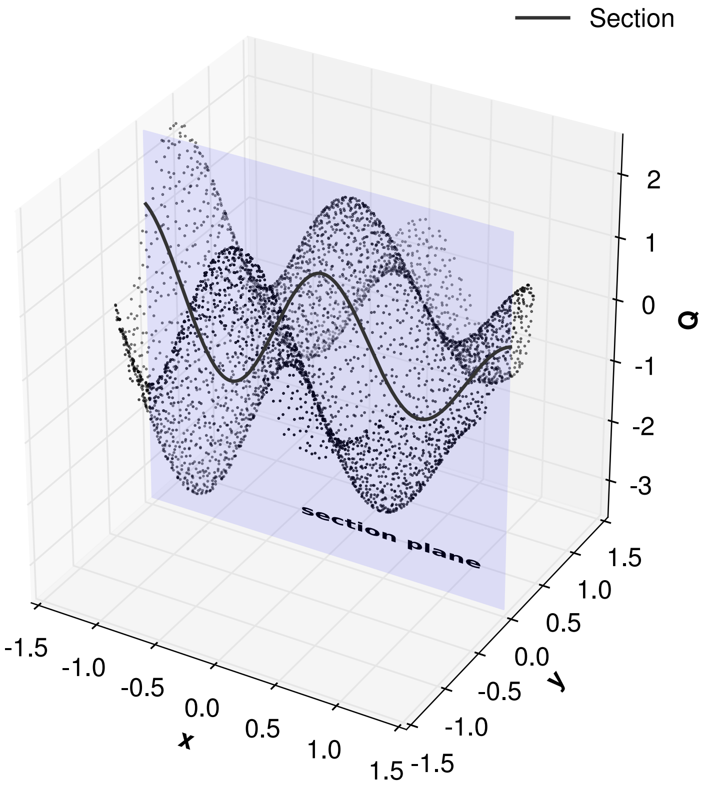
Section
section plane
2
1
0
-1
-2
-3
Q
-1.5
-1.0
-0.5
0.0
0.5
1.0
1.5
x
-1.5
-1.0
-0.5
0.0
0.5
1.0
1.5
y

(b)

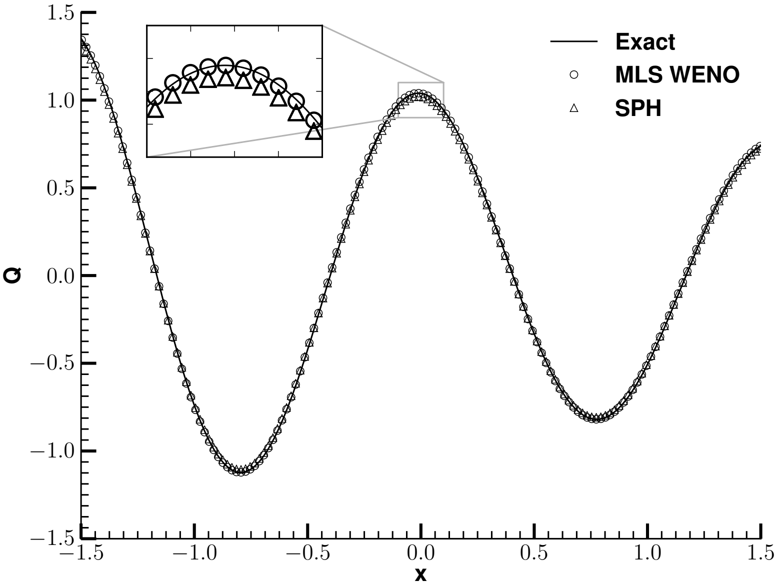

(c)

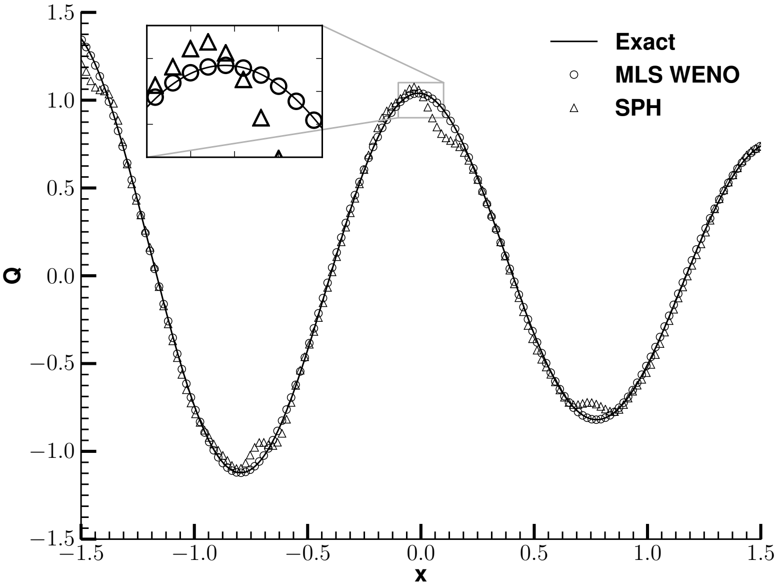

(d)

Figure 2.4: *Comparison of the exact function and the reconstruction for the smooth case computed with standard SPH and with the new MLS-WENO. Particle values on computational domain with equidistant distribution **(a)** and non-equidistant distribution **(b)**. Cut through the reconstruction at $y = 0$ for equidistant particles **(c)** and non-equidistant particles **(d)**.*

2.4.1.2 Reconstruction of a piecewise smooth function

In this additional example the imposed function is piecewise continuous according to:

$$Q_e(\mathbf{r}) = \begin{cases} 2.5, & \text{if } \|\mathbf{r}\| \leq 0.2, \\ 2, & \text{if } 0.2 < \|\mathbf{r}\| \leq 0.4, \\ \|\mathbf{r}\| - 0.2, & \text{if } 0.4 < \|\mathbf{r}\| \leq 0.6, \\ (0.6 - \|\mathbf{r}\|)^2 + 2.2, & \text{if } 0.6 < \|\mathbf{r}\| \leq 1, \end{cases} \tag{2.42}$$

where **r** is the position vector in the computational domain. Figs. 2.5a and 2.5b show particle positions and reconstructed values for both cases: equidistant and non-equidistant. From Figs. 2.5c and 2.5d one can notice that standard SPH does not correctly capture the discontinuities, especially for the non-equidistant case. This is due to well known inconsistency problems of the standard SPH [*Monaghan*, 2005]. Instead, the new MLS-WENO formulation not only successfully reconstructs the piecewise smooth function at discontinuities, but also at the boundary. We believe that this is an important result. Unlike DSPH [*Liu et al.*, 2003a; *Xu et al.*, 2013], we show that we have an automatic treatment and detection of both the discontinuity and boundary conditions where no oscillations are present. However, concerning the implementation of reflective wall boundary conditions or inflow and outflow boundaries, our approach has the same difficulties as any other SPH scheme.

(*This page has been intentionally left blank*)

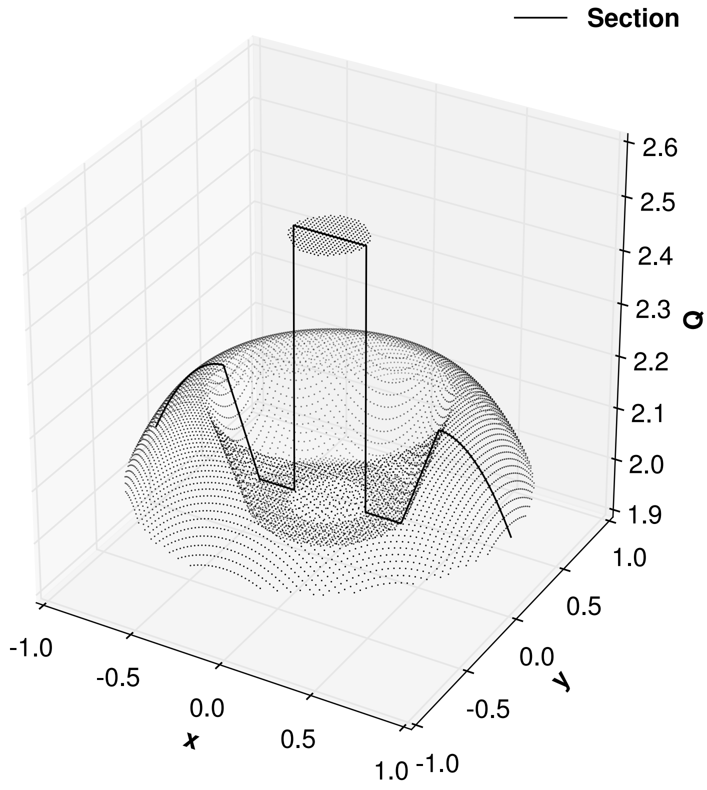

(a) *Equidistant particle distribution.*

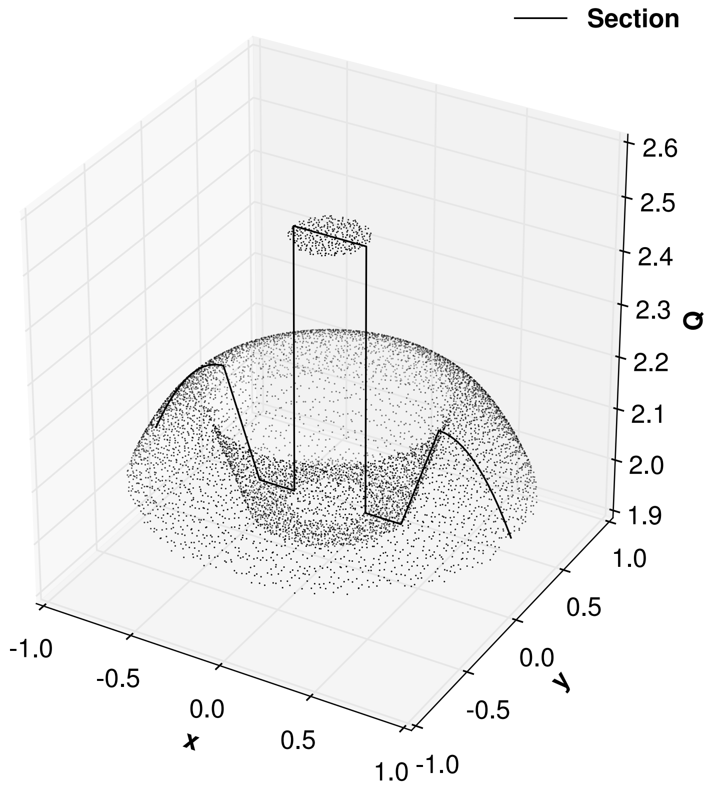

(b) *Random particle distribution.*

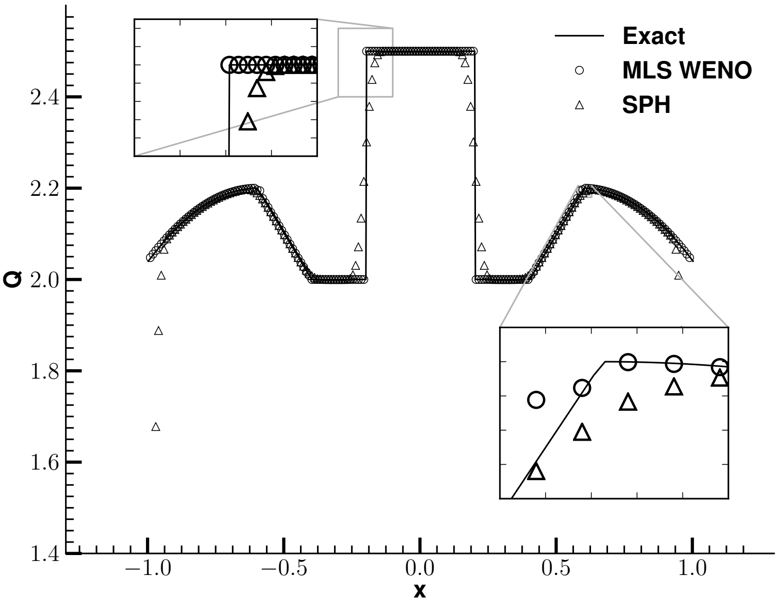

(c) *Equidistant particle distribution.*

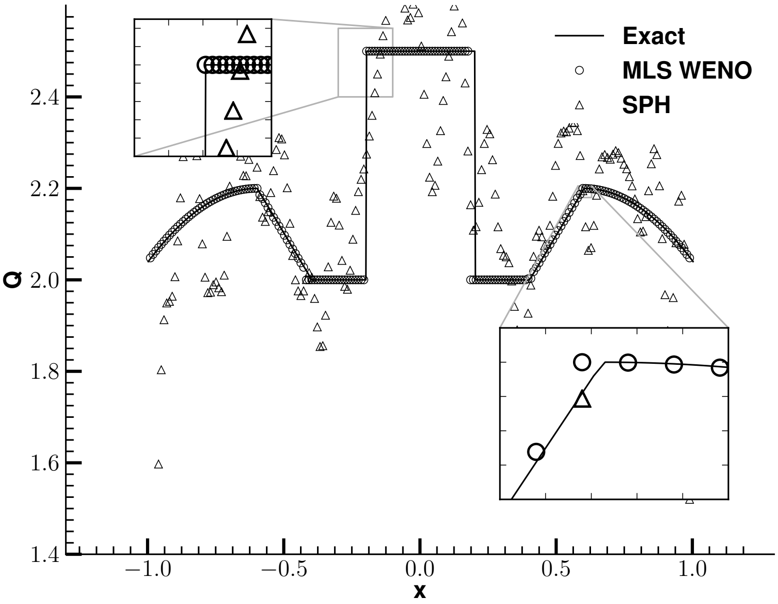

(d) *Random particle distribution.*

Figure 2.5: *Comparison of the exact function and the reconstruction for the piecewise smooth case computed with standard SPH and with the new MLS-WENO. Particle values on computational domain with equidistant distribution **(a)** and non-equidistant distribution **(b)**. Cut through the reconstruction at* $y = 0$ *for equidistant particles **(c)** and non-equidistant particles **(d)**.*

2.4.2 Circular blast wave problems

We consider a two dimensional blast wave problem with initial data taken from the 1D Sod problem [*Sod*, 1978]. The domain has a circular shape with radius $R = 1.5$ and center in $(0,0)$. The computational domain is discretized with 70933 particles located on a regular and radially symmetric grid, Fig. 2.6. We consider the following initial condition:

$$(\rho, u, v, p)(\mathbf{r}, 0) = \begin{cases} (\rho_{in}, 0, 0, p_{in}), & \text{if } \|\mathbf{r}\| \leq 0.5, \\ (\rho_{out}, 0, 0, p_{out}), & \text{otherwise}, \end{cases} \tag{2.43}$$

where the subscripts *in* and *out* denote the inner and the outer states, similar to the left and right states of a classic Riemann problem in 1D, see Tables 2.2 and 2.3. The numerical results are compared with a radial reference solution of the one-dimensional Euler equations with a geometrical source term, see section 17.5 of *Toro* [1997] for details.

	ρ	u	v	p
$\mathbf{Q}_{in}$	1.0	0.0	0.0	1.0
$\mathbf{Q}_{out}$	0.125	0.0	0.0	0.1

Table 2.2: *Initial states $\mathbf{Q}_{in}$ (inner) and $\mathbf{Q}_{out}$ (outer) for the first 2D explosion problem (EP1).*

	ρ	u	v	p
$\mathbf{Q}_{in}$	1.0	0.0	0.0	2.0
$\mathbf{Q}_{out}$	1.0	0.0	0.0	1.0

Table 2.3: *Initial states $\mathbf{Q}_{in}$ (inner) and $\mathbf{Q}_{out}$ (outer) for the second 2D explosion problem (EP2).*

Blast wave problem EP1 Figs. 2.7 and 2.8 show a comparison between the reference solution, V-B-SPH and MWSPH respectively with $\sigma = 2$ and $\sigma_{mls} = 4$. We observe that the MWSPH produces a more accurate solution of the problem. The MWSPH captures the plateau in the density profile unlike the more dissipative V-B-SPH scheme, see Figs. 2.7c and 2.8c. This in clear also from Figs. 2.7a, 2.7b, 2.8b and 2.8a, where the density and pressure distributions on the z-plane are reported for MWSPH and V-B-SPH.

MWSPH and V-B-SPH do not exhibit spurious oscillations, which are observed in the standard SPH, Fig. 2.9. It is shown how MWSPH can handle correctly both, discontinuities

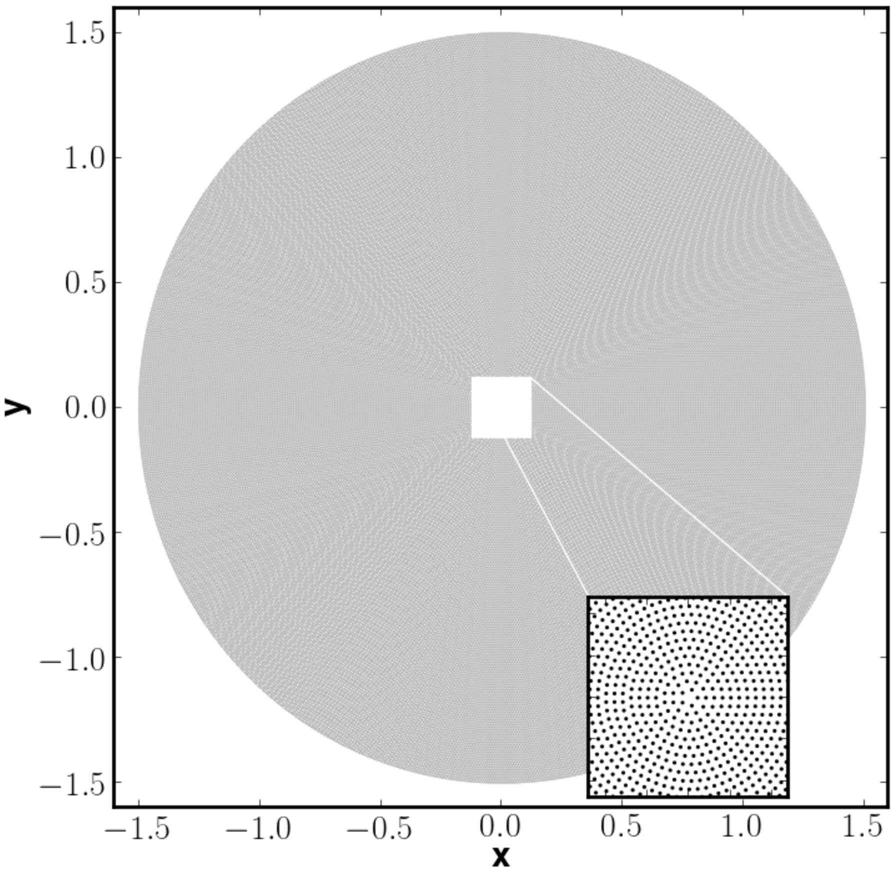

Figure 2.6: *Computational domain and initial particle distribution for the cylindrical explosion problem.*

and rarefaction waves. The use of the Osher-type flux further improves the accuracy of the numerical solution (Fig. 2.10). In particular the MWSPH scheme with Osher-type flux is able to resolve the contact wave in the density profile with only one intermediate point, as it should be for a Lagrangian scheme.

Fig. 2.12 shows the particle positions at the final time. The particle positions computed with V-B-SPH and MWSPH are more uniformly distributed than standard SPH particles. We notice both high particle density and low particle density regions. In both cases MWSPH can handle piecewise high order reconstructions thanks to a variable stencil width due to a variable smoothing length, see Eqn. (2.39).

Since the presented MWSPH scheme is an Arbitrary-Lagrangian-Eulerian scheme, where the particles could in principle move with an *arbitrary* velocity $\mathbf{v}$, we repeat the

MWSPH simulations for this test problem in an Eulerian framework where the particles are *fixed* and where the ALE flux simply reduces to the classical Eulerian flux, i.e. $\mathbf{H}(\mathbf{Q},\mathbf{v}) = \mathbf{F}(\mathbf{Q})$ by setting $\bar{\mathbf{v}}_{ij} = 0$. The results of the simulations are shown in Fig. 2.11, in direct comparison with the Lagrangian MWSPH results obtained previously. Again, the MWSPH results agree very well with the 1D reference solution, but this time the contact wave is subject to visible smearing due to the use of an Eulerian formulation while in the Lagrangian context the contact wave is much better resolved.

(*This page has been intentionally left blank*)

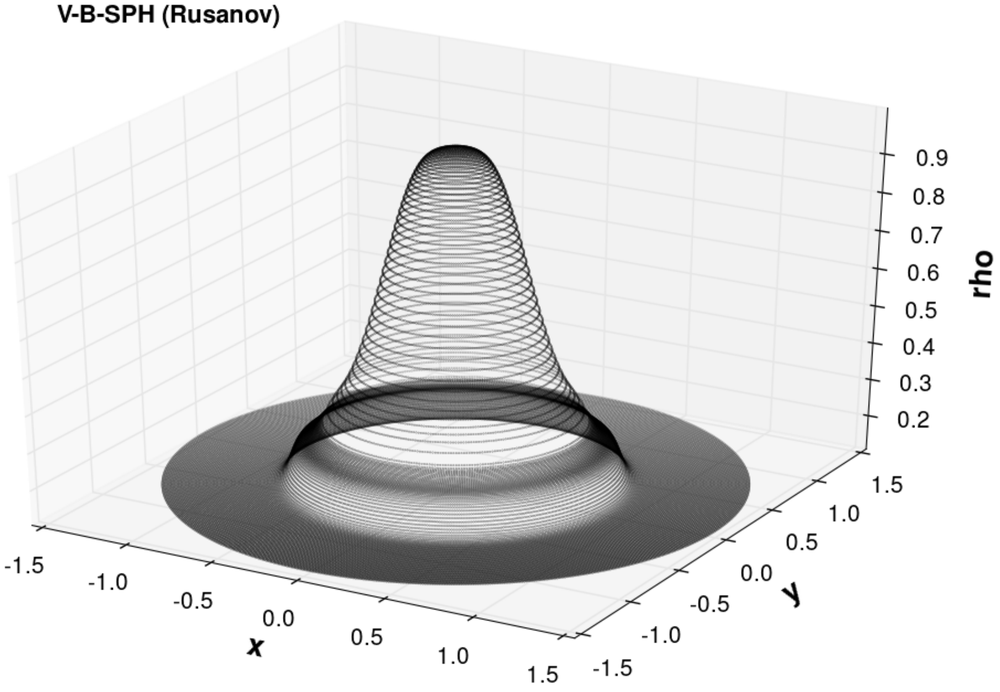
V-B-SPH (Rusanov)
rho
0.9
0.8
0.7
0.6
0.5
0.4
0.3
0.2
x
-1.5
-1.0
-0.5
0.0
0.5
1.0
1.5
y
-1.5
-1.0
-0.5
0.0
0.5
1.0
1.5

(a)

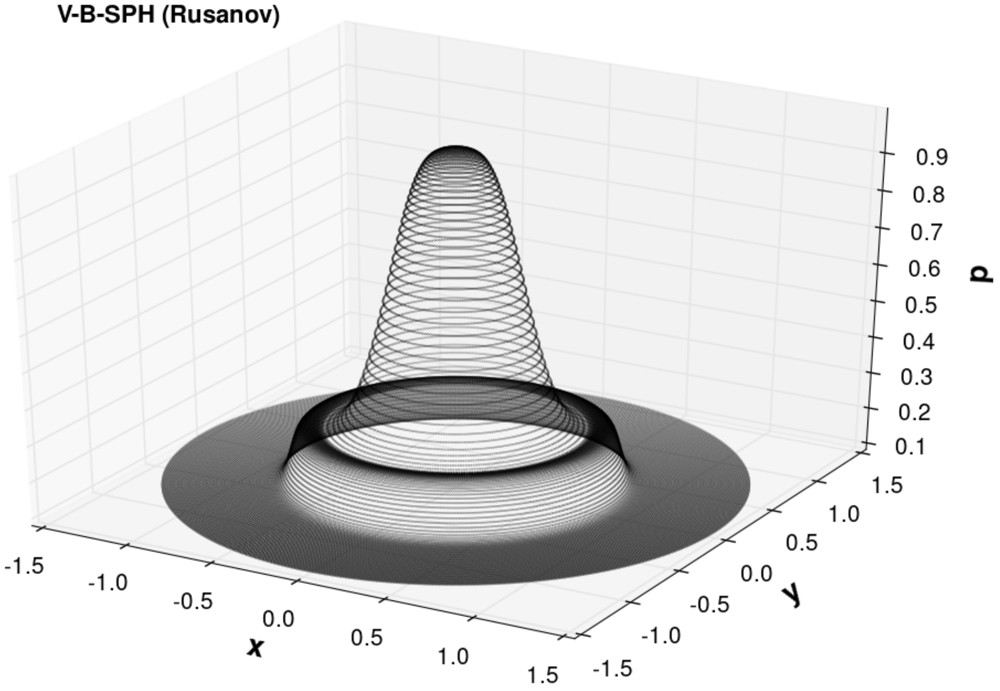
V-B-SPH (Rusanov)
p
0.9
0.8
0.7
0.6
0.5
0.4
0.3
0.2
0.1
x
-1.5
-1.0
-0.5
0.0
0.5
1.0
1.5
y
-1.5
-1.0
-0.5
0.0
0.5
1.0
1.5

(b)

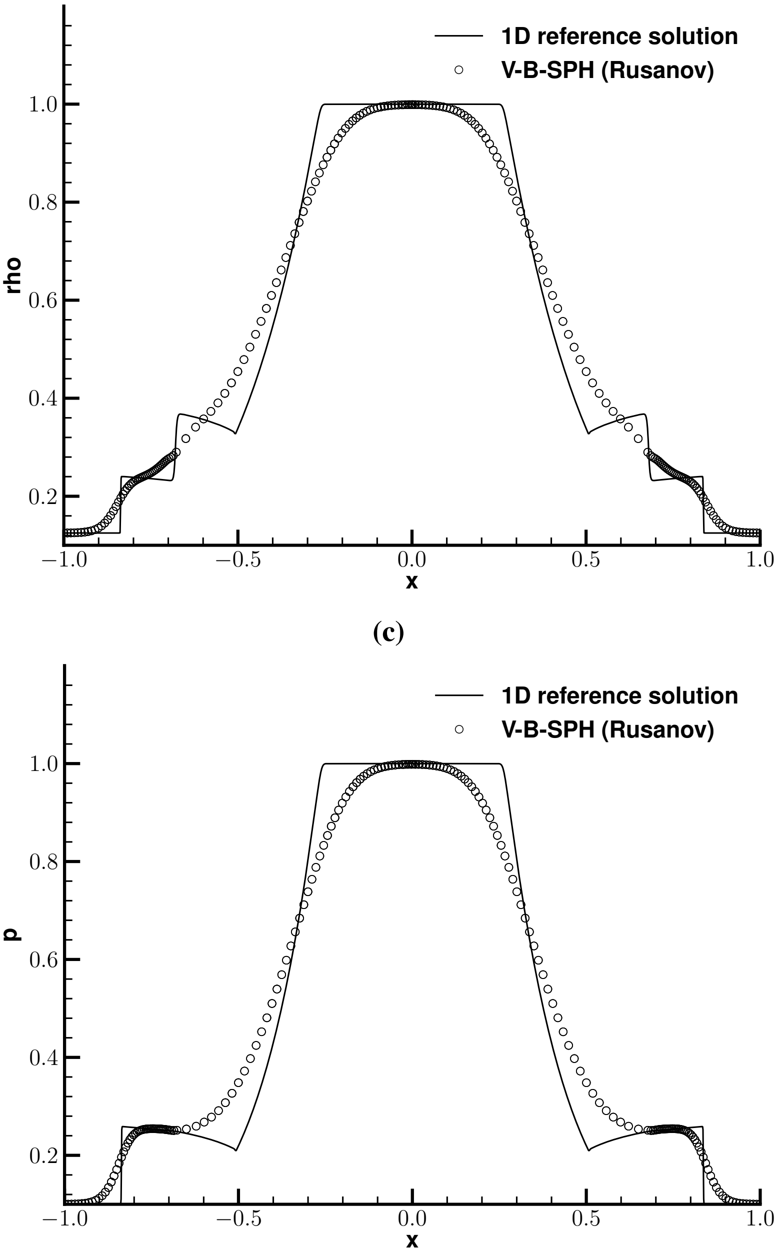

(c)

(d)

Figure 2.7: *Two dimensional numerical results of the blast wave problem with initial data given by Table 2.2 computed with V-B-SPH (Rusanov flux, $\sigma = 2$) at time $t = 0.2s$. Density and pressure **(a)**, **(b)**. Cut at $y = 0$ compared with 1D reference solution (continuous line) **(c)**, **(d)**.*

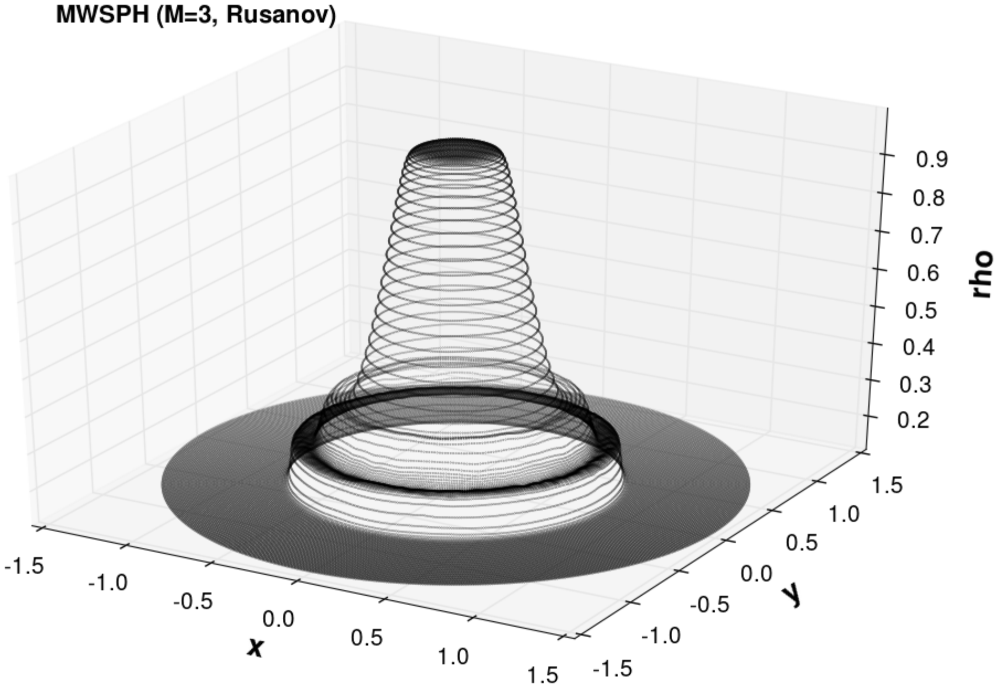
MWSPH (M=3, Rusanov)
rho
0.9
0.8
0.7
0.6
0.5
0.4
0.3
0.2
-1.5
-1.0
-0.5
0.0
0.5
1.0
1.5
x
1.5
1.0
0.5
0.0
-0.5
-1.0
-1.5
y

(a)

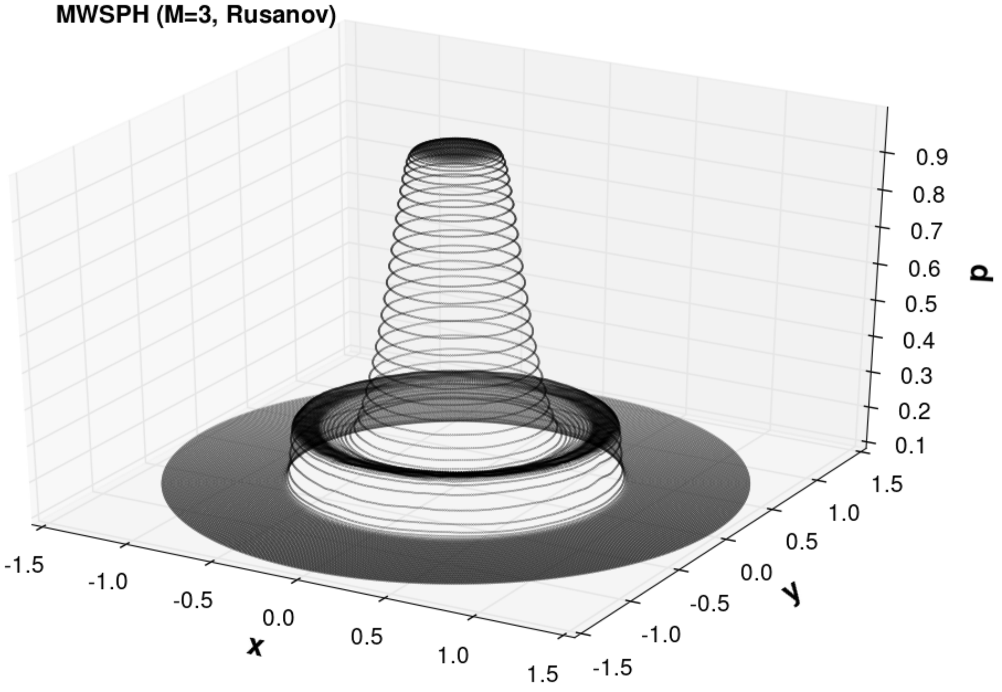
MWSPH (M=3, Rusanov)
p
0.9
0.8
0.7
0.6
0.5
0.4
0.3
0.2
0.1
-1.5
-1.0
-0.5
0.0
0.5
1.0
1.5
x
1.5
1.0
0.5
0.0
-0.5
-1.0
-1.5
y

(b)

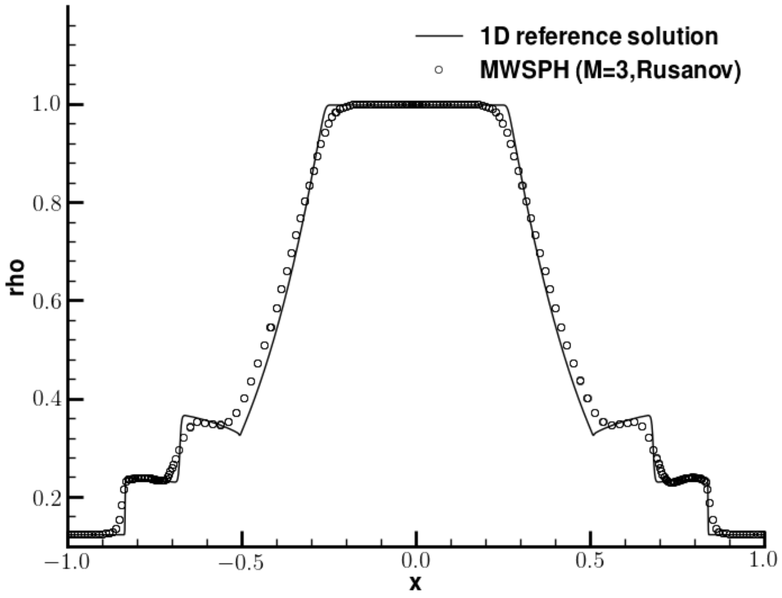

(c)

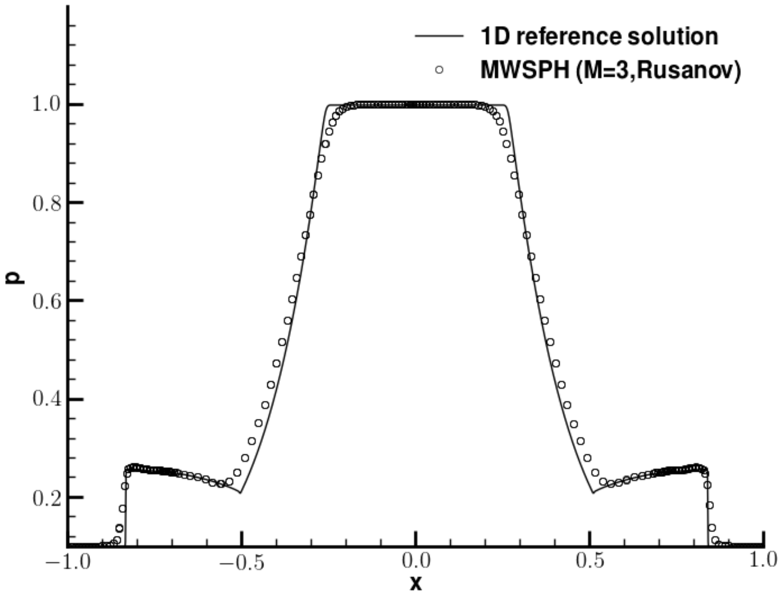

(d)

Figure 2.8: *Two dimensional numerical results of the blast wave problem EP1 with initial data given by Table 2.2 computed with MWSPH (Rusanov flux, $\sigma = 2$, $\sigma_{mls} = 4$, M=3) at time $t = 0.2s$. Density and pressure **(a)**, **(b)**. Cut at $y = 0$ compared with 1D reference solution (continuous line) **(c)**, **(d)**.*

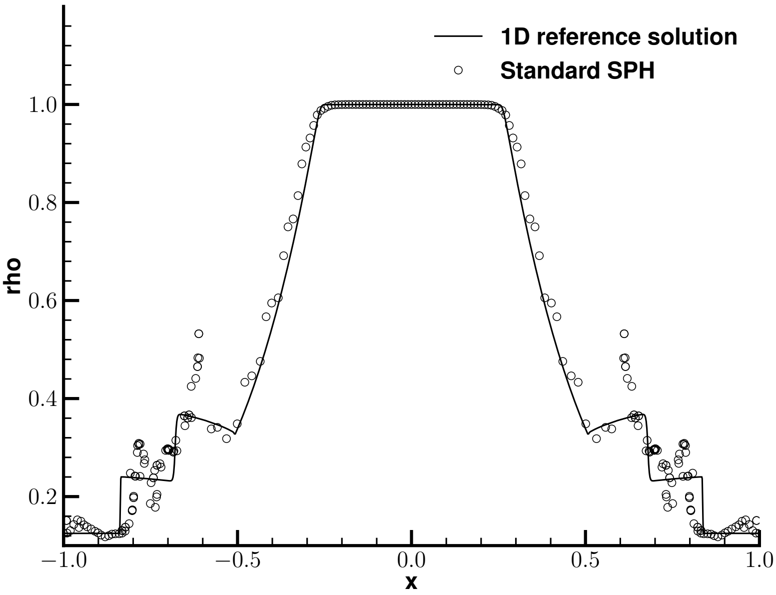

(a)

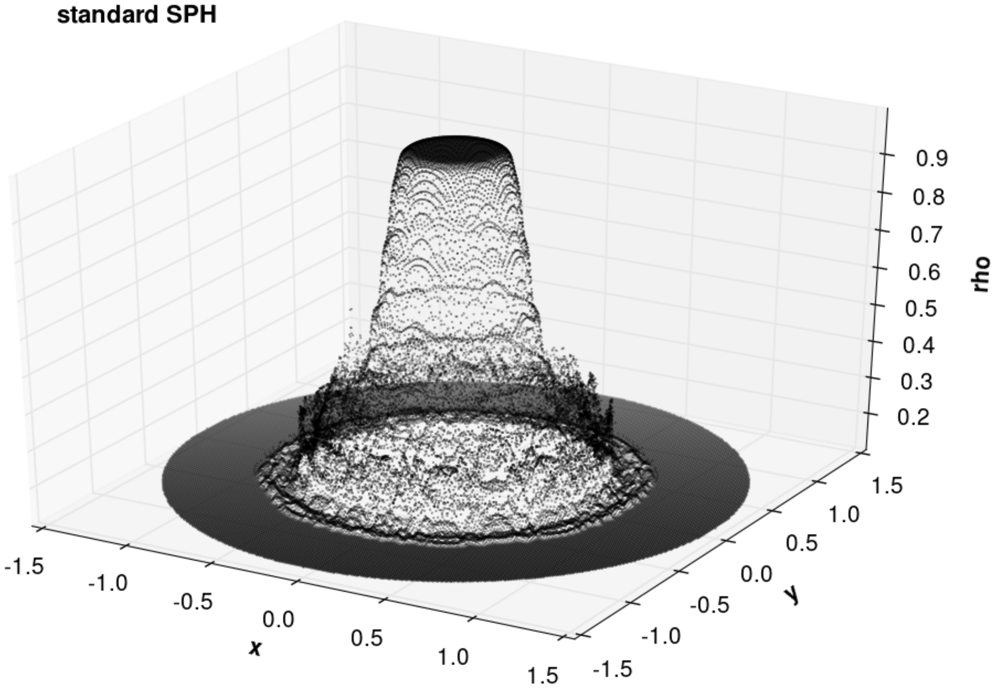

(b)

Figure 2.9: *Numerical results for EP1 obtained with the standard SPH at time* $t = 0.2s$*,* $\sigma = 2$*.*

(*This page has been intentionally left blank*)

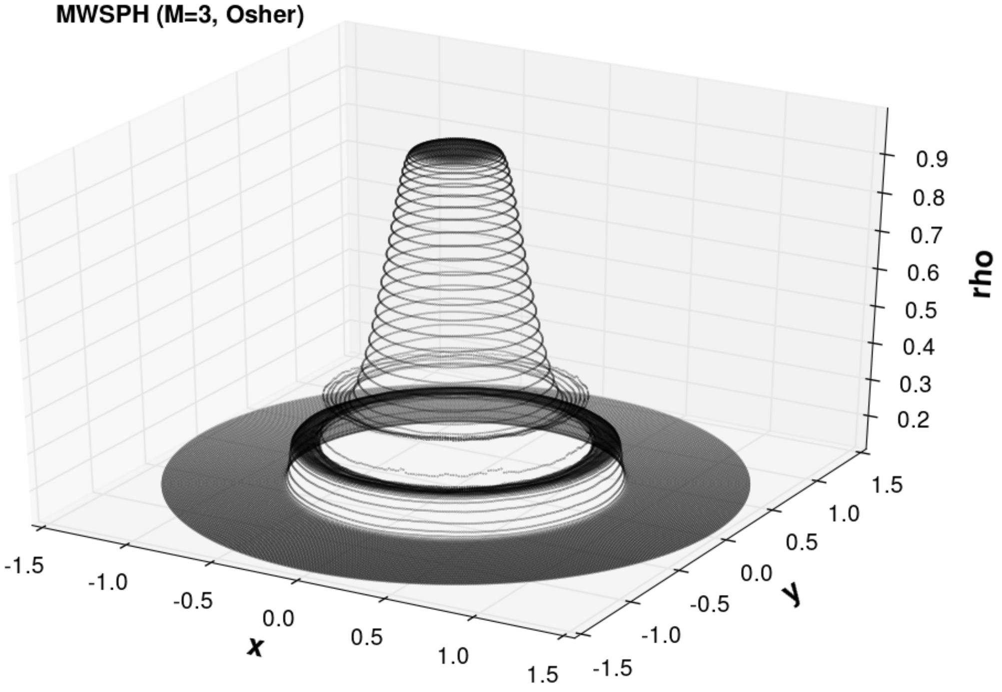
MWSPH (M=3, Osher)
rho
0.2
0.3
0.4
0.5
0.6
0.7
0.8
0.9
x
-1.5
-1.0
-0.5
0.0
0.5
1.0
1.5
y
-1.5
-1.0
-0.5
0.0
0.5
1.0
1.5

(a)

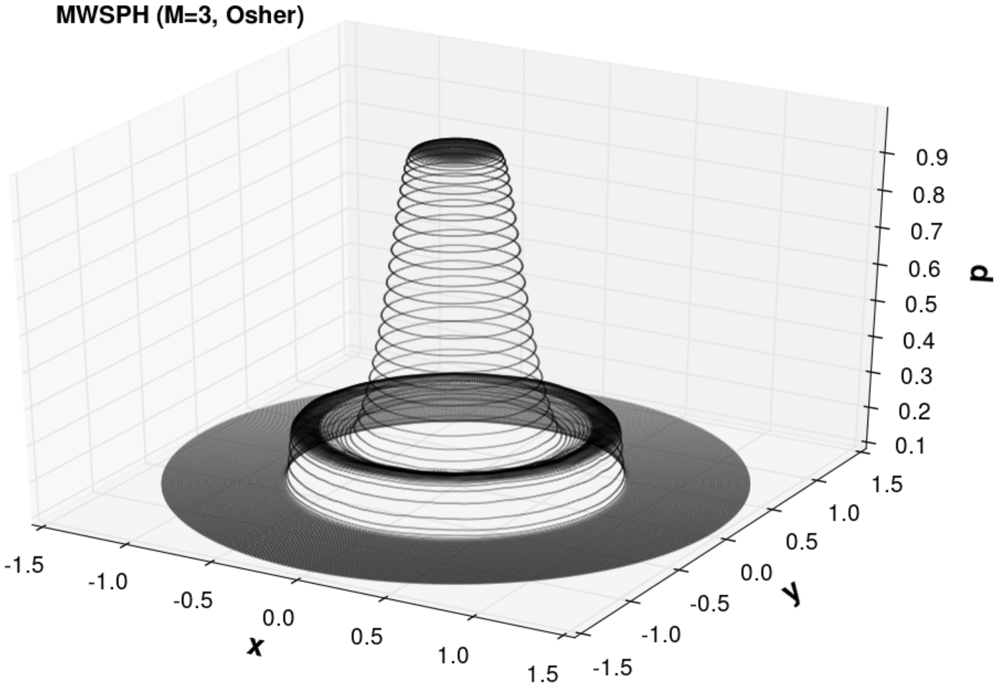
MWSPH (M=3, Osher)
p
0.1
0.2
0.3
0.4
0.5
0.6
0.7
0.8
0.9
x
-1.5
-1.0
-0.5
0.0
0.5
1.0
1.5
y
-1.5
-1.0
-0.5
0.0
0.5
1.0
1.5

(b)

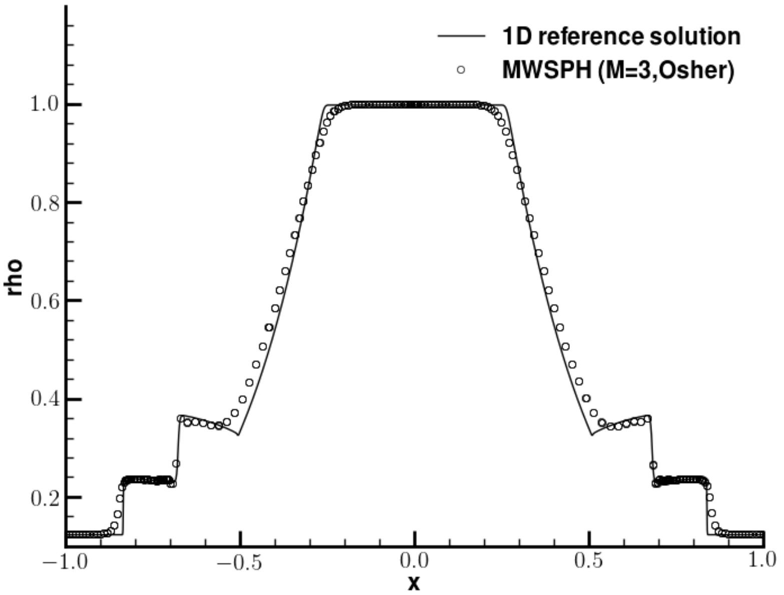

(c)

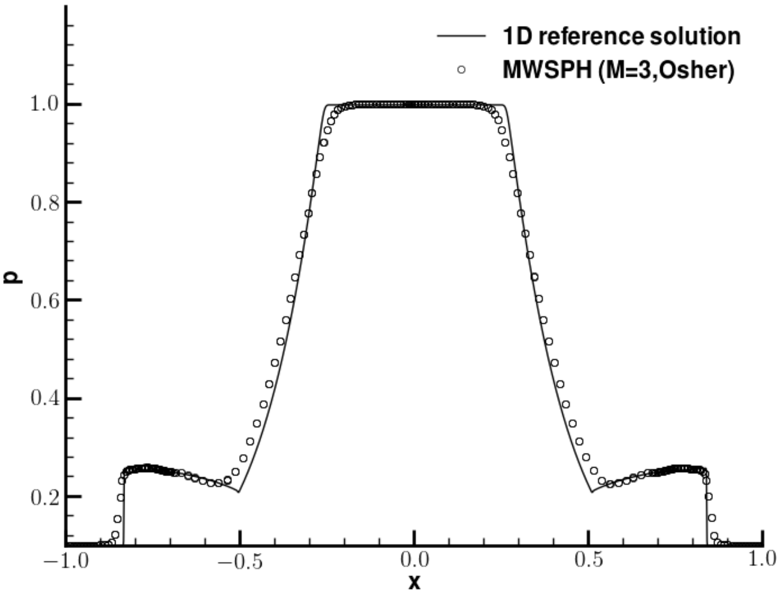

(d)

Figure 2.10: *Two dimensional numerical results of the blast wave problem EP1 with initial data given by Table 2.2 computed with MWSPH (Osher flux,* $\sigma = 2$, $\sigma_{mls} = 4$, *M=3) at time* $t = 0.2s$. *Density and pressure* ***(a)***, ***(b)***. *Cut at* $y = 0$ *compared with 1D reference solution (continuous line)* ***(c)***, ***(d)***.

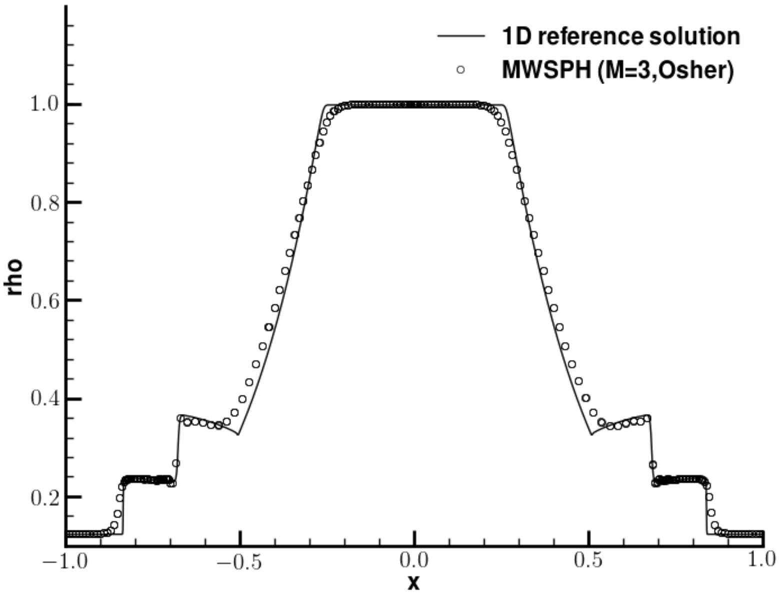

(a)

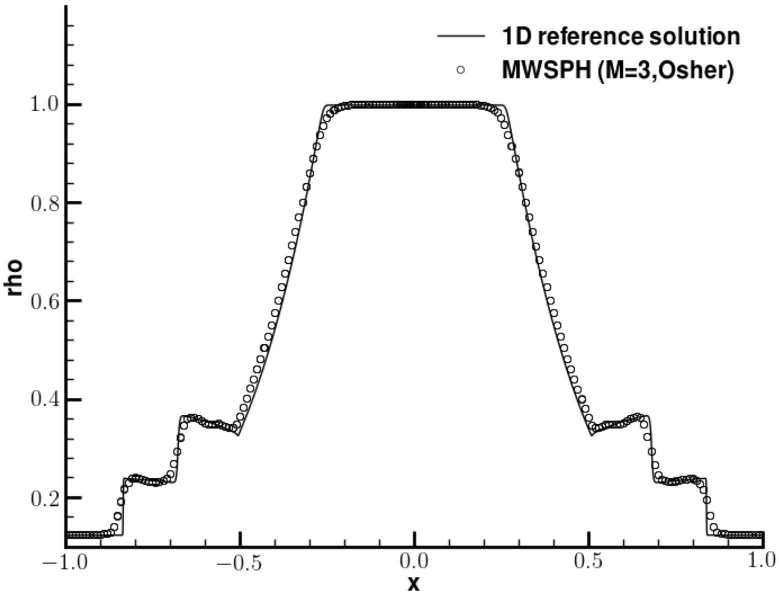

(b)

Figure 2.11: *Comparison of the Lagrangian MWSPH simulation with moving particles (top) and an Eulerian MWSPH simulation with fixed particles (bottom).*

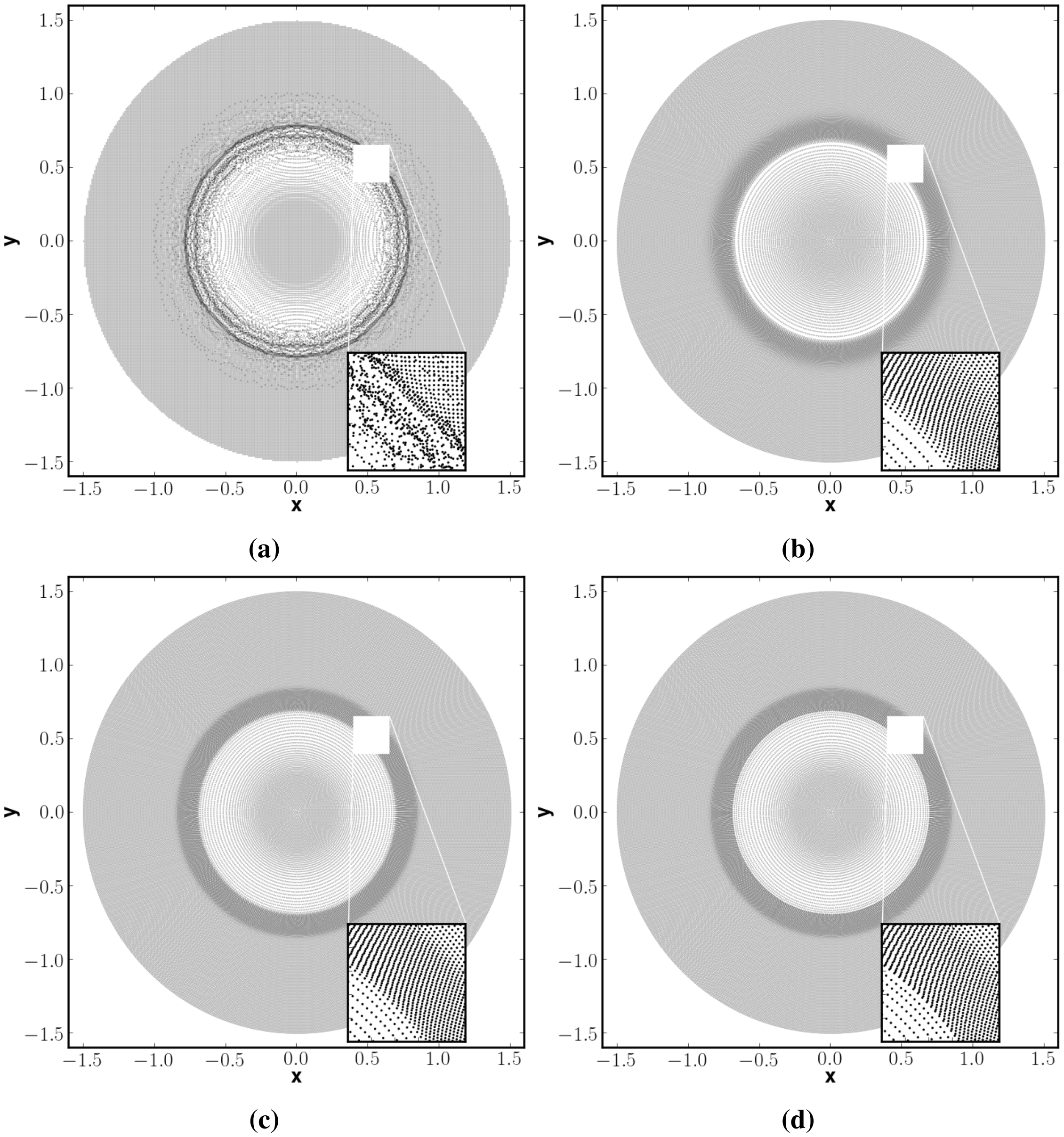

Figure 2.12: *Two dimensional particle positions for the blast wave problem EP1 at the final time* $t = 0.2s$*. Standard SPH (2.12a)* $\sigma = 2$*, V-B-SPH (2.12b)* $\sigma = 2$*, MWSPH with Rusanov flux (2.12c) and MWSPH with Osher flux (2.12d) with polynomial degree* $M = 3$*,* $\sigma = 2$ *and* $\sigma_{mls} = 4$*).*

Blast wave problem EP2 In the following, a second blast wave problem is solved, with initial data given in Table 2.3. Here, the density is initially constant. Fig. 2.13 shows the comparison between the reference solution, V-B-SPH and MWSPH with both Rusanov and Osher-type fluxes and also in this case the new MWSPH scheme yields a better accuracy than the V-B-SPH. For this blast wave problem EP2 we also study the effect of initial particle disorder on the quality of the numerical results. For this purpose, a second simulation is carried out where the particles are initially located at the barycenters of an unstructured triangular mesh. This allows the correct computation of the initial particle volumes V_i needed by the scheme. The mesh has been generated with the PDE toolbox of MATLAB and is depicted in Fig. 2.14. The computational results obtained with the Rusanov flux and the Osher-type flux are depicted in Fig. 2.15, where in both cases a good agreement with the reference solution can be observed.

(*This page has been intentionally left blank*)

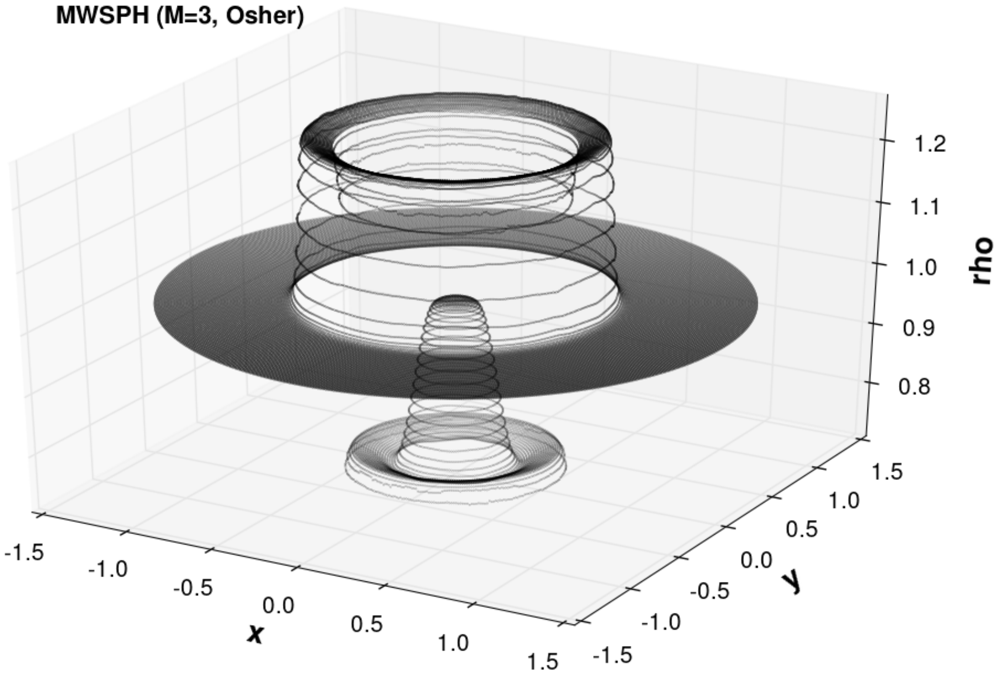

MWSPH (M=3, Osher)

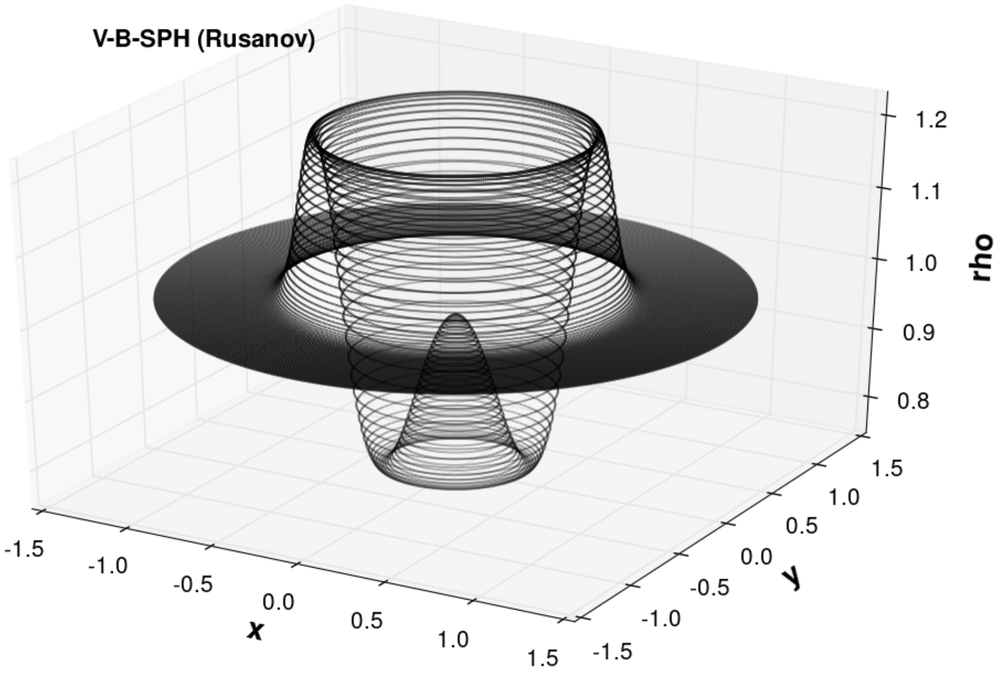

V-B-SPH (Rusanov)

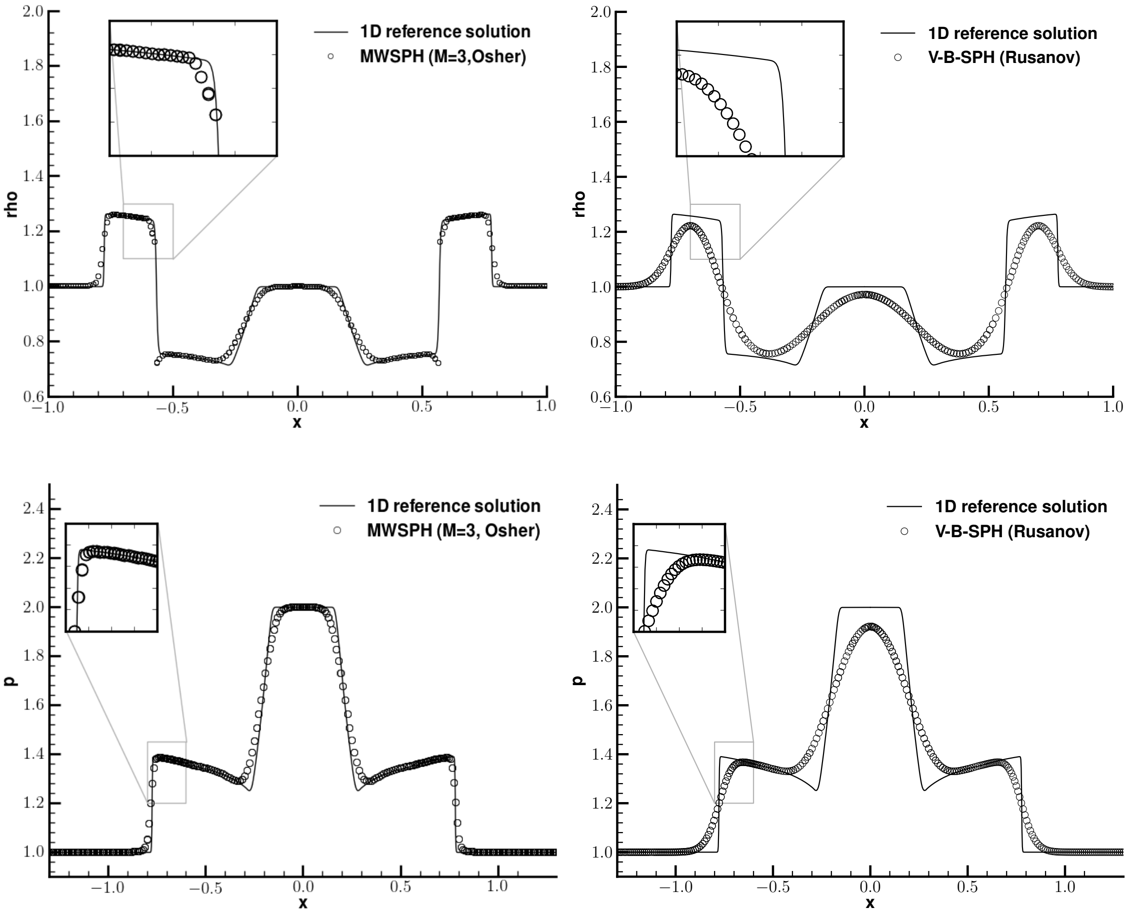

Figure 2.13: *Two dimensional numerical results of the blast wave problem EP2 with initial data given by Table 2.3 computed with V-B-SPH (Rusanov,* $\sigma = 2$*) and MWSPH (Osher flux,* $\sigma = 2$*,* $\sigma_{mls} = 4$*, M=3) at time* $t = 0.2s$*. Two dimensional pressure profile for V-B-SPH (Rusanov) and MWSPH (Osher) the top. Cut at* $y = 0$ *compared with 1D reference solution (continuous line) for pressure and density.*

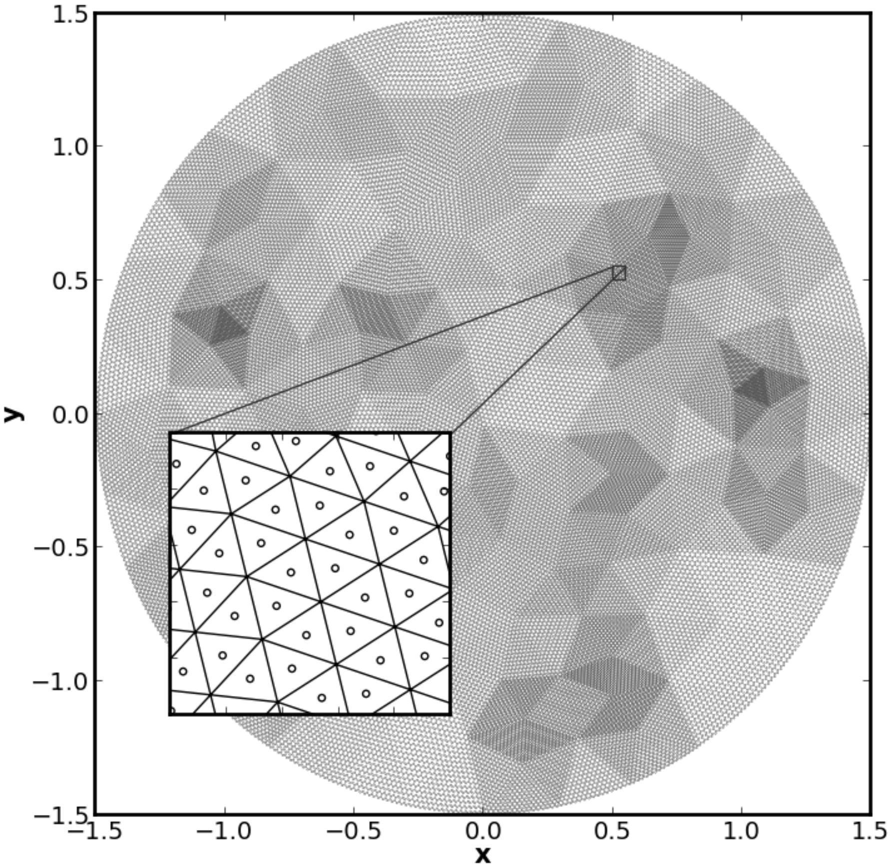

Figure 2.14: *Unstructured triangular mesh used for the assessment of initial particle disorder in the case of blast wave problem EP2.*

(*This page has been intentionally left blank*)

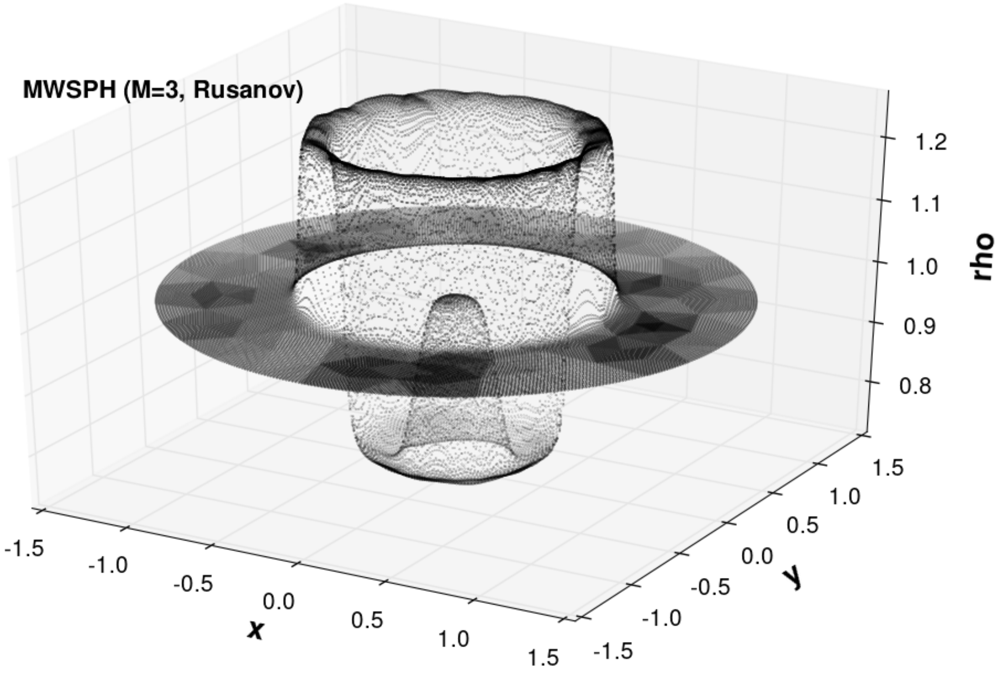
MWSPH (M=3, Rusanov)
rho
1.2
1.1
1.0
0.9
0.8
x
-1.5
-1.0
-0.5
0.0
0.5
1.0
1.5
y
1.5
1.0
0.5
0.0
-0.5
-1.0
-1.5

(a)

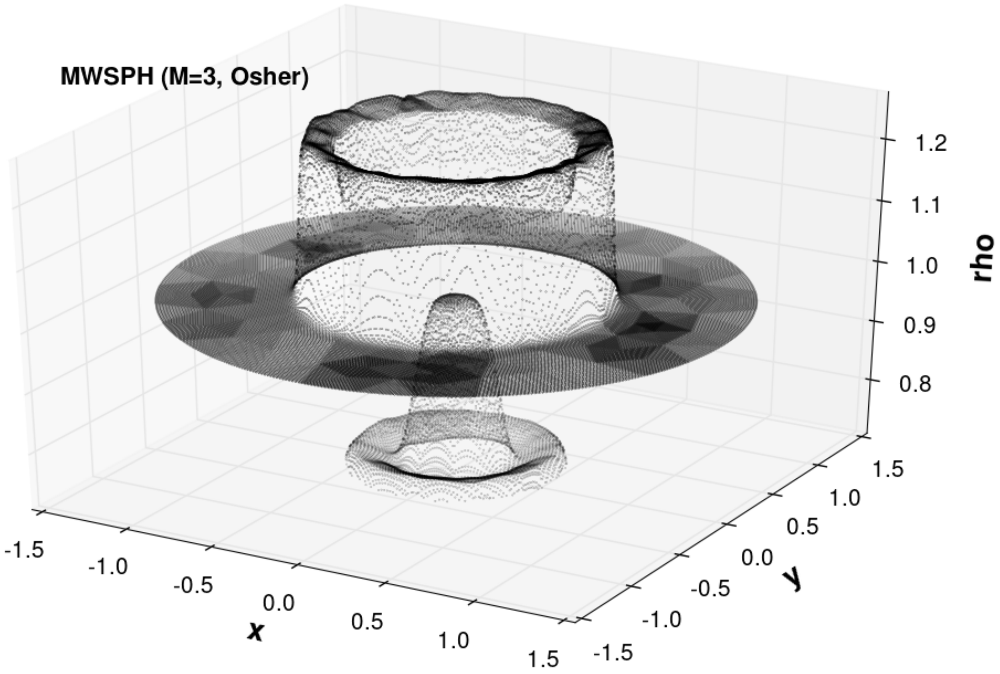
MWSPH (M=3, Osher)
rho
1.2
1.1
1.0
0.9
0.8
x
-1.5
-1.0
-0.5
0.0
0.5
1.0
1.5
y
1.5
1.0
0.5
0.0
-0.5
-1.0
-1.5

(b)

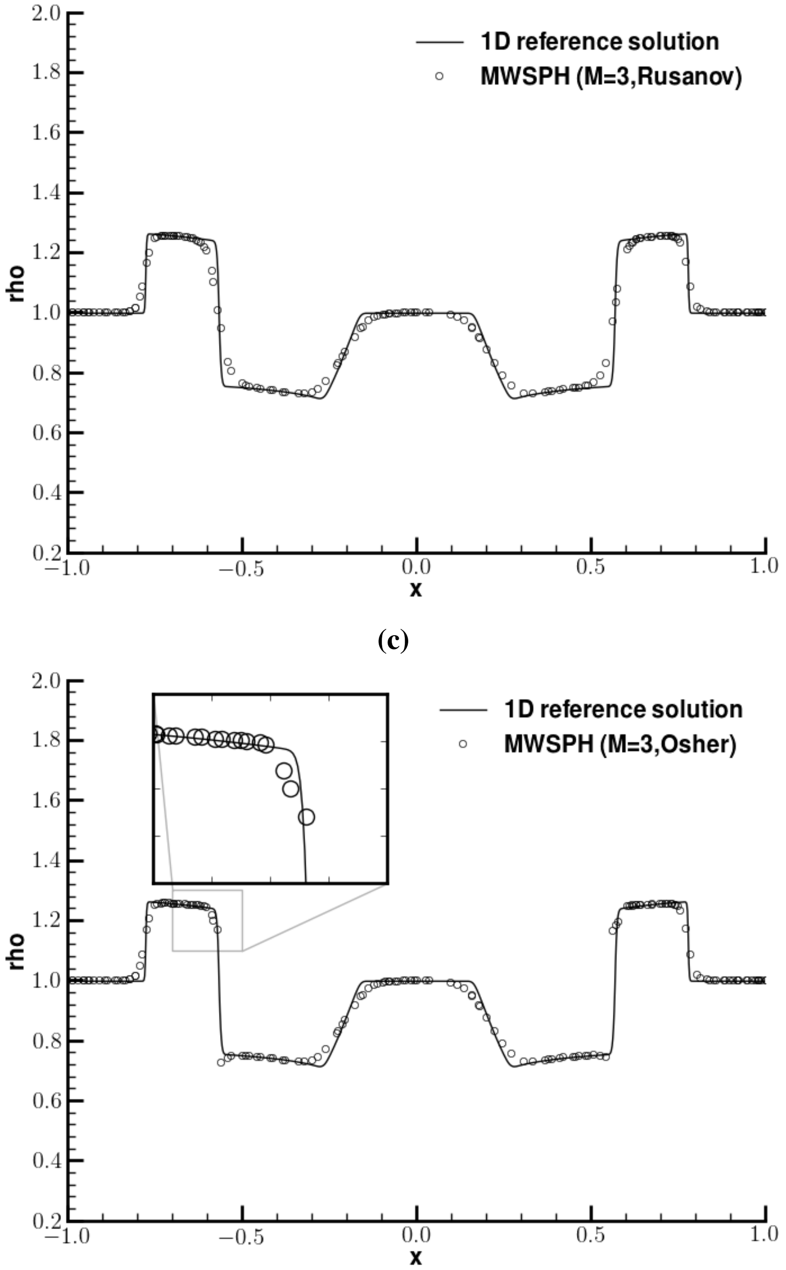

(c)

(d)

Figure 2.15: *Numerical results for the blast wave problem EP2 with initial particles distributed on an unstructured triangular grid. Rusanov-type flux* ***(a)***, ***(c)***. *Osher-type flux* ***(b)***, ***(d)***.

CPU time per particle and time step The present MWSPH scheme has been implemented in FORTRAN 90, but the computer code has not been optimized. For the simulations presented in this work, the method needed about 10^{-2} s of CPU time per particle and time step using a fourth order MLS-WENO reconstruction with $M = 3$ and the Rusanov flux on an Intel(R) Core(TM) i7-2640M CPU with 2.80GHz and 8 GB of RAM. For comparison, an optimized fourth order ($M = 3$) ADER-WENO finite volume scheme *Dumbser et al.* [2007, 2008a] on an unstructured triangular mesh with characteristic WENO reconstruction and Osher-type flux *Dumbser and Toro* [2011b] needs about 10^{-4} s per element and time step. To improve the computational efficiency of our MWSPH scheme, we therefore intend to use a more efficient ADER-type one-step time integration *Titarev and Toro* [2005]; *Dumbser et al.* [2007, 2008b,a] in the near future, since this would require only one MLS-WENO reconstruction and associated neighbor search per time step, instead of one for each Runge-Kutta substage, as in the current implementation of our MWSPH scheme.

2.4.3 1D Sod shock tube problem

For the sake of completeness, Fig (2.16) shows the density and pressure profiles computed with MWSPH using the Osher-type and the Rusanov flux for a purely one-dimensional test case. In 1D only three stencils are used: one centered stencil, and two one-sided stencils. The domain $[0;1]$ is discretized using 200 initially equidistant particles. The initial condition is given by

$$(\rho, u, p)(x, 0) = \begin{cases} (\rho_{in}, 0, p_{in}), & \text{if } x \leq 0.5, \\ (\rho_{out}, 0, p_{out}), & \text{otherwise,} \end{cases} \tag{2.44}$$

where the inner and outer states denoted by the subscripts *in* and *out* are the same as for the 2D test case shown in Table 2.2. In the 1D case we consider a second degree reconstruction polynomial ($M = 2$), a smoothing length defined by $\sigma = 2$ and a MLS stencil width defined by $\sigma_{mls} = 4$. We can note an excellent agreement with the exact solution given by the algorithm detailed in *Toro* [1997]. In particular when using the Osher-type flux, we can note a very sharp resolution of the contact discontinuity. We further observe that our scheme does not produce any spurious pressure oscillations at the contact wave, in contrast to standard SPH.

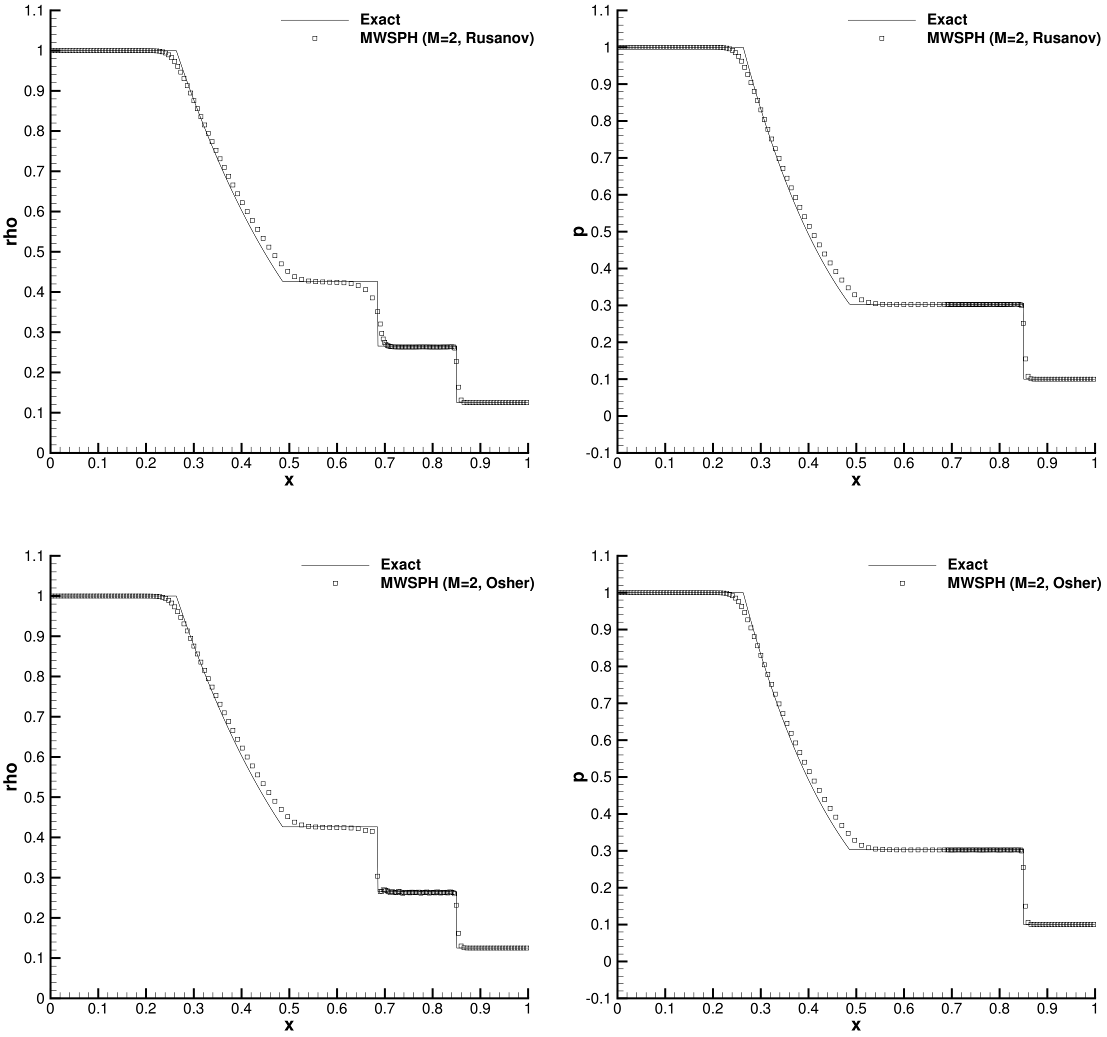

Figure 2.16: *Numerical results for 1D Sod's problem compared with exact solution at the time t = 0.2s computed with 1D MWSPH: Rusanov flux on the top and Osher flux on the bottom. Polynomial degree* $M = 2$, $\sigma = 2$.

2.5 Conclusions

In this chapter we have presented a new SPH formulation based on a novel piecewise high order moving-least-squares WENO reconstruction and on the use of Riemann solvers. To our knowledge, this is the first time that an SPH scheme uses a piecewise high order meshfree WENO reconstruction on moving point clouds in multiple space dimensions. The MLS-WENO method is based on a nonlinear weighted Moving-Least-Squares interpolation on a set of different stencils and produces essentially non-oscillatory polynomial reconstructions. We have shown numerical evidence that the new meshfree MLS-WENO approach can produce higher order reconstruction polynomials that are accurate for smooth problems and essentially non oscillatory for problems with discontinuities.

As the SPH method of Vila and Ben Moussa our new MWSPH formulation uses Riemann solvers to avoid the use of artificial viscosity, but the new higher order WENO reconstruction results in improved accuracy and less numerical dissipation compared to the SPH scheme of Vila and Ben Moussa.

We have presented numerical results for two dimensional blast wave problems and for a one-dimensional shock tube problem. The results indicate that MWSPH increases the accuracy compared to the standard SPH scheme with artificial viscosity. Unlike standard SPH it does not produce unphysical oscillations in the pressure and density fields. We observed that MWSPH can handle properly both rarefaction and shock waves producing essentially non oscillatory profiles at discontinuities. Significant improvements in the resolution of contact waves can be achieved when using the Osher-type flux instead of the Rusanov flux.

Future work will include a thorough code optimization together with a parallel implementation, as well as numerical simulations of advection-diffusion equations with stiff source terms. Following *Aboiyar et al.* [2010] further research could also concern the use of kernel-based polyharmonic spline reconstructions instead of the moving-least-squares (MLS) method in order to further increase accuracy and flexibility. In order to reduce the cost of the MLS-WENO reconstruction and the associated neighbor search, we plan to implement an ADER-type one-step time integration *Titarev and Toro* [2005]; *Dumbser et al.* [2007, 2008b,a] in the near future, since in this manner the expensive reconstruction step will be carried out only once per time step and not in each Runge-Kutta substage again.

3 MWSPH schemes for Advection Diffusion transport in porous media

Smooth Particle Hydrodynamics (SPH) is a Lagrangian meshless numerical scheme developed by *Lucy* [1977] and *Gingold and Monaghan* [1977] and originally applied to advection dynamics, see for examples [*Monaghan*, 1994, 2005; *Ferrari et al.*, 2009] and then extended to advection diffusion equations (see [*Brookshaw*, 1985; *Cleary and Monaghan*, 1999; *Español and Revenga*, 2003; *Aristodemo et al.*, 2010]). SPH has been applied by *Zhu and Fox* [2001, 2002] to simulate diffusion in a periodic porous media and *Tartakovsky et al.* [2007] used the SPH to study reactive solute transport in homogeneous porous media. Recently *Herrera* [2009]; *Herrera et al.* [2010]; *Herrera and Beckie* [2012]; *Boso et al.* [2013] extended SPH to solute transport in heterogeneous porous media.

SPH offers several advantages with respect to traditional Eulerian and Lagrangian numerical schemes. First, it does not suffer from grid orientation effects, which is one of the main problems of the standard Eulerian schemes [*Herrera et al.*, 2010] and it ensures accuracy by introducing little numerical diffusion [*Herrera et al.*, 2009, 2010; *Boso et al.*, 2013]. Unlike particle tracking based methods SPH is able to track low concentrations [*Tompson*, 1993; *Obi and Blunt*, 2004; *Herrera et al.*, 2010] and does not require a background grid to simulate chemical reactions [*Herrera et al.*, 2010]. SPH, however, has also some limitations. A relevant limitation is the occurrence of both unphysical oscillations and negative concentrations when the diffusion is anisotropic [*Herrera*, 2009; *Herrera et al.*, 2010; *Herrera and Beckie*, 2012]. In an attempt to alleviate this problem *Herrera et al.* [2010] developed a new hybrid numerical scheme which applies SPH in a streamline oriented framework. In this scheme, anisotropic dispersion is split into an anisotropic component with only the component along the streamline different from zero and an isotropic component. The one-dimensional advection diffusion equation resulting from the first component is solved by using a finite difference scheme, while the second component is solved by SPH. A modification of this scheme has been proposed by *Boso et al.* [2013], which takes into account that the volume associated to the points where SPH is applied changes along the streamlines. With this modification the method is similar, in term of accuracy, to the standard SPH, but much less demanding in term of computational time.

The objective of the present work is to extend a new class of SPH, the MWSPH [*Avesani et al.*, 2014], originally applied to gas dynamics to advection diffusion equation overcoming the difficulties of existing SPH based schemes in simulating anisotropic dispersion porous media. This new class of SPH, uses high order accurate nonlinear WENO reconstruction operator into SPH, which is usually applied in the context of mesh based finite volume schemes. This yields a nonlinear scheme for the evaluation of the diffusive mass transfer between interacting particles.

The main contribution of this work are: i) the extension of MWSPH to diffusion and anisotropic dispersion problems, ii) the use and the comparison of different schemes for diffusive flux reconstructions, iii) the study of positivity preserving properties and accuracy of the proposed scheme and iv) the comparison of the new scheme with the traditional SPH for advection-diffusion equation.

The outline of this paper is organized as follows. In Section 3.1 we introduce the mathematical model for advection-diffusion equation in the Lagrangian formulation and we describe the new formulation of SPH for diffusion equation. In Section 3.2 we briefly describe the Moving-Least-Square Weno reconstruction. Hence in Section 3.3 we compare mesh-free WENO reconstruction with standard SPH for diffusive fluxes. In Section 3.4 we test the new scheme for both homogeneous and heterogeneous cases comparing with standard SPH. Finally Section 4.5 discusses the advantages of the scheme simulating passive solute transport in porous media.

3.1 Smooth Particle Hydrodynamics

We focus on the advection-diffusion equation, which is commonly used to model solute transport in porous media. Written in a Lagrangian formulation it reads as:

$$\frac{d\mathbf{r}(t)}{dt} = \mathbf{v}(\mathbf{r}(t),t) \tag{3.1}$$

$$\frac{dC(t,\mathbf{r})}{dt} = \nabla \cdot (\mathbf{D}(t,\mathbf{r})\nabla C(t,\mathbf{r})) \tag{3.2}$$

where Eqns. (3.1) and (3.2) describe the movement of the fluid and the change of concentration due to hydrodynamic dispersion, respectively. The variables are the position $\mathbf{r}$, the given fluid velocity $\mathbf{v}$, the coefficient of hydrodynamic dispersion $\mathbf{D}(t,\mathbf{r})$, the concentration C and simulation time t. For the sake of simplicity, hereafter we omit the time and space dependence indication in $\mathbf{r}$,$\mathbf{v}$, $\mathbf{C}$ and $\mathbf{D}$. According to *Bear* [1972] hydrodynamic dispersion in a isotropic porous media can be modeled as:

$$\mathbf{D}_{\hat{i}\hat{j}} = (\alpha_T|\mathbf{v}| + D_m)\delta_{\hat{i}\hat{j}} + (\alpha_L - \alpha_T)\frac{v_{\hat{i}}v_{\hat{j}}}{|\mathbf{v}|} \tag{3.3}$$

where D_m is the molecular diffusion coefficient, $\hat{i}$ and $\hat{j}$ are the main direction vectors, α_L and α_T are the longitudinal and transverse dispersivities. In all SPH based schemes the system of contiuum differential Eqns. (3.1 and 3.2) is approximated in a finite number of points (particles), which carry the physical property of interest, in our case the solute concentration, and which move with the fluid according to Eqn. (3.1) (see for examples [*Monaghan*, 2005; *Ferrari et al.*, 2009; *Herrera et al.*, 2009]). Notice that the solution of Eqn. (3.1), which provides the position of the *i-th* particle, is solved by a standard particle tracking scheme (e.g. [*Salamon et al.*, 2006; *Srinivasan et al.*, 2010]), so that the SPH formulation is only used to approximate the diffusive term (3.2).

3.1.1 Monaghan's formulation

Herrera and Beckie [2012] and *Español and Revenga* [2003] derived the following SPH approximation for anisotropic diffusion, which is based on the SPH formulation developed by Monaghan for modelling thermal diffusion [*Brookshaw*, 1985; *Cleary and*

Monaghan, 1999; *Monaghan*, 2005]:

$$\frac{dC_i}{dt} = \frac{1}{2}\sum_j^N \frac{m_j}{\rho_{ij}}(C_i - C_j)\nabla_i W_{ij}\mathcal{D}(r_i, r_j) \tag{3.4}$$

where

$$\mathcal{D}(r_i, r_j) = \sum_{\hat{i}=1}^{\nu}\sum_{\hat{j}=1}^{\nu}\left(D^i_{\hat{i}\hat{j}} + D^j_{\hat{i}\hat{j}}\right)\left[4\frac{(r_j - r_i)_{\hat{i}}(r_j - r_i)_{\hat{j}}}{|r_j - r_i|^2}\right] - \delta_{\hat{i}\hat{j}} \tag{3.5}$$

Furthermore, $\nabla_i W_{ij}$ is the gradient of the interpolating kernel function centered in r_i [*Ferrari et al.*, 2009]. Here, ν denotes the number of space dimensions, i.e. $\nu = 2$ for the two-dimensional simulations and ρ_{ij} can be approximated as the arithmetic average of the particle density between particles i and j, which ensures that the diffusive fluxes are antisymmetric [*Herrera et al.*, 2009]. Among available options we use the cubic B-kernel interpolating kernel functions:

$$W_{ij} = \frac{c}{(h_{ij})^{\nu}}\begin{cases} 2/3 - q_{ij}^2 + q_{ij}^3/2 & \text{if } 0 \le q_{ij} < 1 \\ (2 - q_{ij})^3/6 & \text{if } 1 \le q_{ij} < 2 \\ 0 & \text{if } q_{ij} \ge 2 \end{cases} \tag{3.6}$$

where q_{ij} is the relative distance between particles *i-th* and *j-th* defined as $\mathbf{q}_{ij} = \mathbf{r}_i - \mathbf{r}_j|/h_{ij}$ and c is a normalization constant. [*Ferrari et al.*, 2009; *Monaghan*, 2005]. Here the term h_{ij} is the smoothing length and it determines the size of the kernel support for each particle.

3.1.2 The MWSPH formulation of advection-diffusion equation

Starting from the the new class of MWSPH schemes developed by *Avesani et al.* [2014] we propose to use Riemann solvers to estimate the diffusive fluxes between two interacting particles i and j. Following MWSPH schemes the advection-diffusion equation reads as follows:

$$\frac{dV_i}{dt} = \sum_{j=1}^{N} 2V_iV_j(2\mathbf{v}_{ij} - \mathbf{v}_i)\cdot\nabla W_{ij}, \tag{3.7}$$

$$\frac{dC_i}{dt} = -\sum_{j=1}^{N} 2V_iV_j\mathbf{G}_{ij}\cdot\nabla W_{ij}, \tag{3.8}$$

where $\mathbf{G}_{ji}$ is the flux tensor and V_j is the volume of the particle j, which evolves in time according evolves according to the velocity field provided by Eqn. (3.7). The numerical approximation of the flux tensor $\mathbf{G}_{ji}$ depends on the choice of the Riemann solver. Using for example the Rusanov-type flux, one obtains [*Dumbser and Balsara*, 2009; *Dumbser*, 2010a; *Hidalgo and Dumbser*, 2011]:

$$\mathbf{G}_{ij} = \frac{1}{2}\left(\mathbf{F}(\nabla C_i^-) + \mathbf{F}(\nabla C_j^+)\right) - \Theta(C_j^- - C_i^+) \otimes \vec{n}_{ij}, \tag{3.9}$$

where Θ is the maximum of Jacobian of the flux with respect to the gradient of C [*Gassner et al.*, 2007; *Hidalgo and Dumbser*, 2011], $\vec{n}_{ij}$ is the unitary separation vector between particles i and j; and $\mathbf{F}$ is the non-linear flux vector, which depends on the concentration and on the concentration gradient. The terms $C_i^- = C_i(\bar{r}_{ij})$, $C_j^+ = C_j(\bar{r}_{ij})$, $\nabla C_i^- = \nabla C_i(\bar{r}_{ij})$ and $\nabla C_j^+ = \nabla C_j(\bar{r}_{ij})$ are the concentrations and concentration gradients computed at the midpoint $\bar{\mathbf{r}}_{ij} = 1/2(\mathbf{r}_i + r_j)$ using local high order accurate reconstruction at each particle's position $\mathbf{r}_i$ known the concentration values of particles in their surrounding. As summarized in Fig. 3.1.2 we first define local high order reconstruction polynomials $C_i(x,y)$ and $C_j(x,y)$ for each couple of interacting particles $\mathcal{P}_j$ and $\mathcal{P}_j$. We use the reconstruction polynomials to compute the concentration and the concentration gradient at the midpoint of the two interacting particles $\mathcal{P}_i$ and $\mathcal{P}_j$ (Fig. 3.1.2). For sake of clearness the fluxes $\mathbf{G}_{ij}$ between two interacting particles in Eqn. (3.8) can be defined as:

$$\mathbf{G}_{ij} = \frac{1}{2}(\mathbf{D}_i \nabla C_i^+ + \mathbf{D}_j \nabla C_j^-) - \Theta_{ij}(C_j^+ - C_i^-) \otimes \vec{n}_{ij}, \tag{3.10}$$

with $\mathbf{D}$ the diffusion tensor also evaluated at particle interfaces. The term $\mathbf{v}_{ij}$ is the velocity at interface between the two interacting particles $\mathcal{P}_i$ and $\mathcal{P}_j$.

3.2 Moving-Least-Square and WENO fluxes reconstruction

For details of the meshfree Moving-Least-Square and WENO reconstruction we refer the reader to [*Avesani et al.*, 2014] and we only briefly recall the main points here. First,

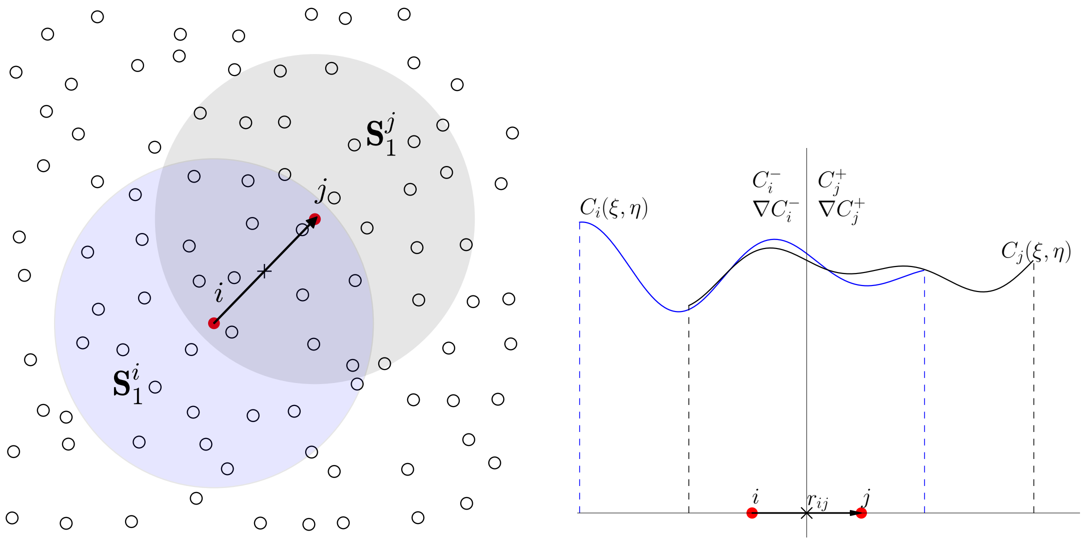

(a) **(b)**

Figure 3.1: *Particle central stencils and recontructions polynomials.*

we construct a set of reconstruction stencils for each particle $\mathcal{P}_i$ as follows:

$$\mathcal{S}_s^i = \bigcup_{k}^{ne_s} \mathcal{P}_{j(k)}, \tag{3.11}$$

where k with $1 \leq k \leq ne_s$ is a local index, counting the particles $\mathcal{P}_j$ in each stencil, $j = j(k)$ is the mapping from the local index k to the global indexation of the particles in the computational domain Ω, ne_s is the number of particles in each stencil and n_s is the number of stencils. The set of stencils consists of one central stencil $\mathcal{S}_0^i$ and a set of one-sided stencils ($1 \leq s \leq 8$). The first stencil, i.e. the central stencil, is obtained by the union of the central particle $\mathcal{P}_i$ and its surrounding particles $\mathcal{P}_j$ as

$$\mathcal{S}_0^i = \bigcup_{k}^{ne_s} \mathcal{P}_{j(k)}, \qquad \left\|\mathbf{r}_{ij}\right\| \leq h, \tag{3.12}$$

while the one-sided stencils are defined as :

$$\mathcal{S}_s^i = \bigcup_{k}^{ne_s} \mathcal{P}_{j(k)}, \quad \left\|\mathbf{r}_{ij}\right\| \leq 2h \quad \text{and} \quad \theta \in [(s-1)\pi/4, s\pi/4], \tag{3.13}$$

where $h_{i,mls}$ is a characteristic length and θ is the angle formed by the vector $\mathbf{r}_{ij} = \mathbf{r}_j - \mathbf{r}_i$ connecting the two particles $\mathcal{P}_i$ and $\mathcal{P}_j$ and the x-axis,

$$\tan(\theta) = \frac{y_j - y_i}{x_j - x_i}. \tag{3.14}$$

As the smoothing length in the kernel interpolation $h_{i,mls}$ is locally variables:

$$h_{i,mls} = \sigma_{mls}\sqrt{m_i/\rho_i} \tag{3.15}$$

with σ_{mls} suitable constant.

After these preparatory steps, we apply a Moving-Least-Square scheme. In particular, for each particle we consider nine reconstruction polynomials:

$$C_i^s(\xi,\eta) = C_i + \sum_{m=1}^{nc-1} \widehat{w}_{m,s}\phi_m(\xi,\eta), \tag{3.16}$$

one for each of its nine stencils $\mathcal{S}_s^{p_i}$, where ξ and η are reference coordinates in a 2D coordinate system defined as $\xi = (x - x_i)/h$ and $\eta = (y - y_i)/h$ where x_i and y_i denote coordinates of particle positions in the two dimensional coordinates system, $\widehat{w}_{m,s}$ denotes the set of nc undetermined coefficients of the s-th polynomial and ϕ_m are the associated basis functions. Eqn. (3.16) is a Taylor series expansion of arbitrary order M of the concentration around the position of the particle p_i. In Eqn. (3.16) the index m ranges from 1 to its maximum nc that depends on the number of space dimensions. In two dimensional domain nc is given by

$$nc = \frac{(M+2)(M+1)}{2}. \tag{3.17}$$

Finally, the nc basis functions in Eqn. (3.16) are defined as follows:

$$\phi_m(\xi,\eta) = \frac{\xi^a\eta^b}{h^{(a+b)}} \tag{3.18}$$

where $a + b = l$ and l ranges from 1 to M [*Zwillinger*, 2003] [*Agossler Albert*, 2001]. The smoothing length h used in Eqn. (3.18) ensures that for small particles distances the basis function values do not approach the computer's floating precision [*Agossler Albert*, 2001] and to avoid ill-conditioned reconstruction matrices. The unknown coefficients $\widehat{w}_{m,s}$ are computed applying a set of reconstruction equations on each stencil S_s as follows:

$$C_j - C_i = \sum_{j=1}^{ne_s} \left(\sum_{m=1}^{nc-1} \widehat{w}_{m,s} \phi_m (\mathbf{r}_j - \mathbf{r}_i) \right) \tag{3.19}$$

where ne_s is the number of particles in stencil S_s, which are chosen in such a way that the number of equations in the system (3.19) is larger than the number of degrees nc. Therefore, Eqns. (3.19) constitute an overdetermined linear algebraic system for the coefficients, which is solved using a least square technique [*Agossler Albert*, 2001; *Dumbser et al.*, 2008a,b]. In order to ensure linear stability, we suggest to use at least $2nc$ particles in each stencil for linear stability purposes [*Dumbser and Kaëser*, 2007; *Dumbser et al.*, 2007].

The final non-linear WENO reconstruction polynomial $C_{i,WENO}(\xi, \eta)$ of degree M is obtained by a non-linear combination of the nine polynomials C_i^s of degree M reconstructed on the ns stencils:

$$C_{i,WENO}(\xi, \eta) = \sum_{l=1}^{ns} \omega_l C_i^s \tag{3.20}$$

with the normalized nonlinear weights

$$\omega_l = \frac{\widetilde{\omega}_l}{\sum_{r=1}^{ns} \widetilde{\omega}_r}. \tag{3.21}$$

computed from the non-normalized weights $\widetilde{\omega}_l$ [*Dumbser et al.*, 2008a,b] as

$$\widetilde{\omega}_l = \frac{\lambda_r}{(\varepsilon + \sigma_s)^r} \tag{3.22}$$

where $\varepsilon = 10^{-14}$, $r = 4$ and the linear weights are set $\lambda_1 = 10^5$ for central stencil and $\lambda_l = 1$ for one side stencil ($2 \leq l \leq 9$). Finally, due to the complexity of mesh-free methods space, we propose to compute the smoothness indicator in a mesh-independent manner as:

$$\sigma_l = \sum_{r=1}^{M} \sum_{\alpha=0}^{r} \sum_{\beta=0}^{r-\alpha} \left(\frac{\partial^r}{\partial^\alpha \xi \partial^\beta \eta} C_i^l \right)^2 \tag{3.23}$$

where the integration of the derivatives in the central cell is implicitly taken into account. Once defined the WENO reconstruction polynomial, the gradient reconstruction polynomial is directly computed from the derivatives of the basis functions as follows:

$$\begin{aligned}\nabla C_{i,WENO}(\xi,\eta) &= \sum_{m=1}^{nc} \widehat{\omega}_m \frac{\partial \phi_m}{\partial \xi},\\ &= \sum_{m=1}^{nc} \widehat{\omega}_m \frac{\partial \phi_m}{\partial \eta}.\end{aligned} \tag{3.24}$$

3.3 Gradient reconstruction

A key point of the MWSPH is the concentration and concentration gradient reconstruction at particle interfaces. The aim of this section is therefore to analyze the accuracy of Moving-Least-Square WENO scheme in gradient computation. Notice that we take into account only reconstruction, this means that we focus only on WENO combined with Moving-Least-Square, here referred as MLS-WENO, and not on the all MWSPH scheme. We compare the new MLS-WENO with the standard SPH which is often used for gradient reconstruction [*Liu and Liu*, 2010; *Di Blasi et al.*, 2011]. According to [*Li and Liu*, 2004] we use the following expression to compute concentration gradient with standard SPH to reach at least zero-th order consistency:

$$\frac{\nabla C_i}{\rho_i} = \sum_{j=1}^{N} \left(\frac{C_j}{\rho_j^2} + \frac{C_i}{\rho_i^2} \right) \nabla W_{ij} m_j. \tag{3.25}$$

We illustrate the capabilities of our method by considering both equispaced particles and not-equispaced particles. The latter case is obtained by perturbing the initial position of the particles, at the nodes of a grid with spacing $dx = dy$, with pseudo-random numbers from the uniform distribution within the range $[0,1)$. We considerer not equispaced particles for mainly two reason. Firstly in a real application the initial concentration informations could be irregularly distributed. Secondly in a heterogeneous flow field, as particles move carried by the flow irregularly velocity, we have the distortion of regular initial positions [*Herrera and Beckie*, 2012].

In the test case, we assign an initial concentration to each particle, and then we compute the gradient by using both standard SPH and MLS-WENO methods. In order to perform accuracy and convergence analyses we compute the L_p norms according to:

$$L_p = \left(\sum_{j=1}^{N} |C_i - C_e(x_i, y_i)| \right)^{(1/p)} /N \tag{3.26}$$

where $C_e(x_i, y_i)$ is the analytical solution at (x_i, y_i), the position of the $i-th$ particle. The L_∞ norm is approximated by taking the maximum error among the particles.

3.3.1 Smooth case

The first test case consists in the computation of the gradient of a two-dimensional bell shape function with the maximum $C(0,0) = 1$ at $(x,y) = (0,0)$ and variance $\sigma_2 = 0.2$. The computational domain is a square with the lower left corner at $(x,y) = (-1,-1)$ and the upper right corner at $(x,y) = (1,1)$. Sub-Fig. 3.2a and Sub-Fig. 3.2c show the gradient computed by using equispaced particles, while Sub-Fig. 3.2b and Sub-Fig. 3.2d show the gradient computed by using irregularly distributed particles. In both cases our MLS-WENO scheme produces excellent approximations of the gradient, while in case of equispaced particles the standard's SPH scheme underestimates the gradient. Moreover, for not equispaced test case, the standard SPH shows strong oscillations around the exact value. This is consistent with the findings of *Liu and Liu* [2006]. Table 3.5 and Table 3.2 show the errors and the orders of convergence measured for equispaced and non-equispaced particles where h_{mls} is the central stencil radius and dx is the particle mean distance. We remark that MLS-WENO reconstruction reaches the nominal order of accuracy M regardless of the distribution of the particles within the stencil, which can be highly inhomogeneous without impacting negatively the gradient. The only imposed condition is that every stencil has at least $2M$ number of particles. Finally for sake of completeness we report in Table 3.3 the convergence rate of standard SPH in gradient reconstruction: in case of equispaced particles the error is $O(h^2)$, while in case of not-equispaced particles the behavior of the scheme is totally unpredictable with even negative convergence rate in some cases. Negative convergence rate has been already reported for anisotropic dispersion application in *Herrera and Beckie* [2012].

dx	ε_{L_1}	ε_{L_2}	ε_{L_2}	$O(L_1)$	$O(L_2)$	$O(L_\infty)$	$t_{CPU}(s)$
$MLS-WENO\ M=3\ (\sigma_{mls}=2.5)$							
0.40E-01	0.25E-03	0.13E-02	0.25E-01	-	-	-	0.38
0.20E-01	0.21E-04	0.14E-03	0.31E-02	3.62	3.29	2.98	1.76
0.10E-01	0.16E-05	0.14E-04	0.47E-03	3.69	3.26	2.73	7.54
0.50E-02	0.48E-06	0.27E-05	0.62E-04	1.72	2.39	2.92	33.52
0.25E-02	0.67E-07	0.34E-06	0.78E-05	2.84	2.99	3.00	137.30
$MLS-WENO\ M=4\ (\sigma_{mls}=2.5)$							
0.40E-01	0.16E-03	0.93E-03	0.13E-01	-	-	-	0.73
0.20E-01	0.11E-04	0.61E-04	0.89E-03	3.92	3.92	3.89	3.39
0.10E-01	0.68E-06	0.39E-05	0.57E-04	3.97	3.98	3.98	17.86
0.50E-02	0.43E-07	0.24E-06	0.36E-05	3.99	3.99	3.99	73.53
0.25E-02	0.27E-08	0.15E-07	0.22E-06	4.00	4.00	4.00	316.68
$MLS-WENO\ M=5\ (\sigma_{mls}=3.0)$							
0.40E-01	0.28E-04	0.12E-03	0.19E-02	-	-	-	1.58
0.20E-01	0.66E-06	0.31E-05	0.53E-04	5.42	5.29	5.15	8.29
0.10E-01	0.25E-07	0.11E-06	0.17E-05	4.70	4.86	4.93	38.73
0.50E-02	0.70E-09	0.31E-08	0.54E-07	5.18	5.11	5.00	165.39
0.25E-02	0.24E-10	0.11E-09	0.17E-08	4.85	4.89	5.00	697.02

Table 3.1: *Numerical convergence results for Gaussian gradient reconstruction with second, third and fourth order version of the MLS-WENO scheme. In the first row the particles distance dx. The second, third and fourth columns contain the error measured in L_1, L_2 and L_∞ norms, followed by three columns giving the measured order of accuracy between the respective particles and the previous particles distributions. The last row gives the CPU time needed by the serial code on Intel(R) Core(TM) i7-2640M CPU 2.80GHz with 8 GB of RAM. The error norms refer to the concentration considering equispaced particles for the smooth case.*

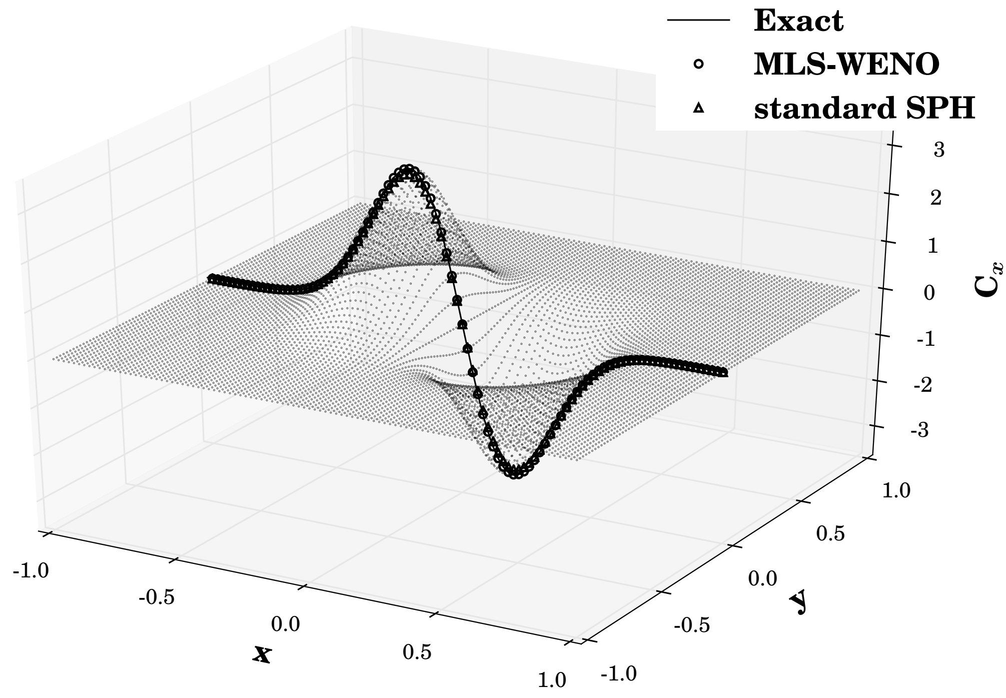
Exact
MLS-WENO
standard SPH
3
2
1
0
-1
-2
-3
$\mathbf{C}_x$
1.0
0.5
0.0
-0.5
-1.0
$\boldsymbol{y}$
-1.0
-0.5
0.0
0.5
1.0
$\boldsymbol{x}$

(a)

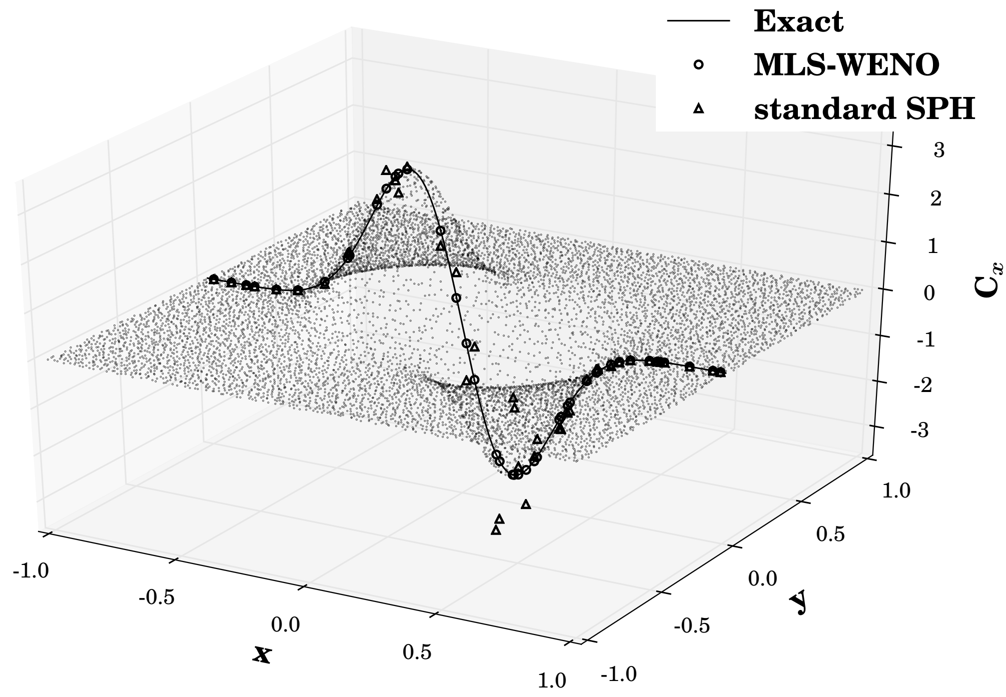
Exact
MLS-WENO
standard SPH
3
2
1
0
-1
-2
-3
$\mathbf{C}_x$
1.0
0.5
0.0
-0.5
-1.0
$\boldsymbol{y}$
-1.0
-0.5
0.0
0.5
1.0
$\boldsymbol{x}$

(b)

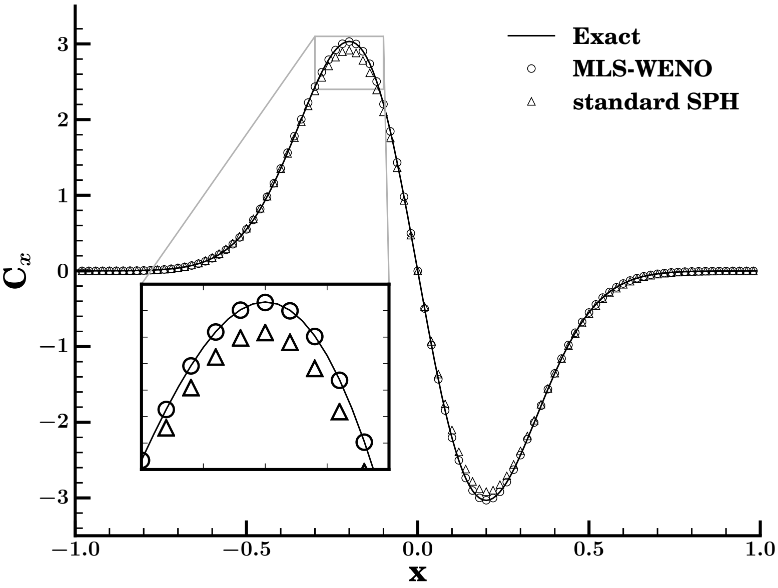

(c)

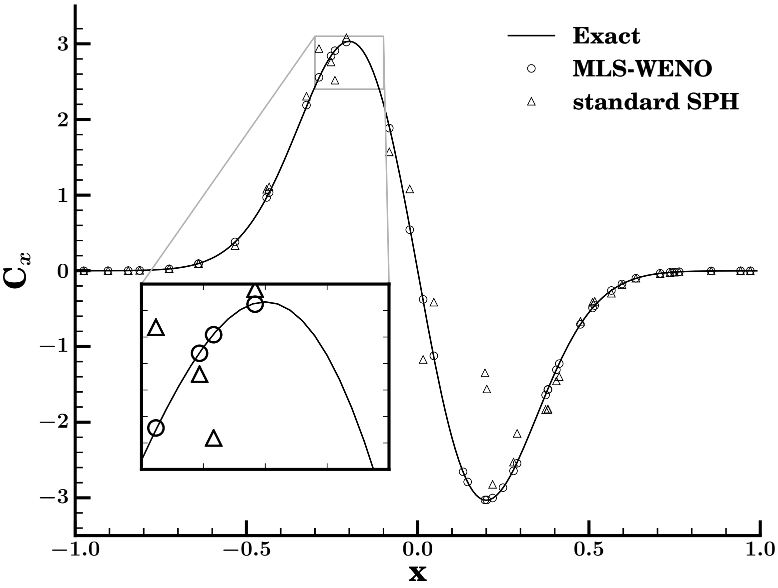

(d)

Figure 3.2: *Comparison of exact and numerical gradient reconstruction for the case of a smooth solution, obtained with standard SPH approach and with the MLS-WENO reconstruction. Equispaced particles and the cut of at y=0 evaluating the reconstructed polynomials on 100 equispaced points **(a)**, **(c)**. Not-equispaced particles and the cut of at y=0 evaluating the reconstructed polynomials on 100 equispaced points **(b)**, **(d)**. Polynomial reconstruction order* $M = 3$, $\sigma = 1.5$, $\sigma_{mls} = 3$.

dx	ε_{L_1}	ε_{L_2}	ε_{L_2}	$O(L_1)$	$O(L_2)$	$O(L_\infty)$	$t_{CPU}(s)$
$MLS-WENO\ M=3$ $(\sigma_{mls}=2.5)$							
0.40E-01	0.39E-03	0.19E-02	0.36E-01	-	-	-	0.58
0.20E-01	0.49E-04	0.23E-03	0.58E-02	2.99	3.05	2.66	3.06
0.10E-01	0.60E-05	0.28E-04	0.83E-03	3.04	3.02	2.80	14.58
0.50E-02	0.74E-06	0.34E-05	0.11E-03	3.02	3.03	2.93	63.05
0.25E-02	0.93E-07	0.43E-06	0.16E-04	2.99	2.99	2.77	249.66
$MLS\ M=4$ $(\sigma_{mls}=2.5)$							
0.40E-01	0.19E-03	0.11E-02	0.18E-01	-	-	-	0.96
0.20E-01	0.13E-04	0.72E-04	0.12E-02	3.92	3.91	3.89	4.84
0.10E-01	0.82E-06	0.46E-05	0.82E-04	3.97	3.98	3.88	21.36
0.50E-02	0.52E-07	0.29E-06	0.54E-05	3.98	3.98	3.94	90.67
0.25E-02	0.32E-08	0.18E-07	0.34E-06	4.00	4.00	3.97	374.68
$MLS\ M=5$ $(\sigma_{mls}=4.0)$							
0.40E-01	0.34E-04	0.15E-03	0.30E-02	-	-	-	1.66
0.20E-01	0.11E-05	0.46E-05	0.95E-04	4.99	5.03	4.99	8.94
0.10E-01	0.35E-07	0.15E-06	0.40E-05	4.97	4.95	4.57	41.33
0.50E-02	0.11E-08	0.47E-08	0.15E-06	4.99	5.00	4.78	179.58
0.25E-02	0.34E-10	0.15E-09	0.50E-08	5.01	5.01	4.86	736.69

Table 3.2: *Numerical convergence results for Gaussian gradient reconstruction with second, third and fourth order version of the MLS-WENO scheme. In the first row the particles distance dx. The second, third and fourth columns contain the error measured in* L_1*,* L_2 *and* L_∞ *norms, followed by three columns giving the measured order of accuracy between the respective particles and the previous particles distributions. The last row gives the CPU time needed by the serial code on Intel(R) Core(TM) i7-2640M CPU 2.80GHz with 8 GB of RAM. The error norms refer to the concentration considering not equispaced particles for the smooth case.*

dx	ε_{L_1}	ε_{L_2}	ε_{L_2}	$O(L_1)$	$O(L_2)$	$O(L_\infty)$	$t_{CPU}(s)$
SPH not equispaced ($\sigma = 1$)							
0.40E-01	0.77E-01	0.24E+00	0.33E+01	-	-	-	0.02
0.20E-01	0.14E+00	0.48E+00	0.73E+01	-0.81	-0.99	-1.13	0.23
0.10E-01	0.28E+00	0.10E+01	0.15E+02	-1.04	-1.06	-1.01	1.26
0.50E-02	0.57E+00	0.20E+01	0.35E+02	-1.02	-1.02	-1.24	5.76
0.25E-02	0.11E+01	0.40E+01	0.74E+02	-1.01	-1.00	-1.10	26.00
SPH not equispaced ($\sigma = 2$)							
0.40E-01	0.48E-01	0.13E+00	0.11E+01	-	-	-	0.03
0.20E-01	0.57E-01	0.19E+00	0.24E+01	-0.26	-0.57	-1.15	0.24
0.10E-01	0.12E+00	0.43E+00	0.60E+01	-1.07	-1.16	-1.30	1.53
0.50E-02	0.24E+00	0.86E+00	0.16E+02	-0.99	-1.00	-1.44	6.92
0.25E-02	0.49E+00	0.17E+01	0.32E+02	-1.02	-1.01	-1.00	28.03
SPH not equispaced ($\sigma = 3$)							
0.40E-01	0.60E-01	0.15E+00	0.10E+01	-	-	-	0.03
0.20E-01	0.24E-01	0.78E-01	0.89E+00	1.32	0.99	0.22	0.26
0.10E-01	0.38E-01	0.14E+00	0.20E+01	-0.68	-0.83	-1.16	1.40
0.50E-02	0.72E-01	0.25E+00	0.46E+01	-0.90	-0.87	-1.22	7.45
0.25E-02	0.14E+00	0.50E+00	0.85E+01	-0.99	-1.00	-0.88	31.18

Table 3.3: *Numerical convergence results for Gaussian gradient reconstruction with standard SPH. In the first row the particles distance dx. The second, third and fourth columns contain the error measured in L_1, L_2 and L_∞ norms, followed by three columns giving the measured order of accuracy between the respective particles and the previous particles distributions. The last row gives the CPU time needed by the serial code on Intel(R) Core(TM) i7-2640M CPU 2.80GHz with 8 GB of RAM. The error norms refer to the concentration considering not equispaced particles for the smooth case.*

3.3.2 Piecewise smooth test case with discontinuity

As a further test we consider the gradient reconstruction of the following two-dimensional piecewise constant function:

$$C(x,y) = \begin{cases} C_0 exp^{-\left(\frac{(x-x_0)}{2\sigma^2} + \frac{(y-y_0)}{2\sigma^2}\right)} & : r \leq 0.3 \\ 0 & : r > 0.3 \end{cases}$$

where $r = \sqrt{(x-x_0)^2 + (y-y_0)^2}$ is the distance from the center of the domain. We propose this test case to show the essentially non-oscillatory reconstruction polynomial behavior that limits the non-monotonic behavior of the MLS reconstruction, although it does not ensure a monotonic preserving reconstruction scheme.

Fig 3.3 shows the gradient reconstruction piecewise smooth test case with discontinuity compare the MLS-WENO and standard SHP numerical solutions with the exact solution. Sub-Figs. 3.3a and 3.3c show the equispaced particles case, and Sub-Figs. 3.3b and 3.3d show the not-equispaced spaced particles case. Similarly to the smooth case, MLS-WENO produces an accurate gradient reconstruction and it does not exhibit oscillations. While, the standard SPH suffers from oscillations of the gradient, which are particularly evident close to the discontinuity for the case of not-equispaced particles.

(*This page has been intentionally left blank*)

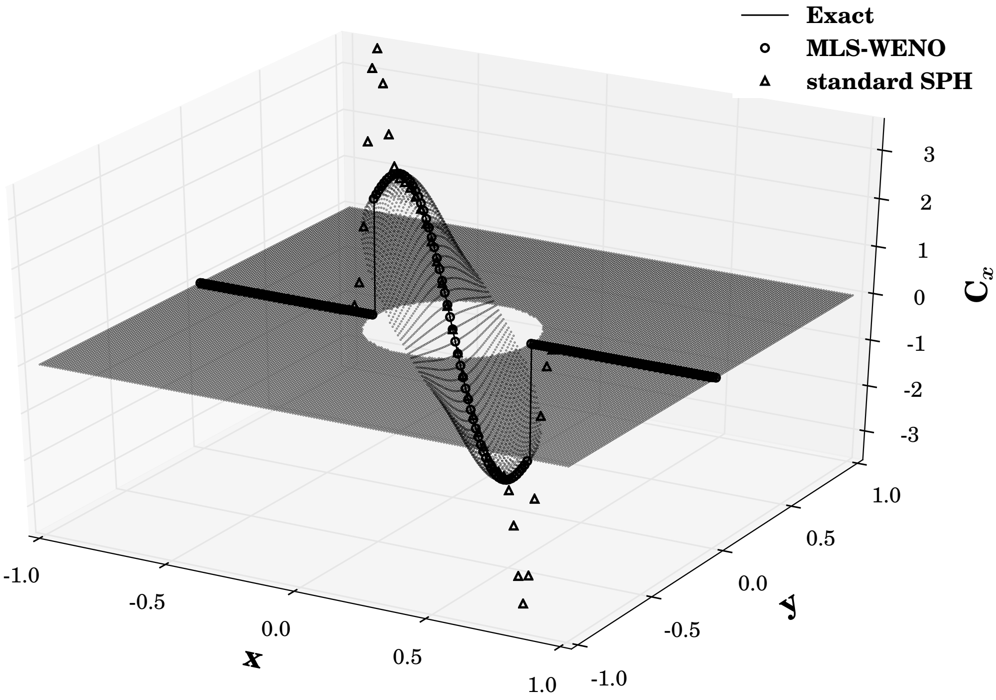
Exact
MLS-WENO
standard SPH
C_x
3
2
1
0
-1
-2
-3
-1.0
-0.5
0.0
0.5
1.0
x
1.0
0.5
0.0
-0.5
-1.0
y

(a)

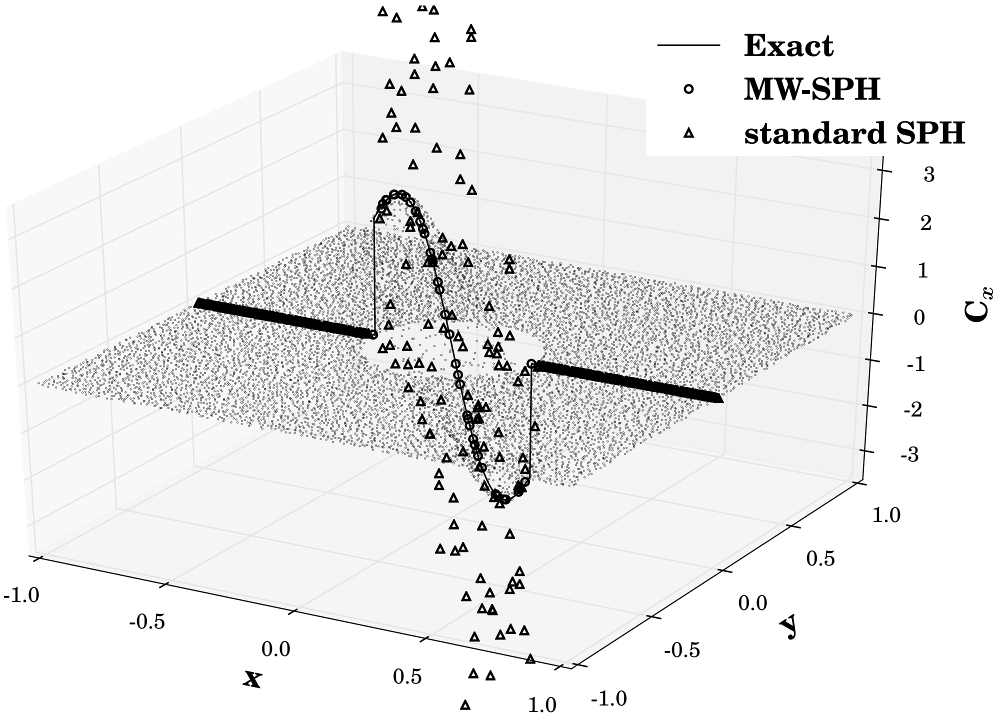
Exact
MW-SPH
standard SPH
C_x
3
2
1
0
-1
-2
-3
-1.0
-0.5
0.0
0.5
1.0
x
1.0
0.5
0.0
-0.5
-1.0
y

(b)

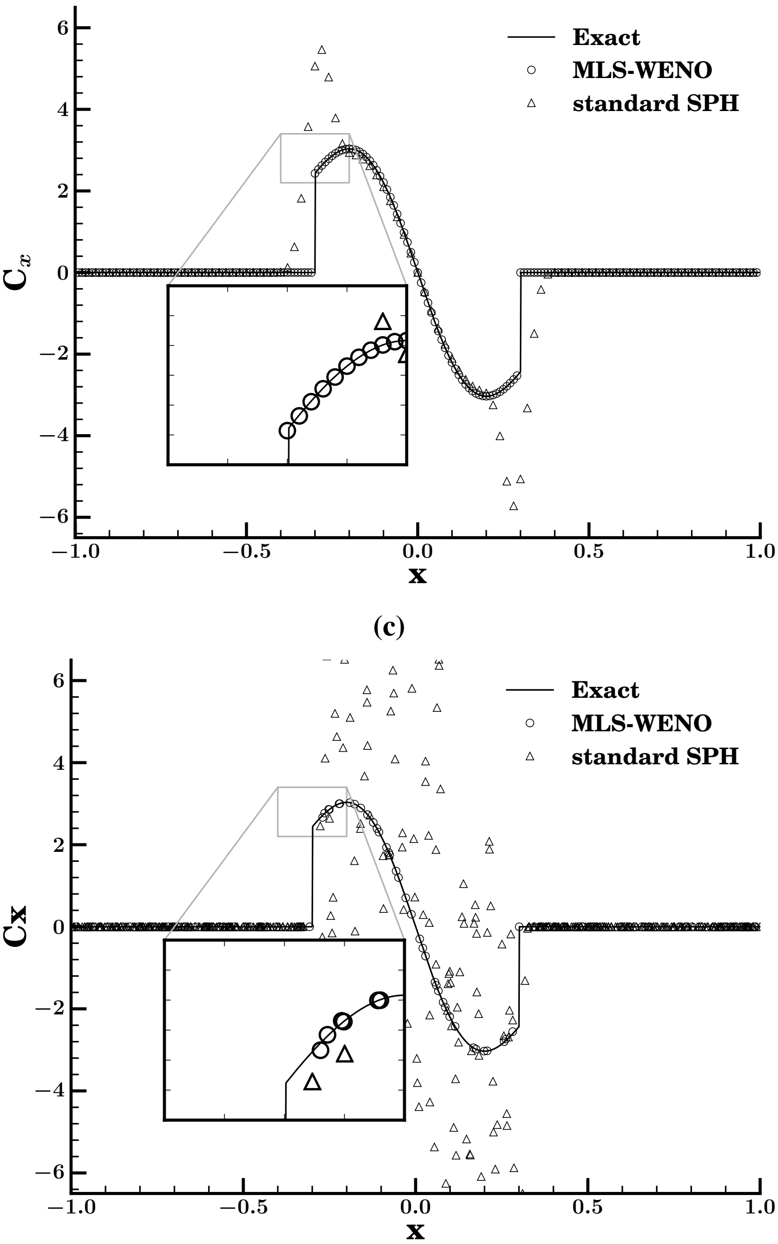

(c)

(d)

Figure 3.3: *Piecewise smooth test case with discontinuity: gradient reconstruction, comparison of exact and numerical solutions obtained with standard SPH approach and with the MLS-WENO reconstruction. Equispaced particles and the cut of at y=0 evaluating the reconstructed polynomials on 100 equispaced points **(a)**, **(c)**. Non-equispaced particles and the cut of at y=0 evaluating the reconstructed polynomials on 100 equispaced points **(b)**, **(d)**. Polynomial reconstruction order* $M = 3$, $\sigma = 1.5$, $\sigma_{mls} = 3$.

3.4 Test case

The aim of this section is to investigate the standard SPH and MWSPH accuracy and positivity preserving properties in case of diffusion phenomena. We consider both homogeneous and heterogeneous flow field. For clarity, we call the MWSPH with third order flux reconstruction MWSPH-M3 as well the MWSPH with fourth order flux reconstruction MWSPH-M4. We take into account anisotropic ratio α_T/α_L in the range $[0.1, 0.01]$ which are similar to the values reported in *Herrera and Beckie* [2012] and based on reasonable physical assumptions.

Following *Boso et al.* [2013], we introduce the dilution index as index of accuracy of the numerical schemes. The dilution index quantifies the distribution in space of the solute mass [*Kitanidis*, 1994]. This means that the intrinsic numerical diffusion directly effects the dilution index. The diluition index is defined as [*Kitanidis*, 1994]:

$$E(t) = \exp\left(-\sum_{k=1}^{N} P_k ln P_k\right) \tag{3.27}$$

where $P_k = C_k/M$ with M the total solute mass in time. In Eqn. (3.27) we consider only concentration larger then $1.e-16$ in order to avoid negative value in logarithm expression. In addition we consider also the dissipation rate χ:

$$\chi(t) = \int_\Omega \nabla C\mathbf{D}\cdot\nabla C d\Omega \tag{3.28}$$

with Ω the computational domain. For the set of discrete particle the dissipation rate is approximated as:

$$\chi(t) = \sum_i = NV_i \nabla C_i \mathbf{D}_i \cdot \nabla C_i. \tag{3.29}$$

We believe that the $\chi(t)$ is a good index for accuracy estimation of the gradient approximation.

3.4.1 Homogeneous

In the present section, we analyze the accuracy and monotonicity properties of standard SPH and MWSPH. We simulate the instantaneous realize of a solute mass in a constant velocity field $\mathbf{v}$ forming an angle of 30^o with respect to the x-axis. This two-dimensional test case is similar to that originally proposed *Herrera and Beckie* [2012] where the analytical solution for the solute concentration in time is given by [*Javandel et al.*, 1984]:

$$C(x,y) = \frac{C_1}{C_4} exp \left(\frac{-(x-x_0)^2 \left(2tD_{\hat{j}\hat{j}} + w^2\right) - (y-y_0)^2 \left(2tD_{\hat{i}\hat{i}} + w^2\right) + 4t(x-x_0)(y-y_0)D_{\hat{i}\hat{j}}}{8t^2C_2^2 + 4w^2tC_3 + 2w^4} \right) \tag{3.30}$$

with $C_1 = C_0 w^2$, $C_2 = D_{\hat{i}\hat{i}} D_{\hat{j}\hat{j}} - 4D^2_{\hat{j}\hat{i}}$, $C_3 = D_{\hat{i}\hat{i}} + D_{\hat{j}\hat{j}}$ and $C_4 = \sqrt{(4t^2C_2 + 2twC_3 + w^4)}$. The exact solution serves as initial condition. Without loss of generality we simulate only the dispersion process neglecting the contribution of advection which can be easily incorporated with a particle tracking without introducing numerical error in case of homogeneous velocity field [*Herrera*, 2009]. In other words, we use the velocity field to define the transport process through the dispersion tensor given by Eqn. (4.8) neglecting the advection contribution given by Eqn. (3.1). As for Section 3.3 we consider both equispaced and not equispaced particles. Table 4.2 shows the parameters in the homogeneous test case.

Parameter	Symbol	Value	Unit
Initial plume width	w	0.2	cm
Maximum initial concentration	C_0	1	mg/L
Length numerical domain	L	1	cm
Longitudinal dispersivity	α_L	0.004	cm
Trasversal dispersivity	α_T	0.0004	cm

Table 3.4: *Homogeneous test case parameters.*

Figs. 3.4-3.5 show the comparison between the numerical solution obtained with standard SPH and with MWSPH with third and fourth order MLS-WENO flux reconstruction. In case of equispaced particles the MWSPH-M3 underestimates the maximum and the standard SPH slightly overestimates the exact solution. However, standard SPH and MWSPH results are comparable. On the contrary, in case of not-equispaced particles, one can clearly see the increase of the accuracy of the MWSPH numerical solution comparing with standard SPH one.

Fig. 3.6 show the maximum concentration in time for standard SPH, MWSPH-M3, MWSPH-M4 and MWSPH-M6 for different smoothing lengths. As already reported by *Herrera* [2009] standard SPH overestimates the maximum concentration. On the other hand MWSPH-M3 tends to underestimates the maximum concentration in time especially for low smooth length. The MWSPH-M4 with higher smoothing length does not underestimate the maximum concentration and it is closer to the analytical solution. All of these behaviors increase in all not-equispaced case. In particular, the error increases in the case of not-equispaced particles for the SPH which is very sensitive to particle positions. On the other hand MWSPH is less sensitive to particle positions and the error in maximum concentration computation stabilizes in time. As expected the MWSPH-M6 produces better results.

Fig. 3.7 compares the evolution of $E(t)$ for different anisotropic ratios for both equispaced and not equispaced particles. The reference solution is computed with the analytic concentration in time provided by Eqn. (4.37). As expected from maximum value analyses, MWSPH-M3 simulates $E(t)$ greater than the reference solution. On the contrary standard SPH and MWSPH-M4 have results similar to the reference solution in case of equispaced particles and lower anisotropic ratio. MWSPH-M4 results slightly more diffusive than standard SPH for higher anisotropic ratio but less sensitive to particle positions. Fig. 3.7.b shows that standard SPH deviates from references solutions for not-equispaced case, in this case $E(t)$ is lower. It indicates that standard SPH underestimates the diffusion between particles. On the other hand, the MWSPH-M6 has better results which are comparable with reference solution in both cases, with equispaced and not equispaced particles.

Fig. 3.8 shows the dissipation rate $\chi(t)$. In all cases taken into account, the MWSPH matches the reference solution. As expected from gradient test cases, standard SPH underestimates the reference solution and it results sensitive to particle positions.

Regarding the positivity preserving properties of the standard SPH and the proposed MWSPH, we study the temporal evolution of minimum simulated concentration as shown in Fig. 3.9. The MWSPH simulates minimum concentration values that are many orders of magnitude smaller than the ones computed with the standard SPH scheme. As the standard Eulerian mesh based WENO, MWSPH has an oscillatory behavior in the minimum concentration that stabilizes in time. Unlike the standard SPH, the minimum in absolute value does not increase with time. This further demonstrates that also in this case the WENO is able to limit the effects of non monotonicity inherent in a high order reconstruction even for long simulation times. On the contrary in the SPH the positivity preserving property decreases in time. The degree of anisotropy has virtually no influence on MWSPH. On the contrary the minimum concentration computed with standard SPH increases in absolute value with the anisotropic ratio. Similarly standard SPH is sensitive

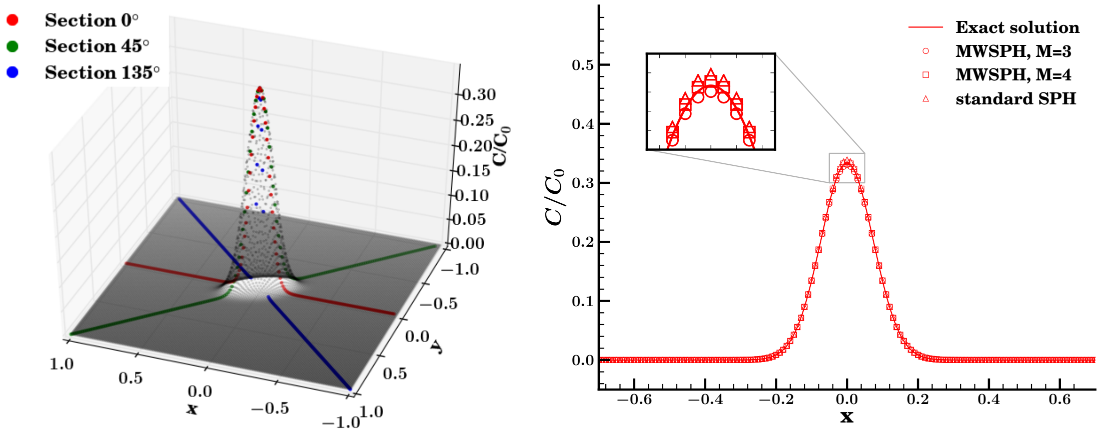

(a) *2D concentration distribution.* **(b)** *Section* 0^o

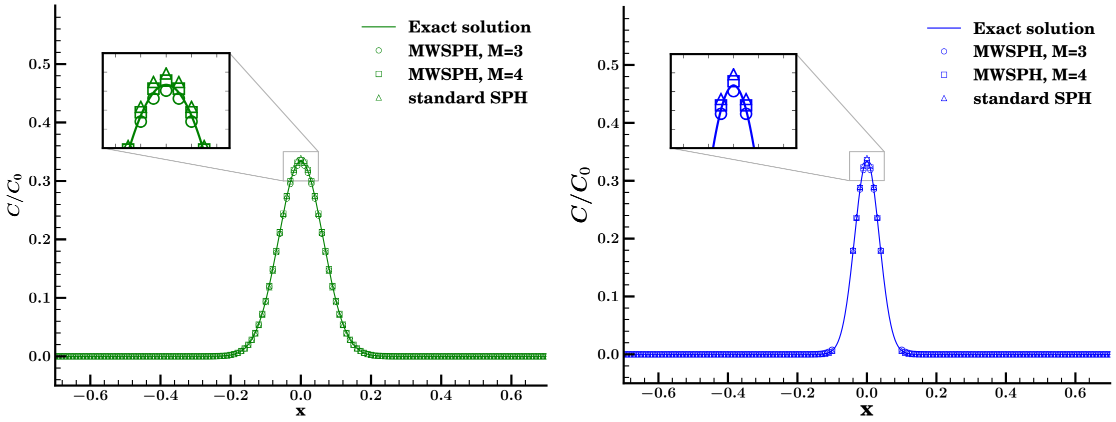

(c) *Section* 45^o **(d)** *Section* 135^o

Figure 3.4: *Comparison of exact and numerical solutions for equispaced particles at time* $t = 1000$ *obtained with standard SPH and different MWSPH with different reconstruction order. Three cuts along different sections (see Fig. 3.4a) are shown evaluating the numerical solution on* 200×200 *not-equispaced particles after 61 time step.* $\sigma = 2.5$*,* $\sigma_{mls} = 4.5$*,* $CFL = 0.9$ *and* $\beta = 30°$.

to the smoothing length, which is less evident in the MWSPH. Fig. 3.10 shows where negative concentrations occur. Standard SPH exhibits negative concentrations in bands aligned with the main direction of the flow. This behavior of standard SPH has been already reported in *Herrera and Beckie* [2012]. Similarly MWSPH has negative concentration bands but in this case they are at the boundary of the computational domain and far from the plume.

Finally we perform a comparative numerical convergence analysis between MWSPH

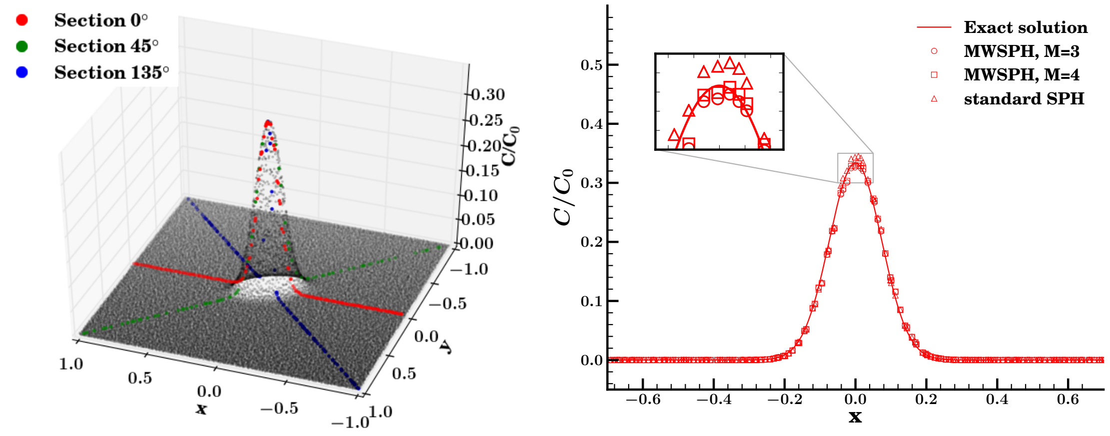

(a) *2D concentration distribution.* **(b)** *Section* 0^o

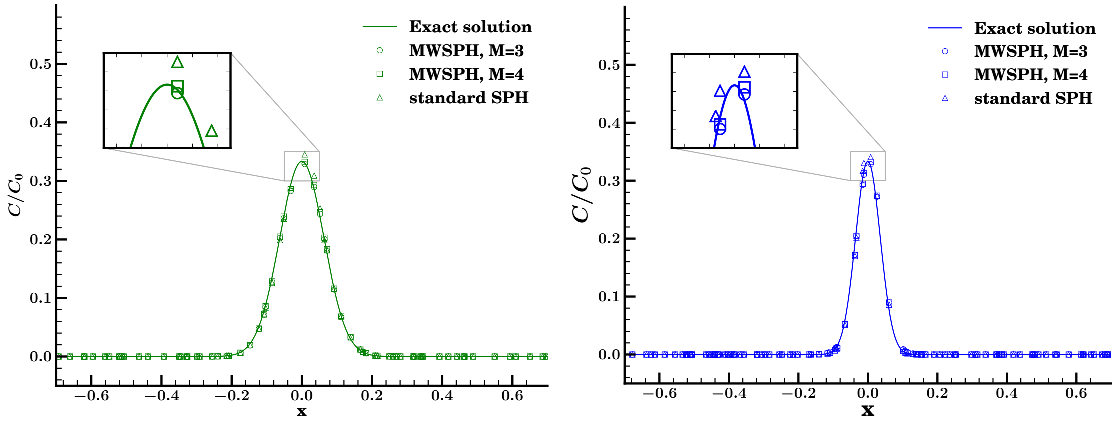

(c) *Section* 45^o **(d)** *Section* 135^o

Figure 3.5: *Comparison of exact and numerical solutions for not-equispaced particles at time* $t = 1000$ *obtained with standard SPH and different MWSPH with different reconstruction order. Three cuts along different sections (see Fig. 3.4a) are shown evaluating the numerical solution on* 200×200 *not-equispaced particles after 61 time step.* $\sigma = 2.5$, $\sigma_{mls} = 4.5$, $CFL = 0.9$ *and* $\beta = 30°$.

and standard SPH using a sequence of successively refined particles. These different runs and results are summarized in Table 3.5. The computational errors of MWSPH and SPH are similar only in the case of the largest particle spacing test. We noted a marked increase in the convergence rate when the highest number of particles are considered. Similarly, MWSPH shows higher accuracy than standard SPH increasing the number of particles. For sake of completeness a graphical illustration of the L_1 error and convergence rate are given in Fig. (3.11). From Fig. 3.12 it is also clear the increase of the numerical accuracy

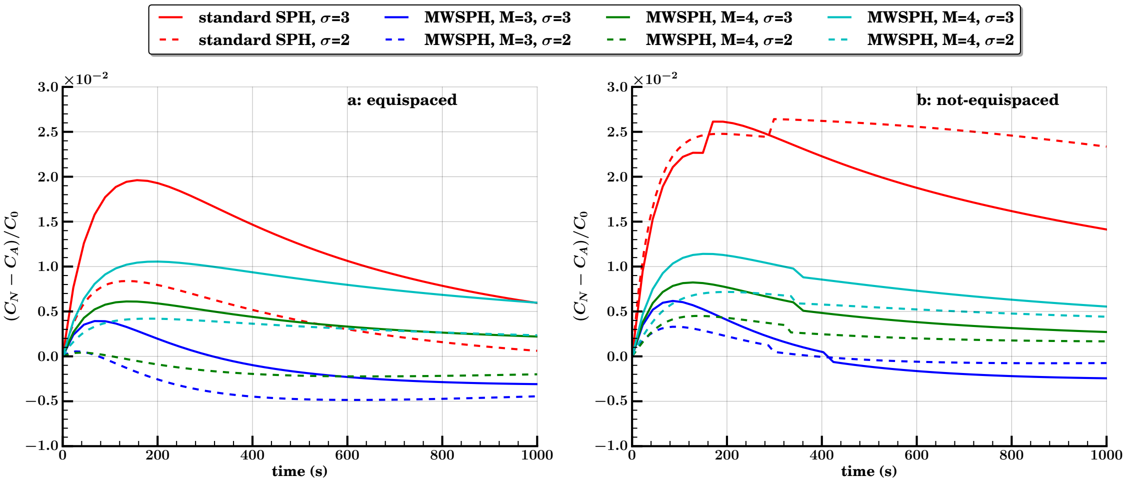

Figure 3.6: *Difference between maximum concentration values of numerical (C_N) and analytical (C_A) solutions as function of time for equispaced particles (on the left) and not-equispaced particles (on the right), for different σ, comparing standard SPH and MWSPH with different reconstruction order M, $\sigma_{mls} = 4.5$ and $CFL = 0.9$.*

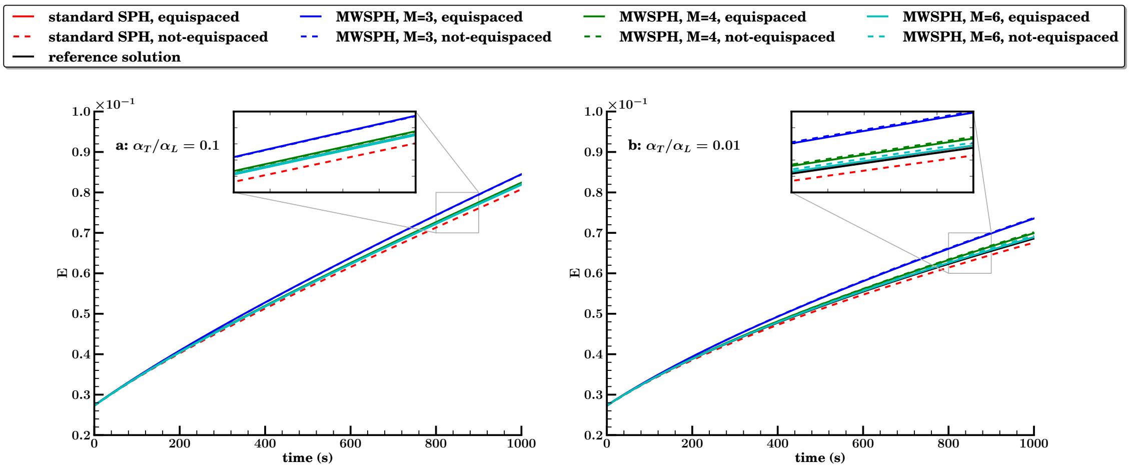

Figure 3.7: *Dilution index for equispaced particles and not-equispaced particles, $\alpha_T/\alpha_L = 0.1$ (on the left) and $\alpha_T/\alpha_L = 0.01$ (on the right), comparing standard SPH and MWSPH with different reconstruction order M, $\sigma_{mls} = 4.5$, $CFL = 0.9$ and $\sigma = 3$.*

of the MWSPH numerical solution comparing with standard SPH when using high order polynomial reconstructions. To give the reader a possibility to assess the computational effort, we report the computational time in Table 3.5 and we give a graphical summary

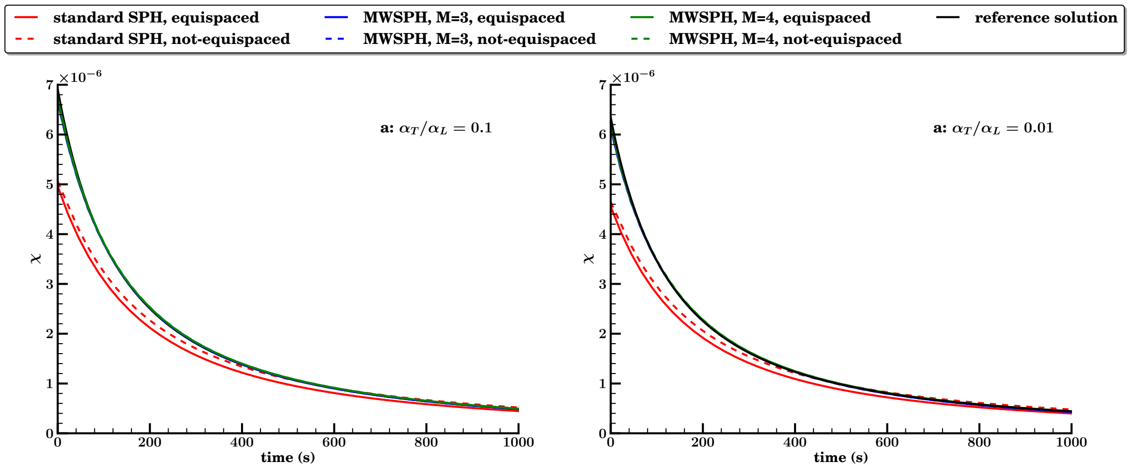

Figure 3.8: *Dissipation rate rate for equispaced particles and not-equispaced particles, $\alpha_T/\alpha_L = 0.1$ (on the left) and $\alpha_T/\alpha_L = 0.01$ (on the right), comparing standard SPH and MWSPH with different reconstruction order M, $\sigma_{mls} = 4.5$, $CFL = 0.9$ and $\sigma = 3$.*

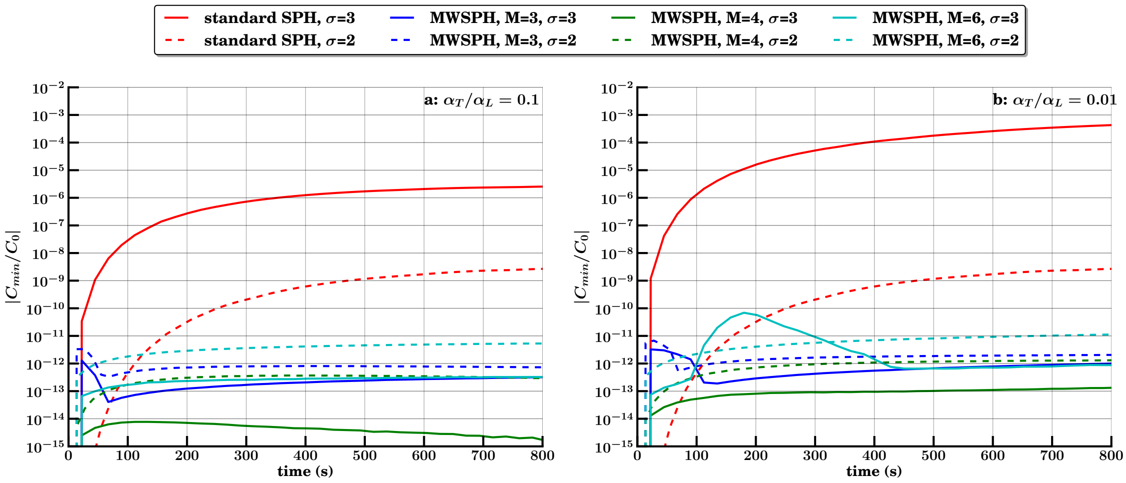

Figure 3.9: *Minimum concentration for different anisotropic ratio, $\alpha_T/\alpha_L = 0.1$ (on the left) and $\alpha_T/\alpha_L = 0.01$ (on the right), for different σ. Standard SPH and MWSPH with different reconstruction order M, $\sigma_{mls} = 4.5$ and $CFL = 0.9$.*

illustration of CPU time in Fig. 3.12. We note that MWSPH increases the total CPU time at most by a factor of two order of magnitude compared to standard SPH. This is essentially due to MLS-WENO reconstruction and to build-up of the stencils. However, MWSPH exhibits an higher convergence rate and accuracy making MWSPH advantageous

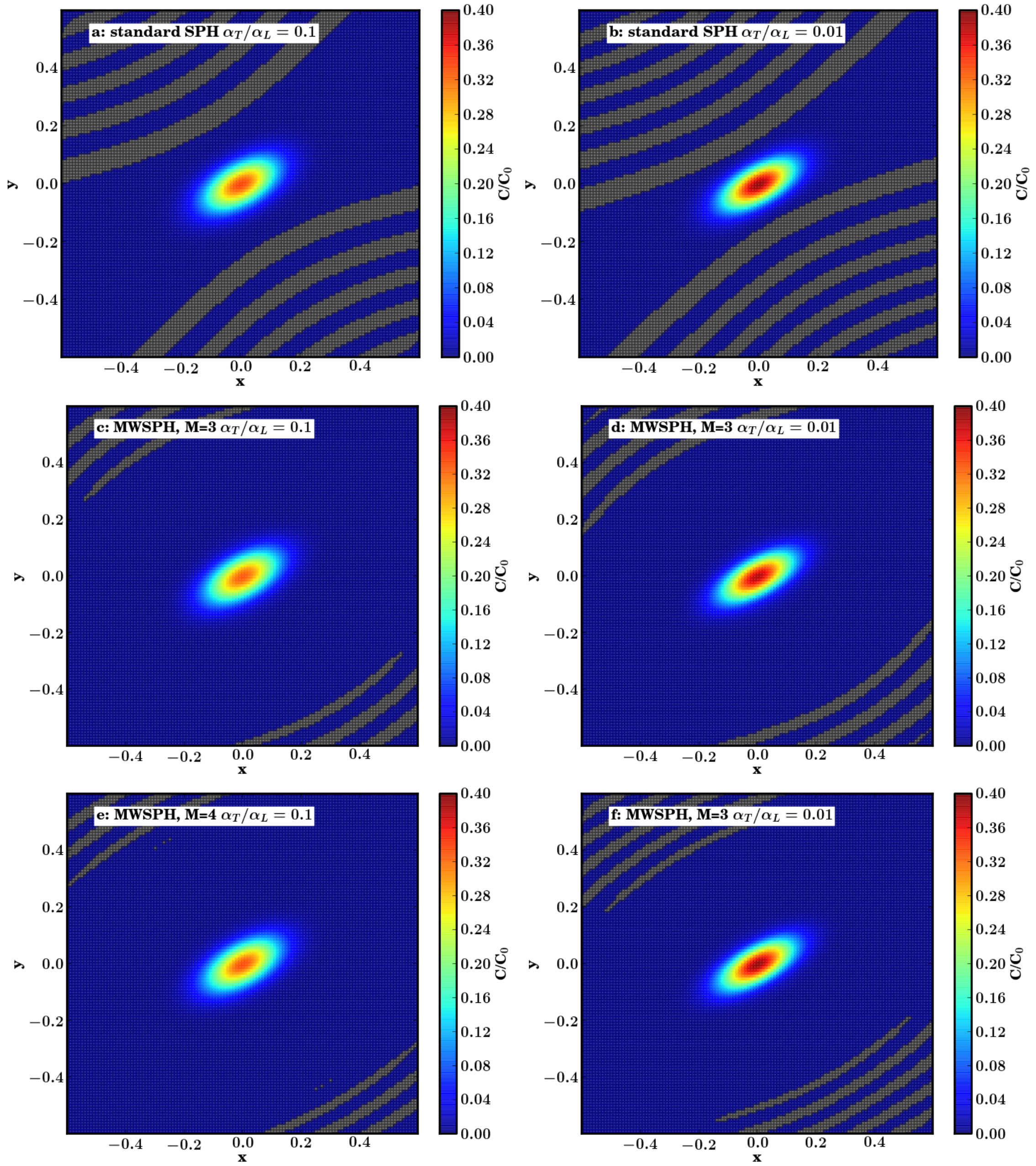

Figure 3.10: *Concentration distribution at time t=10 obtained with standard SPH scheme and different MWSPH orders, for different anisotropic ratio on* 200×200 *equispaced particles after 74 time step.* $\sigma = 3.0$, $\sigma_{mls} = 4.5$, $CFL = 0.9$ *and* $\beta = 30°$. *All cases exhibit negative concentrations (gray bands).*

in cases where a high accuracy is required.

dx	ε_{L_1}	ε_{L_2}	ε_{L_∞}	$O(L_1)$	$O(L_2)$	$O(L_\infty)$	$t_{CPU}(s)$
$standardSPH$ ($\sigma = 3.0$)							
0.20E-01	0.10E-03	0.11E-04	0.29E-01	-	-	-	3.84
0.10E-01	0.33E-04	0.17E-05	0.75E-02	1.66	2.74	1.96	26.17
0.50E-02	0.17E-04	0.42E-06	0.34E-02	0.94	2.03	1.14	250.96
0.25E-02	0.15E-04	0.17E-06	0.25E-02	0.18	0.13	0.44	17718.67
$MWSPH\ M = 3$ ($\sigma = 3.0$)							
0.20E-01	0.15E-03	0.13E-04	0.29E-01	-	-	-	197.11
0.10E-01	0.29E-04	0.13E-05	0.64E-02	2.34	3.24	2.17	1731.15
0.50E-02	0.37E-05	0.10E-06	0.95E-03	3.01	3.76	2.76	18491.27
0.25E-02	0.11E-05	0.17E-07	0.40E-03	1.75	2.55	1.25	158064.79
$MWSPH\ M = 4$ ($\sigma = 3.0$)							
0.20E-01	0.15E-03	0.13E-04	0.29E-01	-	-	-	222.82
0.10E-01	0.29E-04	0.13E-05	0.64E-02	2.36	3.18	2.17	1996.12
0.50E-02	0.37E-05	0.10E-06	0.95E-03	3.24	3.00	1.76	19459.43
0.25E-02	0.11E-05	0.17E-07	0.40E-03	1.53	2.40	1.20	212704.79

Table 3.5: *Numerical convergence result for anisotropic diffusion test case with standard SPH, third and fourth order fluxes reconstruction order.In the first row the particles distance dx. The second, third and fourth columns contain the error measured in* L_1 *,* L_2 *and* L_∞*, followed by three columns giving the measured order of accuracy between the respective particles and the previous particles distributions. The last row gives the CPU time needed by the serial code on Intel(R) Core(TM) i7-2640M CPU 2.80GHz with 8 GB of RAM. The error norms refer to the concentration considering equispaced particles for the homogeneous test case at time* $t = 200$.

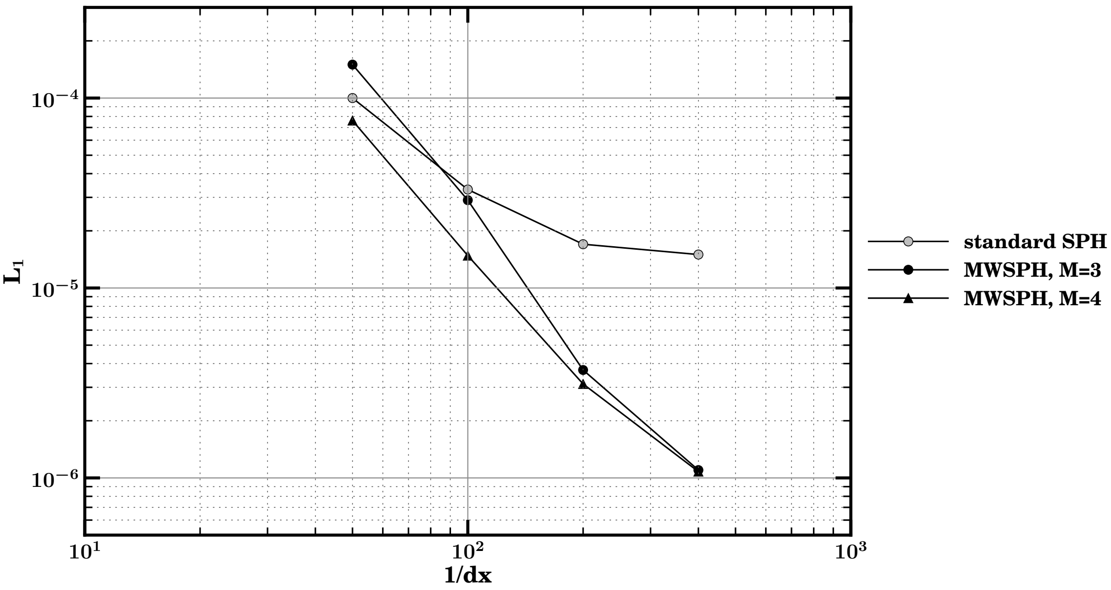

Figure 3.11: *Error norm L_1 computed for homogeneous test case with equispaced particles, $\sigma = 3$, $CFL = 0.9$.*

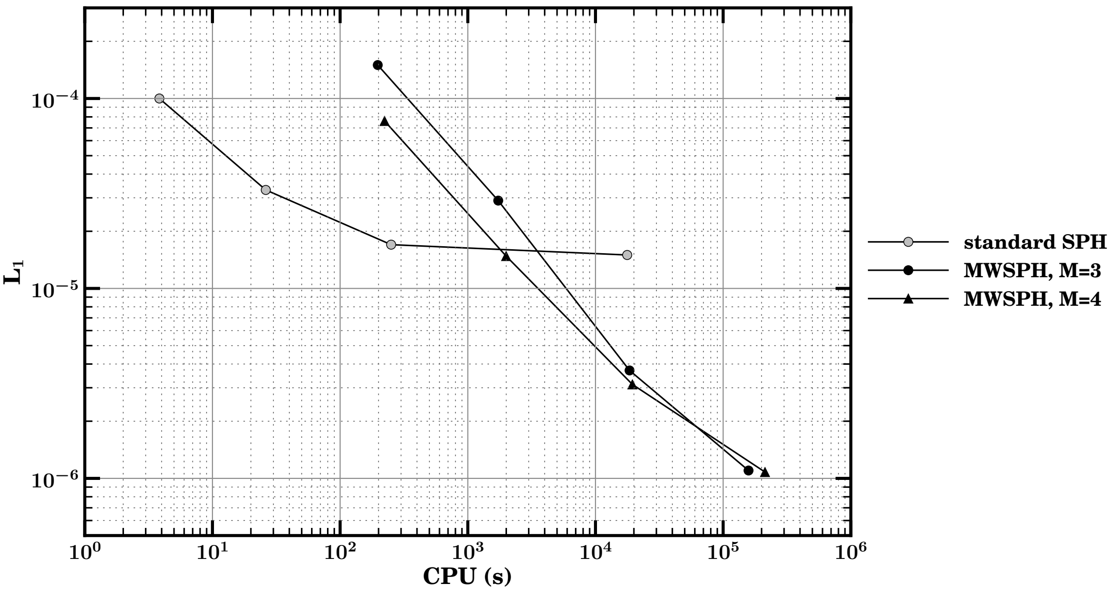

Figure 3.12: *Error norm L_1 computed for homogeneous test case with equispaced particles and computational time on a single processor Intel(R) Core(TM) i7-2640M CPU 2.80GHz.*

3.4.2 Heterogeneous

In this section, previous test cases are modified using heterogeneous flow field. The flow field is taken from the Reference *Nakshatrala et al.* which is defined as

$$v_x(x,y) = 1 + \sum_{k=1}^{3} A_k \frac{n_{yk}\pi}{L_y} \cos\left(\frac{n_{xk}\pi x}{L_x} - \frac{\pi}{2}\right) \cos\left(\frac{n_{yk}\pi y}{L_y}\right) \tag{3.31a}$$

$$v_y(x,y) = 1 + \sum_{k=1}^{3} A_k \frac{n_{yk}\pi}{L_x} \sin\left(\frac{n_{xk}\pi x}{L_x} - \frac{\pi}{2}\right) \sin\left(\frac{n_{yk}\pi y}{L_y}\right) \tag{3.31b}$$

where $m = 3$, $(n_{x1}, n_{x2}, n_{x3}) = (4,5,10)$, $(n_{y1}, n_{y2}, n_{y3}) = (1,5,10)$, $(A_1, A_2, A_3) = (8,2,1)$, and $L_x = L_y = 81$. Fig. (3.13b) shows the velocity field. Figure (3.13a) shows the initial conditions: an instant injection in a square zone with width $S_x = S_y = 30$ with initial concentration $C_0 = 1$. The particles are initially equispaced on a regular square lattice as shown (3.13b) and the longitudinal dispersivity α_L is set equal as 0.1.

Fig. 3.14 shows that, in heterogeneous case, the same trends illustrated for homogeneous cases occurs. All numerical schemes exhibit negative concentration: the standard SPH exhibits negative concentrations on all computational domain and standard SPH is more sensitive to anisotropic ratio. In standard SPH, the number of particles effected by negative concentrations increases with the anisotropic ratio and the negative concentrations are closer to the main plume.

In addition Fig. 3.15 shows that standard SPH not only has higher negative concentration than MWSPH, but that negative concentration increases in proximity of the main plume.

Fig. 3.16 further underlines the difference between the two schemes. As for homogeneous case, standard SPH has the minimum concentration lower than MWSPH of different magnitude order and the minimum concentration increases with the anisotropic ratio. On the other hand, MWSPH-M3 and MWSPH-M4 have a more marked difference in the minimum concentrations.

Fig. 3.18 compares the dilution index for different anisotropic ratios. In particular the standard SPH shows lower values in time with respect to MWSPH. On the other hand both MWSPH-M3 and MWSPH-M4 exhibit similar results. We believe that this behavior is due to not monotonicity preserving property of SPH. The standard SPH overestimates the maximum concentrations (Fig. 3.17) leading to a higher values in the dilution index.

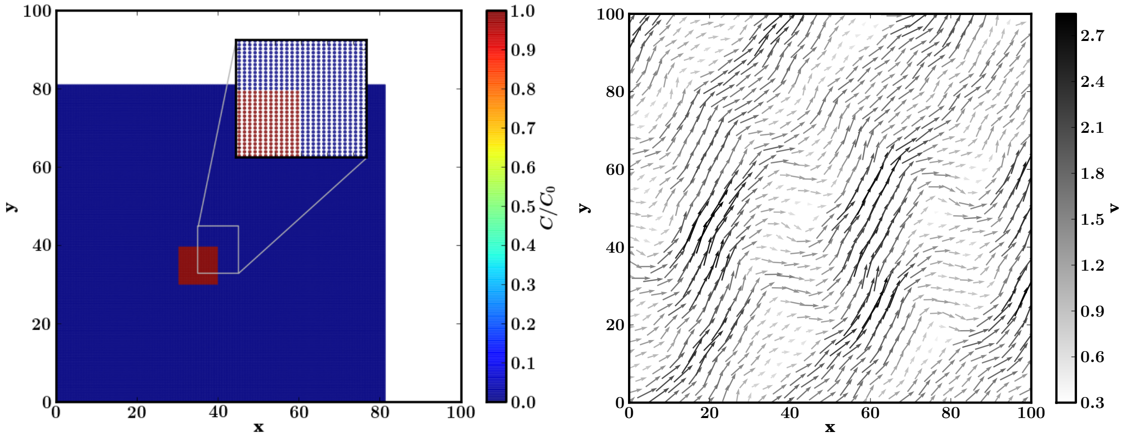

(a) *Initial conditions and particle positions* **(b)** *Flow field*

Figure 3.13: *Initial conditions on the left and velocity field on the right for heterogeneous test cases.*

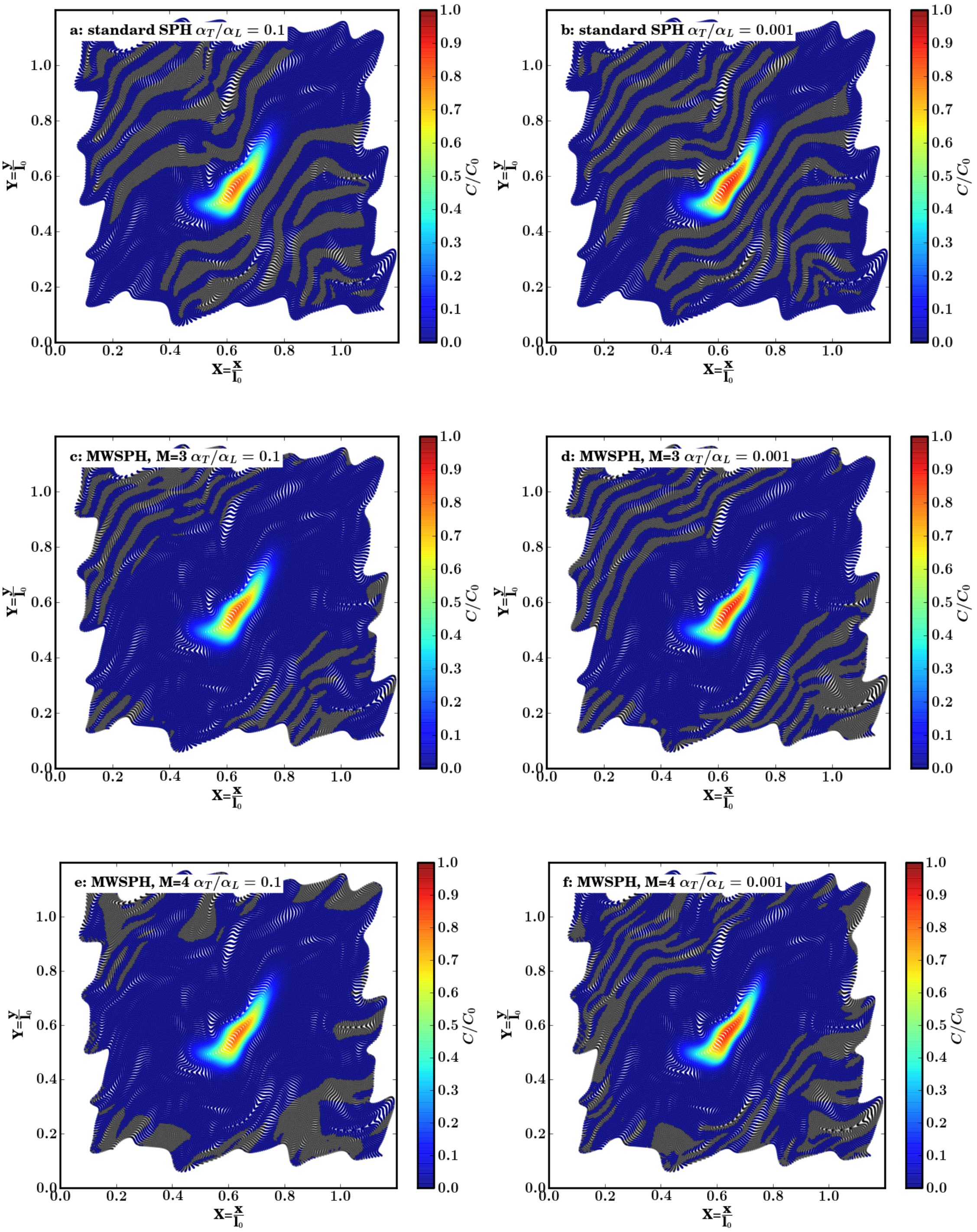

Figure 3.14: *Concentration distribution at time* $t = 1000$ *obtained with standard SPH scheme and different MWSPH orders, for different anisotropic ratio with* 200×200 *particles after 32 time step for heterogeneous test cases.* $\sigma = 3.0$, $\sigma_{mls} = 4.5$, $CFL = 0.9$. *All cases exhibit negative concentrations (gray bands).*

(a) *standard SPH, anisotropic ratio 0.1* **(b)** *standard SPH, anisotropic ratio 0.001*

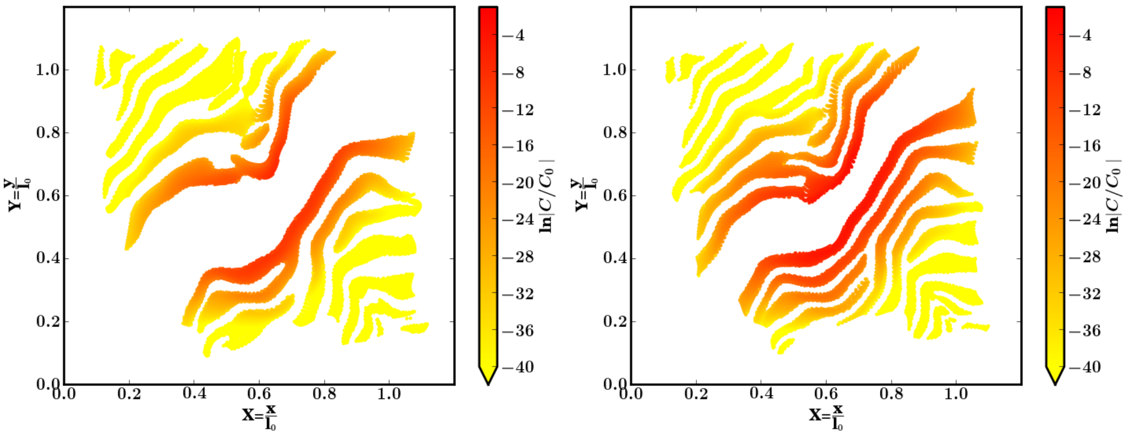

(c) *MWSPH M=3, anisotropic ratio 0.1* **(d)** *MWSPH M=3, anisotropic ratio 0.001*

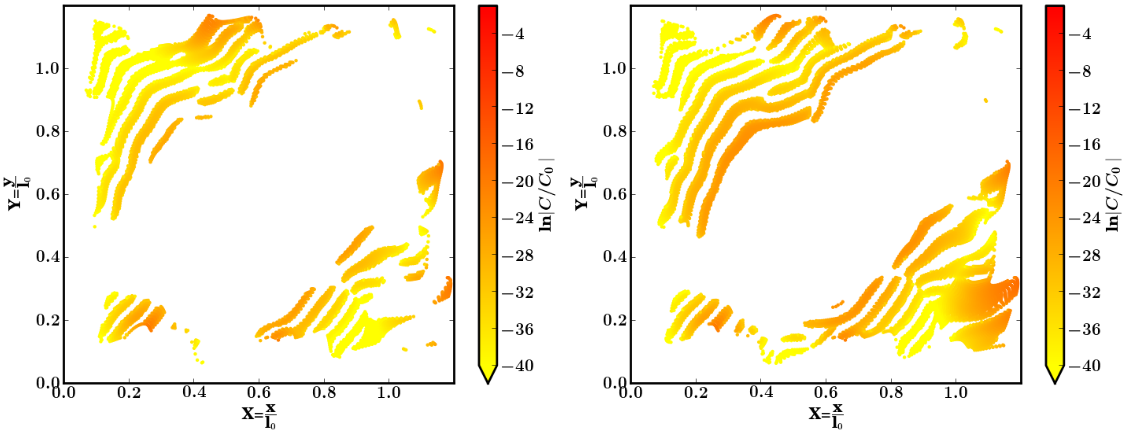

(e) *MWSPH M=4, anisotropic ratio 0.1* **(f)** *MWSPH M=4, anisotropic ratio 0.001*

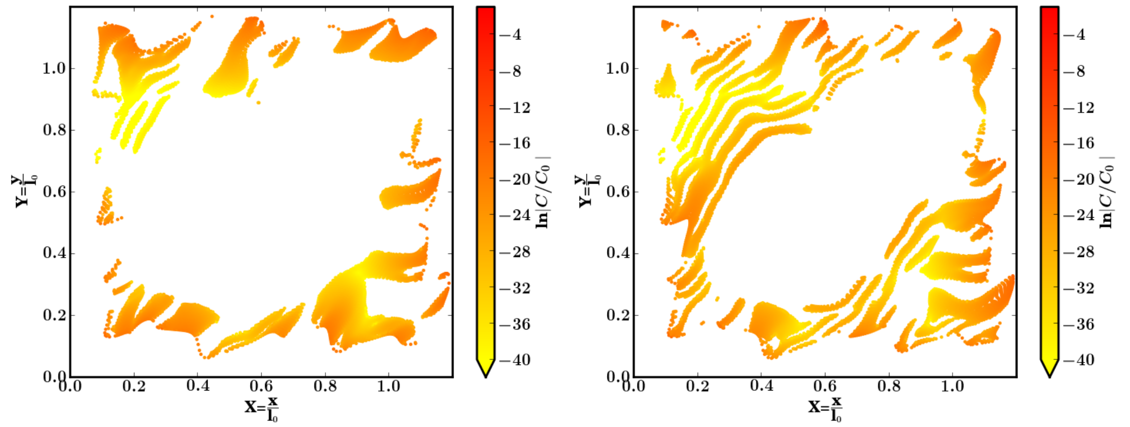

Figure 3.15: *Negative concentration distribution for heterogeneous case at final simulation time. Comparison of the standard SPH with the MWSPH scheme for different reconstruction order of accuracy,* $\sigma = 3.0$, $\sigma_{mls} = 4.5$, $CFL = 0.9$.

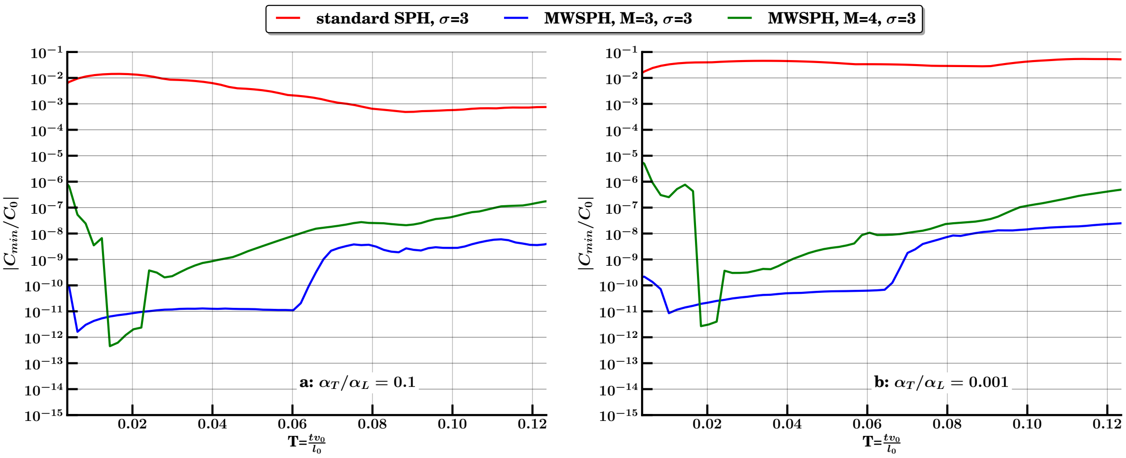

Figure 3.16: *Negative concentration distribution for heterogeneous case. Comparison of the standard SPH with the MWSPH scheme with third reconstruction order of accuracy,* $\sigma = 3.0$, $\sigma_{mls} = 4.5$, $CFL = 0.9$.

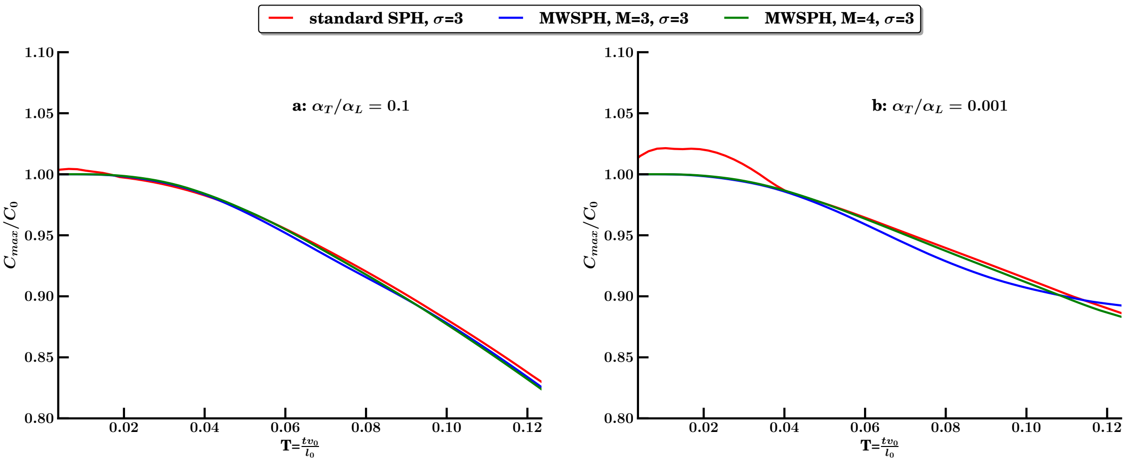

Figure 3.17: *Maximum concentration in time for standard SPH and MWSPH scheme with third and fourth flux reconstruction order of accuracy,* $\sigma = 3.0$, $\sigma_{mls} = 4.5$, $CFL = 0.9$.

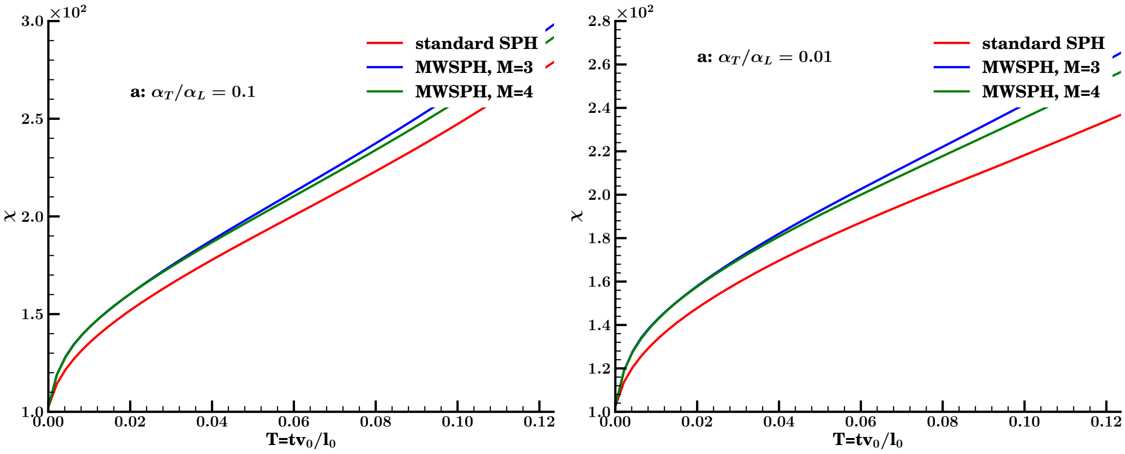

Figure 3.18: *Dilution index, heterogeneous case,* $\sigma = 3$, $\sigma_{mls} = 4$, $CFL = 0.9$.

3.5 Conclusion

In this work we have derived a new SPH formulation based on MWSPH to simulate anisotropic diffusion in porous media. We have compared the performance of MWSPH simulating the instantaneous release of a solute mass with anisotropic diffusion tensor considering different anisotropic ratios and particle distributions in both homogeneous and and heterogeneous flow field. Both the standard SPH and the MWSPH exhibit negative concentrations. Nevertheless, in case of the MWSPH, the unphysical negative concentration results limited in time and lower of many order of magnitude than negative concentration computed with the standard SPH. Convergence analysis show that the MWSPH is more accurate than standard SPH, which is less computation time demanding but with a lower convergence rate with respect to MWSPH.

In the more general SPH scheme framework, MWSPH seems to be the only option when the anisotropic diffusion equation can not be solve uncoupled with the flow fields, the MWSPH ensures at the same time accuracy and it limits the not-positivity preserving properties of SPH.

4 An alternative SPH formulation to model chemotaxis in porous media

Chemotaxis is the ability of some bacteria to swim toward or away chemical concentrations [*Long and Ford*, 2009; *Pedit et al.*, 2002; *Alt*, 1980; *Erban et al.*, 2004]. Chemotactic bacteria can sense and measure local chemical gradient and direct their tumble motion in the direction of chemical attractant [*Ford and Harvey*, 2007a]. This single bacteria migration results in concentration bacteria motion that can reach velocity comparable to groundwater flow velocity [*Rivero et al.*, 1989; *Long and Ford*, 2009; *Valdés-Parada et al.*, 2009a]. This means that bacteria can potentially reach low permeability area, where usually the contaminant are trapped, improving the standard bioremediation techniques.

Early works focused on the development of effective medium coefficients of chemotaxis within porous medium [*Duffy et al.*, 1997; *Ford and Harvey*, 2007a]. *Long and Ford* [2009]; *Wang and Ford* [2009] reported an increase of transverse migration of bacteria induced by chemotaxis in laboratory scale porous media models for both homogeneous and heterogeneous cases. Lattice Boltzmann and Monte Carlo approaches have been developed to study chemotaxis in porous medium under groundwater flow conditions. *Valdés-Parada et al.* [2009a] derives the effective-medium advection-diffusion with chemotaxis equations with the method of volume averaging and *Porter et al.* [2011] presents a predictive multiscale modeling framework for chemotaxis in porous media. These experimental and theoretical works suggest that the effects of chemotaxis are visible where the flow conditions are such as not dissipate the chemical solute gradients within the porous media. Therefore, modeling chemotaxis requires special care of low solute concentrations and solute gradients to correctly simulate chemotactic bacteria response. Unfortunately, traditional numerical scheme adds artificial numerical diffusion, this leads to the dissipation of the real solute interfaces gradient canceling or inhibiting the chemotaxis bacteria behavior.

Recently *Boso et al.* [2013] compared the accuracy of five different numerical schemes in solving the solute transport equation and analyzing the artificial numerical diffusion add in the discretization of both passive and reactive solute transport in porous media. This work indicates that the Smooth Particle Hydrodynamics (SPH) scheme add a null or small amount of artificial diffusion even in advection dominant flow, where usually traditional schemes fail. The SPH is a meshless numerical scheme where the continuum is discretized with a set of particles carrying solute concentrations [*Herrera et al.*, 2009, 2010]. Unlike traditional Random Walk Particle Tracking scheme, particles do not carry solute mass. This implies that the numerical precision to represent the concentration values does not depend on the number of particles but on the hardware representation precision. The reactions can be computed at each particles without any background grid. SPH results accurate and able to reproduce correctly small scale concentrations [*Boso et al.*, 2013; *Herrera et al.*, 2009, 2010]. These features makes the SPH the ideal scheme for the study of chemotaxis in porous media.

Unfortunately, the standard SPH has some limitations. As we show later, in the case of chemotaxis the bacteria have two advection field: one due to the fluid flow field and one due to the chemotaxis. This makes the extension of standard SPH to chemotaxis not straightforward. On the other hand, despite the accuracy in the numerical solution, SPH does not compute the solute gradient properly which is fundamental in chemotaxis velocity estimation [*Avesani et al.*, 2014]. SPH usually underestimate the gradients or produces unphysical oscillations in the gradient when particles are not equidistant such as when particles moves according to a irregular flow field.

Motivated by above, the primary goal of this paper is to develop an alternative SPH formulation to correctly model chemotaxis in porous media. Recently *Avesani et al.* [2014] introduces a a new class of Moving Least Squares WENO-SPH Schemes, based on Ben Moussa & Vila SPH formulation [*Vila*, 1999; *Ben Moussa et al.*, 1999], hereafter refer as MWSPH. The MWSPH uses high order moving-least-squares WENO reconstruction and Riemann solvers to evaluate fluxes between interacting particles. This scheme is very accurate in evaluations of spatial derivatives which is crucial in chemotactic velocity estimation [*Rivero et al.*, 1989]. The new key idea consists of model the chemotaxis using a monotone upwind flux in a relative moving frame with moving particles. The main advantages of the proposed method are: (i) like traditional streamlines methods, it is well suited to simulate solute transport in porous media because of the elimination of artificial numerical diffusion, ii) it provides a robust mechanism to incorporate chemotaxis in the SPH bases schemes overcoming its limitations, iii) it accurately computes gradients regardless of the position of the particles.

The paper is organized as follows: in section 4.1 the mathematical model for chemotaxis in porous media is briefly presented. In section 4.2, we first present the standard SPH describing its limits in chemotaxis applications. Section 4.3 describes an alternative SPH formulation to incorporate properly the chemotaxis in the SPH framework. In section 4.4, the new SPH scheme is tested with respect to analytical solutions and some numerical experiment show some possible applications. Finally in section 4.5, we discuss our general conclusions with some remarks.

4.1 Mathematical Modeling

For sake of clearness and without losing generalization we limit ourself to one bacteria species and one attractant species. The governing equation for bacteria transport in porous media including chemotaxis are:

$$\frac{\partial c_a}{\partial t} + \nabla \left(\mathbf{v}_f c_a\right) = \nabla \cdot \left(\mathcal{D}_a \nabla c_a\right), \tag{4.1}$$

for attractant and

$$\frac{\partial c_b}{\partial t} + \nabla \left(\mathbf{v}_f c_b\right) + \nabla \left(\mathbf{v}_c c_b\right) = \nabla \cdot \left(\mathcal{D}_b \nabla c_b\right), \tag{4.2}$$

for bacteria. In Eqns. (4.1)-(4.2) c_a and c_b are the attractant and bacteria concentration respectively, $\mathbf{v}_f$ is the fluid velocity and the terms $\mathcal{D}_a$ and $\mathcal{D}_b$ denotes the molecular diffusion coefficient for the attractant and for bacteria respectively. The so called chemotactic velocity vector $\mathbf{v}_c$ represents the bacteria response to attractant transport. The general expression for chemotactic velocity reads as follows [*Chen et al.*, 1998; *Rivero et al.*, 1989]:

$$\mathbf{v}_c = \frac{2}{3} v_s tanh \left(\frac{\chi_0}{2 v_s} \frac{k_d \|\nabla c_a\|}{\left(k_s + c_a\right)^2} \right) \frac{\nabla c_a}{\|\nabla c_a\|} \tag{4.3}$$

where v_s is the mean bacteria swimming speed, χ_0 is the chemotactic sensitivity coefficient, k_d is the dissociation constant that represents the ability of the bacteria to sense gradients of the attractant in the surrounding. In scientific literature other different formulation have been proposed, see for example [*Keller and Segel*, 1971a,b; *Odell and Keller*, 1976; *Chen et al.*, 1998; *Ford and Harvey*, 2007a]. For example *Frymier and Ford* [1997] take into account the effect of porous media surface on chemotactic velocity.

According to SPH formalism is useful to rewrite Eqns. (4.1)-(4.2) in a Lagrangian framework as:

$$\frac{dc_a}{dt} = \nabla \cdot (\mathcal{D}_a \nabla c_a); \tag{4.4a}$$

$$\frac{d\mathbf{r}}{dt} = \mathbf{v}_f; \tag{4.4b}$$

$$\tag{4.4c}$$

for attractant, and

$$\frac{dc_B}{dt} = \nabla \cdot (\mathcal{D}_\mathcal{B} \nabla c_B); \tag{4.5a}$$

$$\frac{d\mathbf{r}}{dt} = \mathbf{v}_f + \mathbf{v}_c; \tag{4.5b}$$

$$\tag{4.5c}$$

for bacteria. Here $\frac{d}{dt}$ denotes the total derivative that follows the motion of the fluid and $\mathbf{r}$ the position of the infinitesimal control volume. Eqns. (4.1-4.2) represent the transports processes in porous media at microscale, whose solutions is impracticable at field scale in order to quantify the contribution of chemotaxis to bacteria transport.

Starting from Eqns. (4.1) and (4.2) using the method of volume averaging, *Valdés-Parada et al.* [2009a] derived the effective medium mass balance equations for chemotaxis, which reads as:

$$\frac{dC_a}{dt} = \nabla \cdot (\mathbf{D}_a \nabla C_a); \tag{4.6a}$$

$$\frac{d\mathbf{r}}{dt} = \mathbf{V}_f; \tag{4.6b}$$

$$\tag{4.6c}$$

for attractant, and

$$\frac{dC_b}{dt} = \nabla \cdot (\mathbf{D}_b \nabla C_b)\,; \tag{4.7a}$$

$$\frac{d\mathbf{r}}{dt} = \mathbf{V}_f + \mathbf{V}_c; \tag{4.7b}$$

$$\tag{4.7c}$$

for bacteria, where C_a and C_b are the intrinsic average attractant and bacteria concentrations at Darcy's scale and $\mathbf{V}_f$ is the effective groundwater velocity. The terms $\mathbf{D}_a$ and $\mathbf{D}_b$ are the hydrodynamic dispersion tensor, which reads as:

$$\mathbf{D}_{\hat{i}\hat{j}} = (\alpha_T|\mathbf{v}| + D_m)\delta_{\hat{i}\hat{j}} + (\alpha_L - \alpha_T)\frac{v_{\hat{i}}v_{\hat{j}}}{|\mathbf{v}|} \tag{4.8}$$

Note that $\mathbf{V}_c$ if the effective chemotactic velocity at Darcy's scale that is different form the constitutive chemotactic velocity $\mathbf{v}_c$ at pore scale expressed by Eqn. (4.3). Originally *Long and Ford* [2009] quantify empirically $\mathbf{V}_c$ increasing of two order of magnitude the sensitive coefficient χ in order reproduce the observation in their experiments. Alternatively, *Valdés-Parada et al.* [2009a] derives the effective chemotactic velocity under particular assumptions on bacteria and attractant concentrations and on attractant gradients. In this case the effective chemotactic velocity results from the solutions of the governing equations at pore scale and of the closure problem associated to an elementary volume. The effective chemotactic velocity can be expressed by:

$$\mathbf{V}_c = \frac{2}{3}v_s tanh\left(\frac{\chi_0}{2v_s}\frac{k_d\|\nabla C_a\|}{(k_s + C_a)^2}\right)\frac{\nabla C_a}{\|\nabla C_a\|}\frac{\mathbf{D}_a}{\mathcal{D}_a}. \tag{4.9}$$

4.2 SPH formulation

The original SPH formulation for advection-diffusion equation has been proposed by *Español and Revenga* [2003] and then extended to passive solute transport in porous media in *Herrera et al.* [2009], which reads as:

$$\frac{dC_{a,i}}{dt} = \sum_{j=1}^{N}\frac{m_j}{\rho_i\rho_j}\left(\rho_i C_{a,i} - \rho_j C_{a,j}\right)\left(\mathbf{D}_{b,i} + \mathbf{D}_{b,j}\right)\frac{\mathbf{r}_{ij}}{\|\mathbf{r}_{ij}\|}\cdot\nabla W_{ij} \tag{4.10}$$

$$\frac{d\mathbf{r}_i}{dt} = \mathbf{v}_{f,i} \tag{4.11}$$

where the subscript i denotes the ith particle, m_i is the mass of ith particle and ρ_i is its density, which evolves in time according to relative particles positions as:

$$\rho_i = \sum_{j=1}^{N} m_j W_{ij}. \tag{4.12}$$

The term W_{ij} is the interpolating kernel function centered in $\mathbf{r}_i$ with respect to the location $\mathbf{r}_j$. As suggested by *Ferrari et al.* [2009], in this work we use the cubic B-spline which is defined as follows:

$$W_{ij} = \frac{\mathcal{C}}{h_{ij}^{\upsilon}} \begin{cases} 1/3 - q_{ij}^2 + q_{ij}^3/2 & \text{if } 0 \leq q_{ij} < 1 \\ (2 - q_{ij})^2 + q_{ij}^3 & \text{if } 1 \leq q_{ij} \leq 2 \\ 0 & \text{if } q_{ij} > 0 \end{cases} \tag{4.13}$$

where $q_{ij} = |r_j - r_i|/h_{ij}$, υ is the number of space dimension and $\mathcal{C}$ is the normalization constant so that $\int W_{ij} = 1$. The term h_{ij} is the so called smoothing length and it is locally variable:

$$h_{ij} = \frac{1}{2}\left(h_i + h_j\right), \qquad \text{with} \qquad h_i = \sigma \sqrt[\nu]{\frac{m_j}{\rho_j}} \tag{4.14}$$

Similarly the equation for bacteria including chemotaxis in SPH formalism reads as

$$\frac{dC_{b,i}}{dt} = \sum_{j=1}^{N} \frac{m_j}{\rho_i \rho_j} \left(\rho_i C_{b,i} - \rho_j C_{b,j}\right) \left(\mathbf{D}_{b,i} + \mathbf{D}_{b,j}\right) \frac{\mathbf{r}_{ij}}{\|\mathbf{r}_{ij}\|} \cdot \nabla W_{ij}, \tag{4.15}$$

$$\frac{d\mathbf{r}_i}{dt} = \mathbf{V}_{f,i} + \mathbf{V}_{c,i}. \tag{4.16}$$

This implies that in case of bacteria concentration each particle has two advection fields: the fluid and chemotactic velocity. On the other hand in case of attractant concentration the particles move only according to fluid velocity. This makes impossible the direct application of SPH. The only possibility would be to use two sets of particles: one for the attractant and one for the bacteria. In case of multiple bacteria species one should have a set of particles for each bacteria species due to different chemotactic response to attractant.

However, this raises two numerical issues. First, since the particles related to the bacteria and attractant are different and have different motion fields, they have different positions in the computational domain. This means that we need a scheme to transfer the attractant concentration information from the attractant particles to bacteria particles to compute the chemotactic velocity. For the same reason we have to compute the attractant gradient on the particles related to bacteria. Secondly, many particles related to bacteria would move to area where the attractant gradient and concentration are high. This means that some areas of the computational domain would not have particles related to bacteria making the SPH inapplicable. As point out by *Herrera et al.* [2009], the SPH requires particles even where solute concentration is zero to perform mass diffusion between interacting particles. This is the main difference between standard RWPT scheme.

Fig. 4.1 shows an illustrative example. We consider Gaussian concentration distribution of an attractant in an homogeneous flow field whose analytic solutions is known (Fig. 4.1a). On the same computational domain we set an equidistant distribution of particles which represents the particles carrying bacteria concentration information (4.1c). The analytical attractant concentration distribution allows to directly compute the attractant gradient and attractant gradient on each particles, i.e. the chemotactic flow field Fig. 4.1b . In order to simplify the computation we neglect the attractant diffusion. Both attractant and bacteria particles move according to the same flow field, and their relative positions does not change. This means that the contribution of advection due to the flow field can be neglected. However, the bacteria particle move also according to the chemotactic flow field directly computed on each particle. Fig. 4.1d shows the particle positions at the final time step. It is clear that we do not have enough particles in some domain areas to allows diffusion mass exchanged between particles. We underline that in this case the attractant concentration in known in each point of the computation domain as well its gradient. Table 4.1 shows the parameters used in this explicative example and they are taken from the work of *Long and Ford* [2009]. The chemotactic velocity is computed with the Eqns. (4.3) and increased by 35 per cent to amplify the chemotactic field effects on particles distribution decreasing the simulation time.

Parameter	Symbol	Value	Unit
Maximum attractant concentration	c_{a0}	$0.3e-4$	mg/L
–	w	0.06	$-$
Bacteria mean swimming velocity	$4.8e-3$	0.06	cm/s
Chemotactic receptor constant	$4.8e-3$	$1.25e-4$	M
Chemotactic sensitivity parameter	$2.4e-4$	$1.25e-4$	cm^2/s

Table 4.1: *Parameters for the explicative standard SPH test case.*

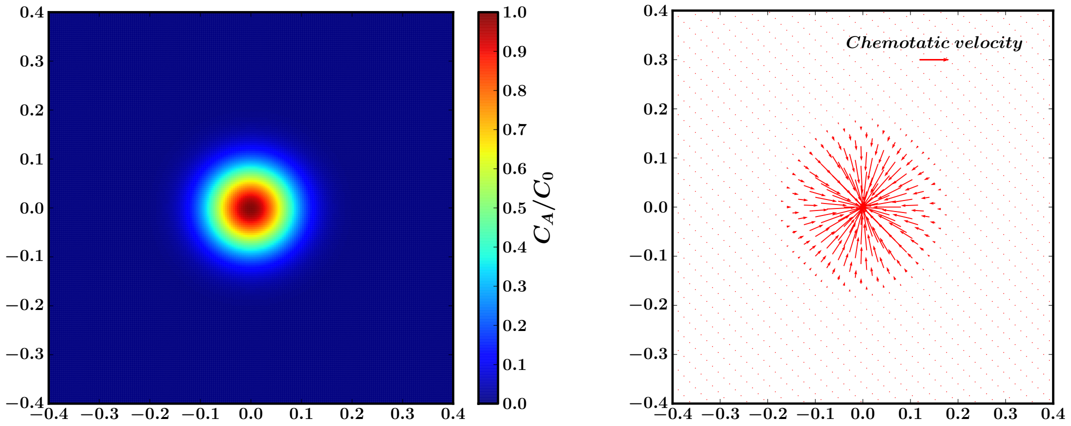

(a) *Attractant concentration.*

(b) *Chemotactic velocity field.*

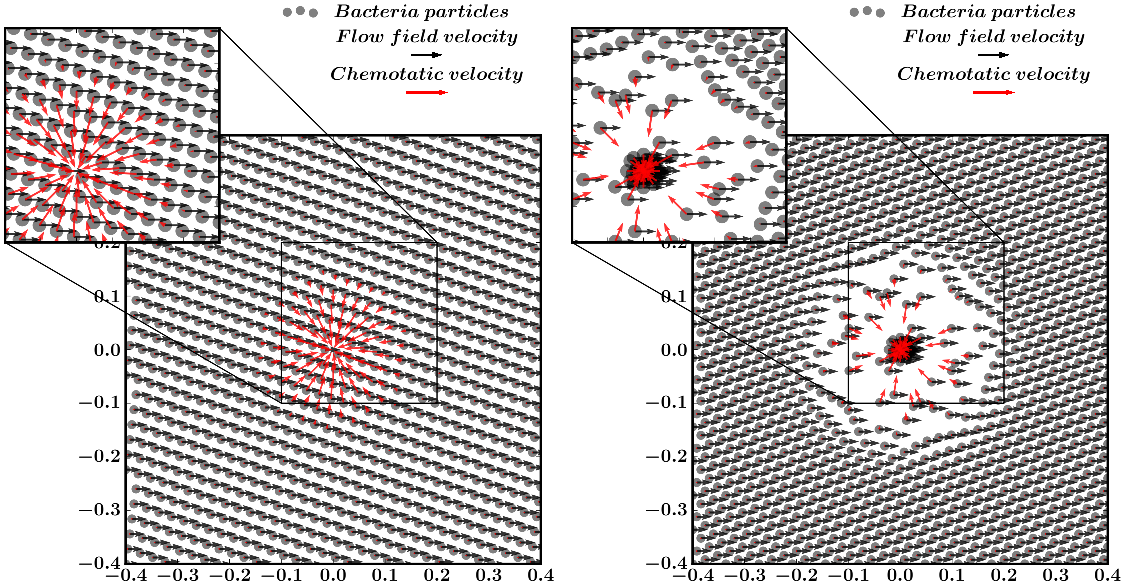

(c) *Bacteria concentration particles initial positions.*

(d) *Bacteria concentration particles final positions.*

Figure 4.1: *Standard SPH applied to chemotaxis, explicative test case.*

4.3 The new SPH approach

In attempt to have a SPH scheme but using only one set of particles, we propose the MWSPH developed by [*Avesani et al.*, 2014]. This alternative formulation of SPH derives from the work of *Vila* [1999] and *Ben Moussa et al.* [1999] and it uses high order Riemann solver to evaluate a numerical fluxes between each couple of interacting particles. Self similar to traditional mash-based scheme the chemotaxis can be expressed as a convective flux between each pair of interacting particles, but in a relative moving frame. As summarized in Fig. 4.2, particles move according to the flow field carrying both bacteria and attractant concentrations. For each particle we define high order reconstruction polynomials with a full meshfree scheme. The diffusive and chemotactic fluxes are then evaluated with the midpoint values between two interacting particles using a Riemann solver. We point it out that, known the attractant and attractant gradients at particle interfaces, the chemotactic velocity can be directly computed at the midpoint of the interpolating particles. This means that the kernel interpolation is not only used to model only the mass exchanged due to dispersion but also to take into account the chemotaxis. The use of the high order reconstruction polynomials together with the Riemann solver ensure the ability to capture the sharp bacteria concentration front which chemotactic velocity field forms.

As a result the more general advection-diffusion equation including chemotaxis can be rewritten as:

$$\frac{d}{dt}\mathbf{r} = \mathbf{v}_f, \tag{4.17}$$

$$\frac{d}{dt}\mathbf{Q} = \nabla\left(\mathbf{F}(\mathbf{Q},\nabla\mathbf{Q})\right), \tag{4.18}$$

where $\mathbf{Q} = (C_a, C_b)$ is the vector of the concentration and $\mathbf{F}(\mathbf{Q},\nabla\mathbf{Q})$ is the nonlinear flux vector, that depends on $\mathbf{Q}$ and on the gradient of $\mathbf{Q}$ in order to take into account both the diffusion effects and chemotactic advection, which reads as:

$$\mathbf{F}(\mathbf{Q},\nabla\mathbf{Q}) = \begin{bmatrix} -\mathbf{D}_a\nabla C_a \\ -\mathbf{D}_b\nabla C_b + \mathbf{V}_c C_b \end{bmatrix}; \tag{4.19}$$

As a consequence, the new MWSPH scheme including chemotaxis has the following form:

$$\frac{d(V\mathbf{Q})_i}{dt} = -\sum_{j=1}^{N} V_i V_j 2\mathbf{G}_{ij} \cdot \nabla W_{ij}, \tag{4.20}$$

$$\frac{dV_i}{dt} = \sum_{j=1}^{N} \left(\bar{\mathbf{v}}_{ij} - \mathbf{v}_{f,i}\right) \cdot \nabla W_{ij}, \tag{4.21}$$

$$\frac{d\mathbf{r}_i}{dt} = \mathbf{v}_{f,i}, \tag{4.22}$$

where $\mathbf{G}_{ij}$ is the numerical flux tensor. The term V_i is the particle volume, which evolves in time according to Eqn. (4.21) to take into account deformations due to velocity field [*Ferrari et al.*, 2009] and $\bar{\mathbf{v}}_{ij}$ is the velocity at the interface between the two interacting particles $\mathcal{P}_i$ and $\mathcal{P}_j$. Following *Avesani et al.* [2014], the numerical flux $\mathbf{G}_{ij}$ is solved using the Rusanov-type flux [*Dumbser et al.*, 2008a; *Dumbser*, 2010b] as

$$\mathbf{G}_{ij} = \frac{1}{2}\left(\mathbf{H}_i\left(\mathbf{Q}_{ij}^-, \nabla\mathbf{Q}_{ij}^-, \bar{\mathbf{v}}_{f,ij}\right) + \mathbf{H}_j\left(\mathbf{Q}_{ij}^+, \nabla\mathbf{Q}_{ij}^+, \bar{\mathbf{v}}_{f,ij}\right)\right) - \Theta\left(\mathbf{Q}_{ij}^+ - \mathbf{Q}_{ij}^-\right) \otimes \mathbf{n}_{ij}. \tag{4.23}$$

with

$$\bar{\mathbf{v}}_{f,ij} = \frac{1}{2}\left(\mathbf{v}_i^- + \mathbf{v}_j^+\right) \tag{4.24}$$

where $\mathbf{n}_{ij}$ the unitary vector of the distance particles $\mathcal{P}_i$ and $\mathcal{P}_j$ and $\mathbf{H}$ the flux tensor in the reference frame moving with velocity $\mathbf{v}_f$:

$$\mathbf{H}\left(\mathbf{Q}, \nabla\mathbf{Q}, \mathbf{v}_f\right) = \mathbf{F}\left(\mathbf{Q}, \nabla\mathbf{Q}\right) - \mathbf{Q} \otimes \mathbf{v}_f. \tag{4.25}$$

where the chemotactic velocity is computed from the extrapolated left and right states. The term Θ denotes the dissipation matrix [*Hidalgo and Dumbser*, 2011]:

$$\Theta = \left(\lambda_{ij} - \frac{1}{\|\mathbf{r}\|}\lambda_{\nu,ij}\right)\mathbf{I} \tag{4.26}$$

where λ_{ij} is the maximum absolute value of the eigenvalues of the Jacobian matrix of the convective part and $\lambda_{\nu,ij}$ is the maximum absolute value of the eigenvalues of the Jacobian matrix of the diffusive part of the flux evaluated in this case with respect to $\nabla\mathbf{Q}$. The dissipation matrix is evaluated both the along the direction $\mathbf{n}_{ij}$ in the moving frame with fluid velocity.

In the first case λ_{ij} reads as:

$$\lambda_{ij} = \max(|\Lambda_i^-|, |\Lambda_j^+|), \tag{4.27}$$

with Λ being the diagonal matrix of eigenvalues of $\mathbf{A_n}(\mathbf{Q}, \mathbf{v}) = \partial \mathbf{H}/\partial \mathbf{Q} \cdot \mathbf{n}_{ij}$. In the second $\lambda_{\nu,ij}$ is defined as:

$$\lambda_{\nu,ij} = \max(|\Lambda_{\nu,i}^-|, |\Lambda_{\nu,j}^+|), \tag{4.28}$$

with Λ_ν being the diagonal matrix of eigenvalues of $\mathbf{B_n}(\nabla\mathbf{Q}, \mathbf{v}) = \partial \mathbf{H}/\partial(\nabla\mathbf{Q}) \cdot \mathbf{n}_{ij}$. Furthermore, $\mathbf{Q}_{ij}^-$ and $\mathbf{Q}_{ij}^+$ are the left and right states at the midpoint of the two interacting particles obtained by the high order MLS-WENO reconstruction polynomials of degree M $\mathbf{Q}_i(\mathbf{r})$ for particle $\mathcal{P}_i$ and $\mathbf{Q}_j(\mathbf{r})$ for particle $\mathcal{P}_j$. For details of the MLS-WENO reconstruction we refer to Reference [*Avesani et al.*, 2014].

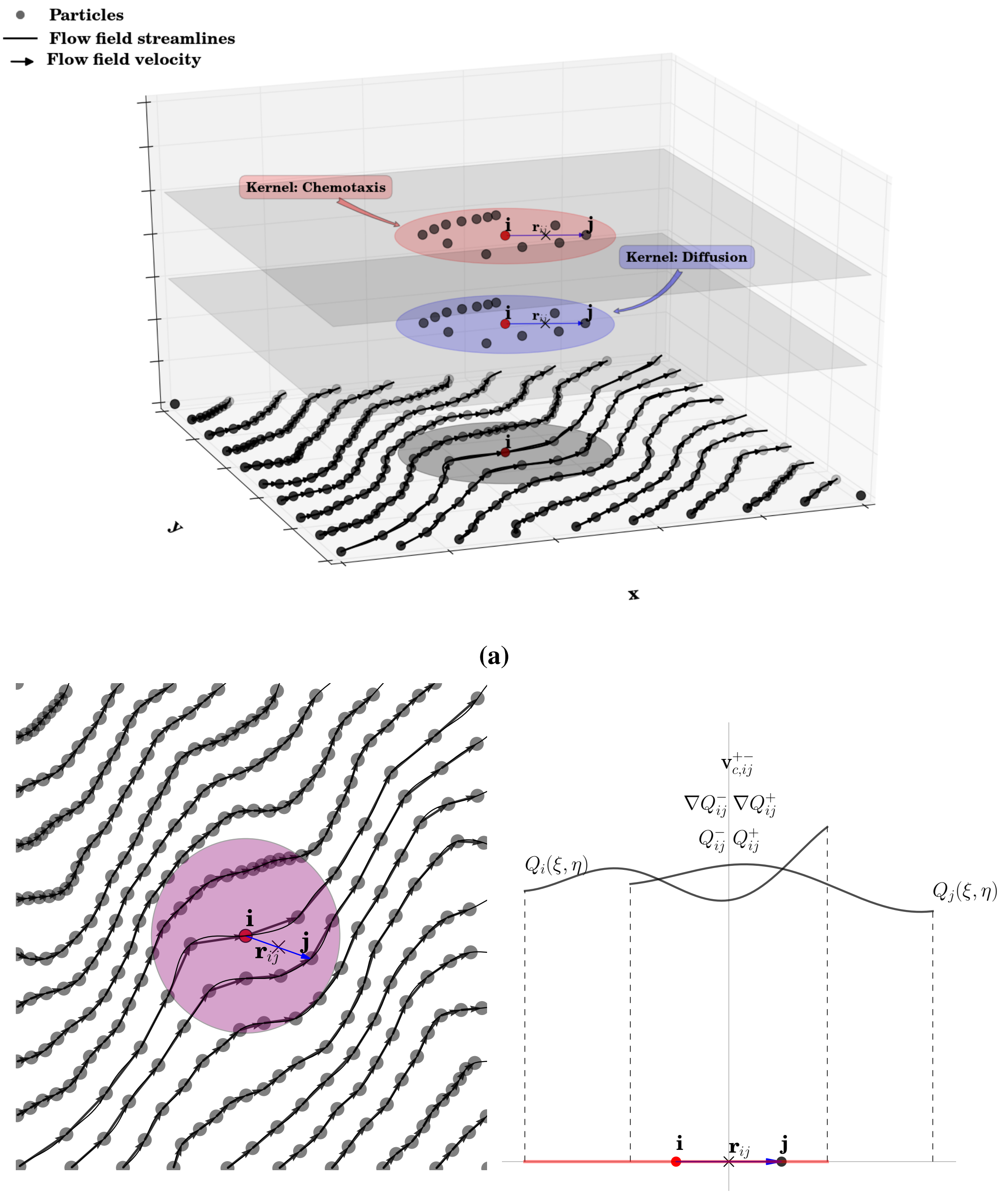

(a)

(b) **(c)**

Figure 4.2: *Meshless MWSPH method extended to chemotaxis. Particle move along instantaneous streamlines carrying both bacteria and attractant concentrations. They exchange solute mass with particles that are within its kernel support both for dispersion and chemotaxis. One dimension cut through the reconstruction polynomials along the line connecting particles* $\mathcal{P}_i$ *and* $\mathcal{P}_j$ *as well states* Q^-_{ij},∇Q^-_{ij}*and* Q^+_{ij},∇Q^+_{ij}*extrapolated to the midpoint and chemotactic velocity computed form the extrapolated states.*

4.4 Test cases

In this section some test cases are performed. These test cases have the aim to verify the accuracy and the robustness of the proposed numerical method in simulating chemotaxis in porous media. In the first subsection we study the one-dimensional problem while in the other subsections two dimensional problems are taken into account. In all test problems presented, the time step has been computed according to:

$$dt = CFL\frac{h_{ij}^{min}}{|\lambda_{ij}^{max}| + 2|\lambda_{\nu,ij}^{max}|/h_{ij}^{min}} \tag{4.29}$$

Following *Ferrari et al.* [2009]; *Avesani et al.* [2014], we implement an explicit third order Runge-Kutta scheme in time ensuring linear stability.

4.4.1 1D chemotaxis test case

This purely one dimensional test case has the aim to verify the accuracy of the MWSPH applied to chemotaxis. The positions of the particles are fixed during time evolution in Lagrangian coordinates while they are exchanging mass due to chemotaxis and diffusion. As a consequence, in this 1D test case particles do not move and the mathematical model for chemotactic bacterial-attractant system with reaction terms reads as:

$$\frac{\partial c_a}{\partial t} = \frac{D}{\tau}\frac{\partial^2 c_a}{\partial x^2} + r_s \tag{4.30}$$

$$\frac{\partial c_b}{\partial t} + \frac{1}{\tau}\frac{\partial}{\partial x}(v_c c_b) = \frac{\mu}{\tau}\frac{\partial^2 c_b}{\partial x^2} - Y r_s \tag{4.31}$$

where r_s is a Monod kinetics reaction model between the bacteria and the attractant:

$$r_s = -q\frac{c_a}{c_a + k_s}c_b, \tag{4.32}$$

which represents the rate of attractant consumption and the rate of bacteria growth. Here the term q is the maximum reaction rate between the bacteria and the attractant, k_s is the half saturation constant, μ is the random motility coefficient of the bacteria, τ is the tortuosity of the porous media, D is the diffusion coefficient of the attractant and Y is the yield coefficient. The reader can find more theoretical details of model (4.30-4.31) in *Alt*

[1980]; *Erban et al.* [2004]; *Ford and Harvey* [2007a].

We use the anlytical solution proposed by *Long and Hilpert* [2007] to validate the numerical scheme. This analytic solution is a more general formulation of the original one derived by *Keller and Segel* [1971a] which reads as:

$$\frac{c_b}{c_{b0}} = \left(\frac{c_b}{c_{b0}}\right)^{\lambda} \exp\left(-\frac{\tau c}{\mu}(x-ct)\right) \tag{4.33}$$

$$\mathcal{F}\left(\frac{c_a}{c_{a0}}\right) - \mathcal{F}(1) = \frac{c_{b0} q \mu}{\tau c^2 c_{a0}} \exp\left(-\frac{\tau c}{\mu}(x-ct)\right) \tag{4.34}$$

with

$$\mathcal{F}(X) = \frac{X^{1-\lambda}}{\lambda-1} + \frac{k_s}{c_{a0}}\frac{X^{-\lambda}}{\lambda} \tag{4.35}$$

under the following assumptions:

1. the bacteria diffusion is null ($D=0$);
2. the bacterial growth and death is neglected ($Y=0$);
3. the attractant concentration for large positive x equals c_{b0};
4. the bacteria concentration for large negative x is null;
5. The attractant concentration gradient is null for both large positive and negative x ($\partial c_a(x=\pm\infty)/\partial x = 0$);

In this case the chemotactic velocity is defined as:

$$v_c = \frac{\chi_0 k_s}{3c_a}\frac{\partial c_a}{\partial x} \tag{4.36}$$

The main difference between the original formulation proposed by *Keller and Segel* [1971a] and the one developed by *Long and Hilpert* [2007] is that the attractant availability is limited. The analytic solution represents the one dimensional bacterial and attractant concentration bands that travel with constant speed c through space and whose shape does not change in time. The expression is obtained setting the parameters such that $\frac{c_{b_0} q \mu}{\tau c^2 \lambda} = 1$.

Fig. 4.3 shows the numerical results computed with the MWSPH scheme on 400 particles for different time steps. The parameters used in the numerical experiment are reported in the Table 4.2 and they are taken form *Pedit et al.* [2002]. The reactive term is solved with an implicit Newton-Raphson scheme [*Press et al.*, 1992]. The agreement between numerical and reference solution is excellent. The numerical solutions move without changing shape or underestimating the maximum concentrations.

Parameter	Symbol	Value	Unit
Initial bacteria concentration	c_{b0}	$4.9e+9$	cfu/l
Initial attractant concentration	c_{a0}	$2.83e-3$	mg/L
Diffusion coefficient (attractant)	D	$7.5e-10$	m^2/s
Mobility	μ	$3.2e-11$	m^2/s
Maximum rate of attractant consumption	q	$7.9e-16$	$g/cfu/s$
Yield coefficient	Y	0	$g/cfu/s$
Dissociation constant	k_d	$2.1e-3$	g/l
Half saturation constant	k_s	$1.3e-4$	g/l
Chemotactic sensitivity coefficient	χ	$1.8e-9$	m^2/s
Swimming speed	ν	48	$\mu m/s$

Table 4.2: *Parameters for one-dimensional test case.*

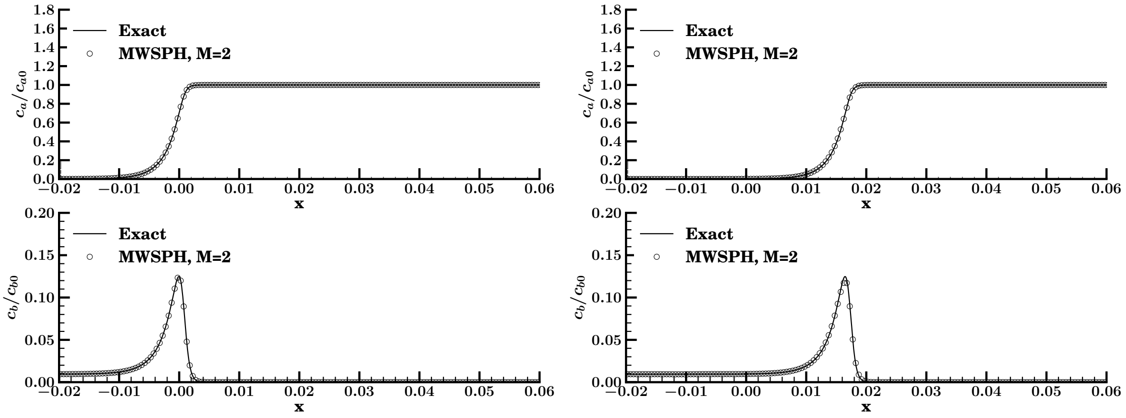

(a) $time = 0\ \frac{tv_s}{l_0}$ **(b)** $time = 4.57e-5\ \frac{tv_s}{l_0}$

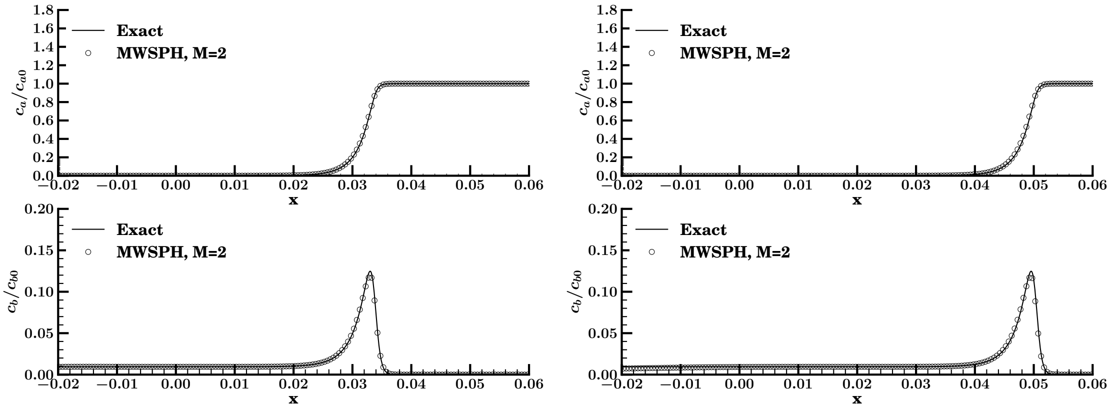

(c) $time = 9.14e-5\ \frac{tv_s}{l_0}$ **(d)** $time = 1.37e-4\ \frac{tv_s}{l_0}$

Figure 4.3: *Numerical solution for one dimensional test case at different time step,* $CLF = 0.8$ $\sigma = 2$ *and* $M = 2$.

4.4.2 2D diffusion chemotaxis

In this test case we consider an instantaneous release of both bacteria and attractant solutes in an homogeneous flow field with velocity v_0 with orientation of 30^o with respect to *x-axis*. The initial concentrations are given by:

$$C_i = \frac{C_1}{C_4} exp\left(\frac{-(x-x_0)^2 w^2 - (y-y_0)^2 w^2}{2w^4}\right) \tag{4.37}$$

where C_i is the species taken into account with $C_1 = C_0 w^2$, $C_2 = D_{\hat{i}\hat{i}} D_{\hat{j}\hat{j}} - 4D^2_{\hat{j}\hat{i}}$, $C_3 = D_{\hat{i}\hat{i}} + D_{\hat{j}\hat{j}}$ and $C_4 = w^2$. Table 4.3 reports the numerical test case parameters and Fig. 4.4 shows the initial concentration for both attractant and bacteria. The two plumes are slightly overlapping to enable the bacteria chemotaxis. The attractant and bacteria parameters refer to Reference [*Long and Ford*, 2009].

Parameter	Attractant	Bacteria
Maximum initial concentration	$c_{a0} = 0.3e-4(mg/l)$	$c_{b0} = 1$
w	0.04	0.04
Initial plume maximum position	$x_0 = -0.05$, $y_0 = 0$	$x_0 = +0.05$, $y_0 = 0$
Longitudinal dispersion	$\alpha_L = 0.04$	$\alpha_L = 0.008$
Transversal dispersion dispersion	$\alpha_T = 0.004$	$\alpha_T = 0.0008$
Flow field velocity	$v_0 = 1.e-3cm/s$	
Flow field orientation	$\beta = 30^o$	
l_0	$l_0 = w$	

Table 4.3: *Parameters for two dimensional diffusion test case.*

Fig. 4.5 reports the numerical solution of bacteria transport at simulation time $T = 3.76$, with T the dimensionless time defined as $T = tv_0/l_0$. The contribution of chemotaxis is clear. The chemotactic bacteria move where the attractant concentration and attractant gradients are higher. The concentration aligns with the velocity field. The same behavior can be noticed in case of bacteria without the contribution of chemotaxis. Because of the presence of attractant, there is a chemotactic advective field that effects the bacteria transport. It can be notice that the chemotactic flow field is directed according to the attractant gradient. As a consequence, in case of chemotaxis, the bacteria move to the center of the attractant plume where the attractant gradient is null and where we have the maximum of attractant concentration.

Fig. 4.6 shows the snapshots of the numerical solution of the MWSPH extended to

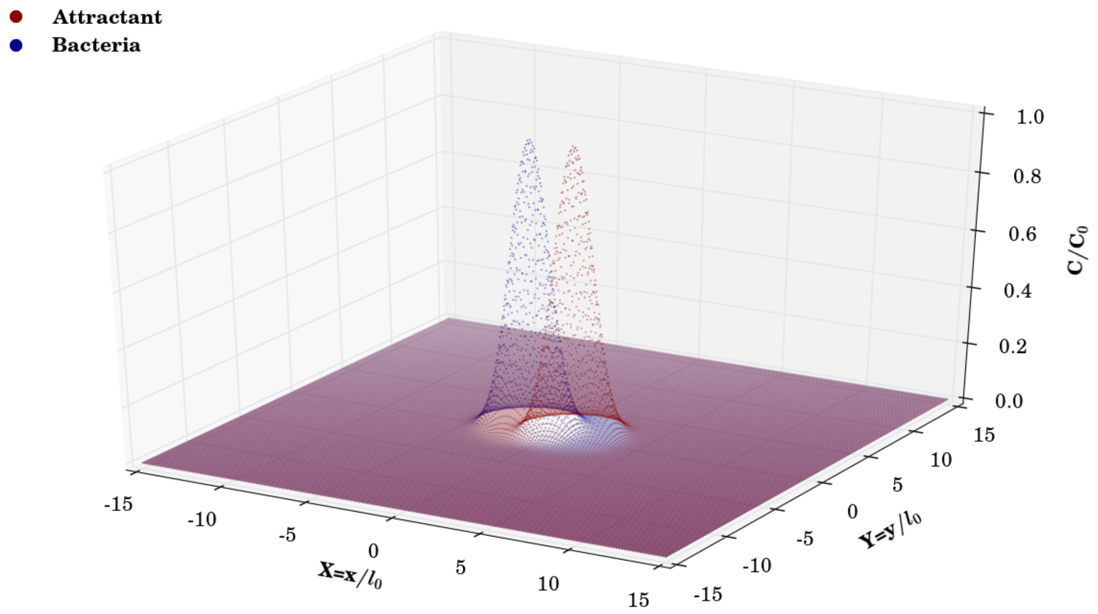

Figure 4.4: *Diffusion test case, initial concentration for attractant and bacteria.*

chemotaxis transport at different time steps. The chemotaxis not only causes an asymmetric shift of the plume of bacteria but also it reduces the contribution of the diffusion to bacteria transport. Bacteria concentration at section x at different time steps.

Fig. 4.6 shows the time evolution of bacteria concentration at section x to better assess the contribution of chemotaxis. The section x is located at $y = 0$ along x-axis (Fig. 4.6b). The bacteria concentration without the contribution of chemotaxis are also included in order to underline the chemotactic bacteria response to attractant. The reader can notice mainly two effects of chemotaxis on bacteria transport. First, the chemotaxis reduces the bacteria diffusion: the maximum bacteria concentration is higher when chemotaxis is taken in account. Secondly, we have an asymmetric response of bacteria plume in case of chemotaxis while the bacteria plume without the contribution of chemotaxis maintain its original symmetry. The bacteria are developing self sharpening front as already shown in experimental observations.

(a) *Attractant concentration and chemotactic velocity field generated.*

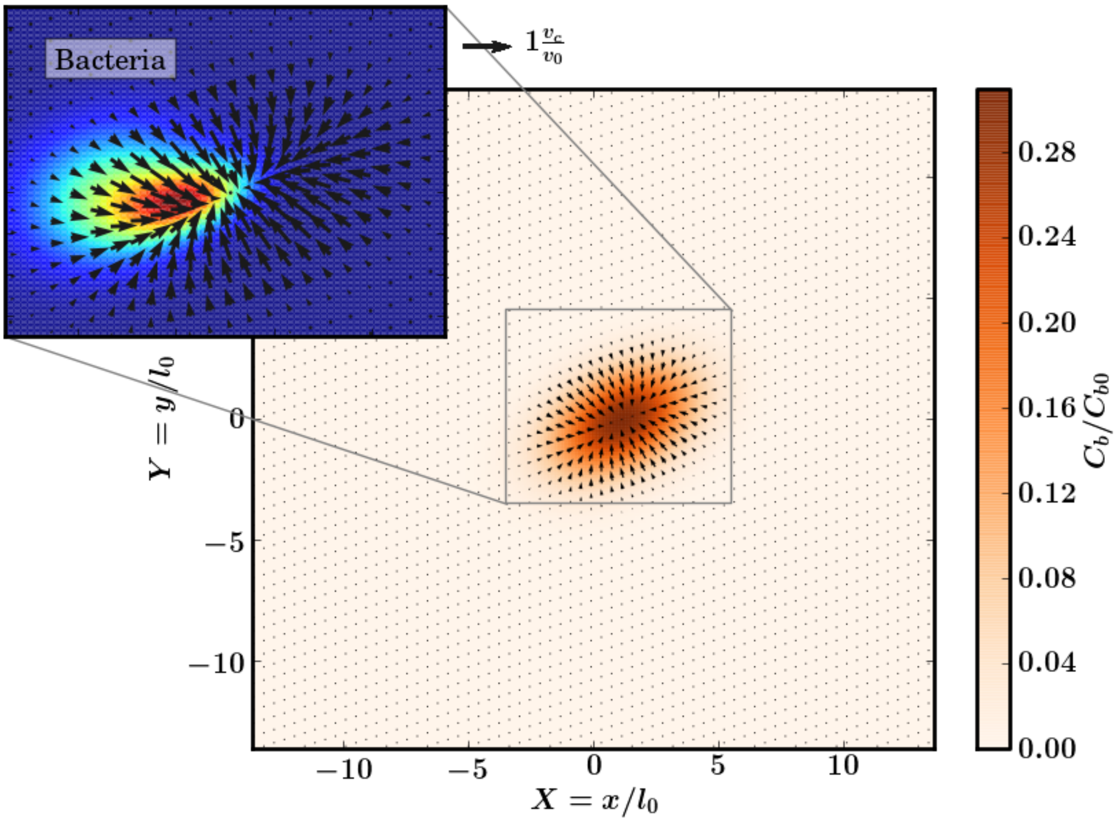

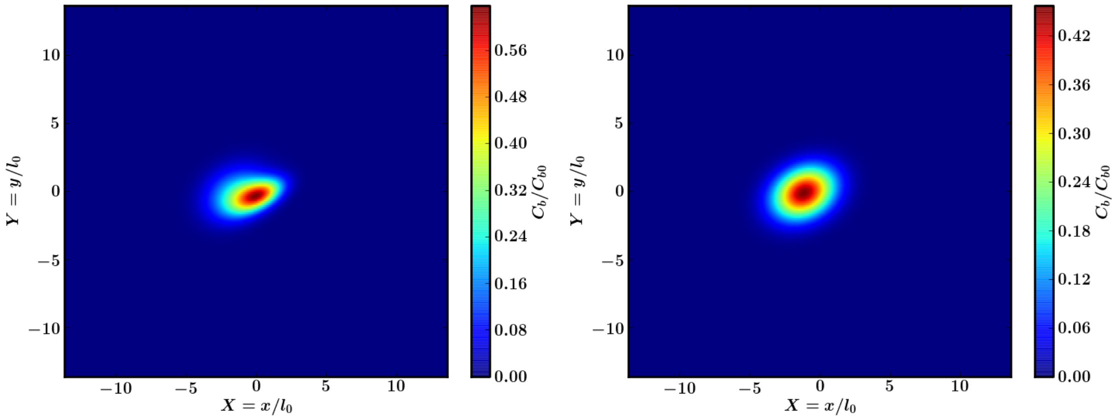

(b) *Bacteria with chemotaxis.* **(c)** *Bacteria without chemotaxis.*

Figure 4.5: *Numeral results for diffusion test case at time* $T = 3.76$, $CFL = 0.9$, $\sigma = 3$, $\sigma_{mls} = 4$. *Attractant concentration and chemotactic velocity field, bacteria concentration with or without the chemotactic.*

(a) *Time evolution of bacteria and attractant concentration in section x.*

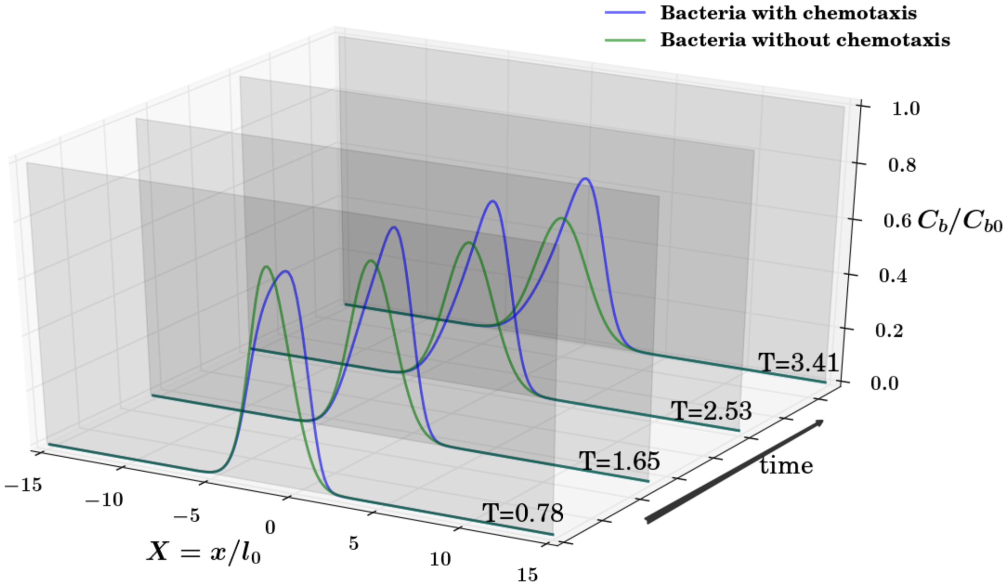

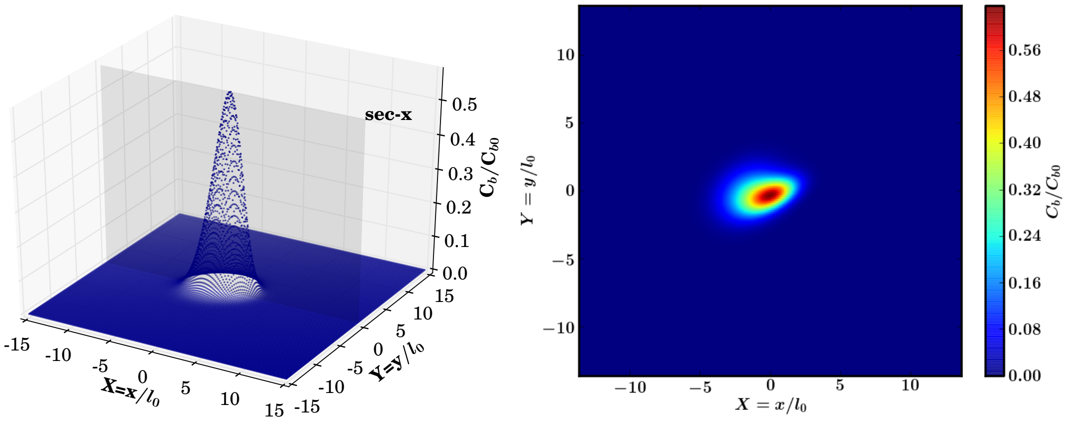

(b) *Bacteria concentrations and section x.*

(c) *Bacteria concentration plane view.*

Figure 4.6: *Numeral results for diffusion test case,* $CFL = 0.9$, $\sigma = 3$, $\sigma_{mls} = 4$. *Bacteria concentration and snapshots at different time steps at section* $sec - x$ *for bacteria with or without chemotaxis.*

4.4.3 2D advection-diffusion chemotaxis

This numerical experiment is intended to illustrate how both chemotactic advection field and advection flow field are solved simultaneously with the MWSPH in the more general SPH framework. Fig. 4.7 shows the numerical experiment set-up to simulate layers of porous media with different conductivities: a inner part with a higher permeability k_1 and and two external parts with lower permeability k_2. Because of the different permeability the layers have also different velocity V_1 and V_2. The inner part has a width w. We use the same experimental set-up given by *Wang and Ford* [2009] for the computational domain and flow field which are reported in Table 4.4. The attractant is placed at $2 \leq x \leq 10$ along the central $x-axis$ to mimic a contaminant trapped in an aquifer. The initial attractant concentration is defined as:

$$C_a = C_{a0}\frac{1}{2}\left(erfc\left(\frac{(y-y_0)-w}{4\mathcal{D}_a t^i}\right) - erfc\left(\frac{(y-y_0)+w}{4\mathcal{D}_a t^i}\right)\right) \tag{4.38}$$

A pulse of bacteria is then uniformly injected with constant concentration C_b at $1.5 \leq x \leq 3.5$ along the $y-axis$.

The computational domain is defined as $[0, L_x] \times [0, L_y]$ and we use 150×200 particles equispaced on a regular lattice $[0, L_x^1] \times [0, L_y]$. We point out that the particles are deleted or added during the simulation following the motion of the fluid. Basically the particles in the inner part are removed from the downstream and added again at upstream to ensure the buffer zone to the plumes which allows the bacteria and attractant dispersion. This limits the total number of required particles for numerical simulation, it decreases the total computational time. According to the initial conditions set up, the attractant produces a chemotactic advective field that effects the bacteria transport (Fig. 4.7b).

Fig. 4.8 shows the attractant and bacteria concentrations at time $1225s$ after 150 time steps. The heterogeneous flow conditions split the bacteria plume in two part: the inner part, that moves downstream together with the attractant, and the outer part, that moves slowly. Part of bacteria moves to the center of the plumes for the presence of chemotactic flow field. This produces a peak in bacteria concentration located at the center of the plume. This implies that a large portion of bacteria has migrated to the inner part of the flow field according to the chemotactic velocity generated by the attractant and perpendicular to the main flow direction. Furthermore, Fig. 4.9 underlines the contribution of chemotactic to bacteria transport. We consider the bacteria concentration with or without the contribution

Parameter	Attractant	Bacteria
Maximum initial concentration	$c_{a0} = 0.3e-4(mg/l)$	$c_{a0} = 1$
w	0.04	0.04
Initial plume maximum position	$x_0 = -0.05$, $y_0 = 0$	$x_0 = +0.05$, $y_0 = 0$
Longitudinal dispersion	$\alpha_L = 0.004\ (cm)$	$\alpha_L = 0.0008\ (cm)$
Transversal dispersion dispersion	$\alpha_T = 0.0004\ (cm)$	$\alpha_T = 0.00008\ (cm)$
Initial diffusion time for the attractant	$t^i\ (1200s)$	–
Chemotactic response parameter		
Bacteria mean swimming velocity v_s	$4.8e-3$	(cm/s)
Chemotatic receptor constant k_d	$1.25e-4$	(M)
Chemotatic sensitivity χ_0	$8.0e-4$	(cm^2/s)
Flow field		
Internal velocity V_1	0.0087	(cm/s)
External velocity V_2	0.00202	(cm/s)

Table 4.4: *The parameters for advection-diffusion-chemotaxis test case.*

of chemotaxis at section y located at bacteria plume peak. In case of chemotaxis the maximum bacteria concentration becomes twice the maximum bacteria concentration when chemotaxis is not taken into account.

The effectiveness of chemotaxis is quantified with the dilution index and with the dissipation rate. The dilution quantifies the volume occupied by the solute [*Kitanidis*, 1994] and the dissipation rate quantifies the mixing rate [*Le Borgne et al.*, 2010]. Fig. 4.10 reports the dissipation rate and the dilution index for bacteria with or without the contribution of chemotaxis. The reader can notice that chemotaxis leads to lower dissipation rate. This means that the bacteria plume spreads in a more narrow region. On the other hand, the dissipation rate is higher because of the contribution of chemotaxis. This clearly means that in case of bacteria reactive transport the chemotaxis potentially increases the biodegradation of the attractant.

(a) *Numerical experiment set-up: initial concentrations and flow field.*

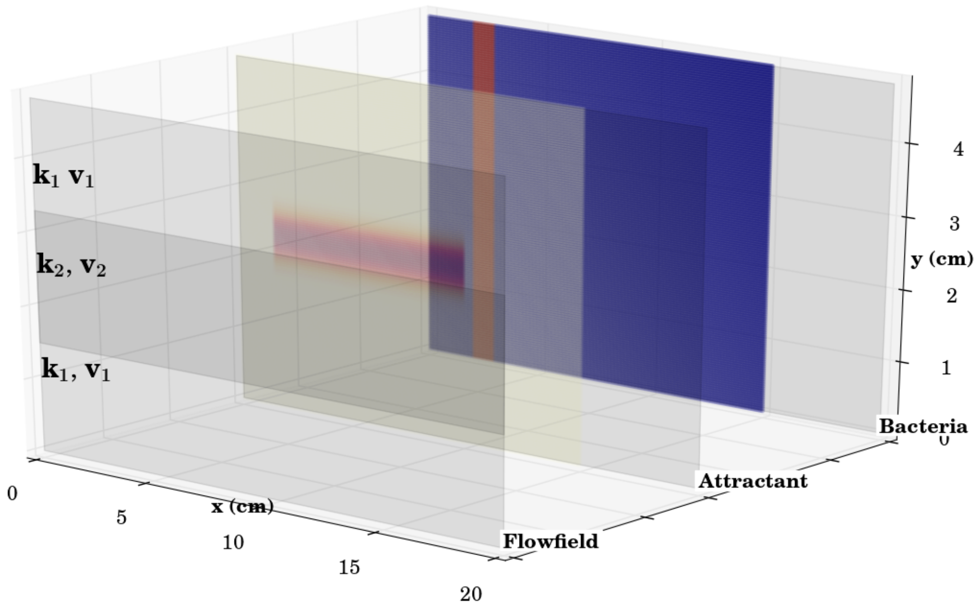

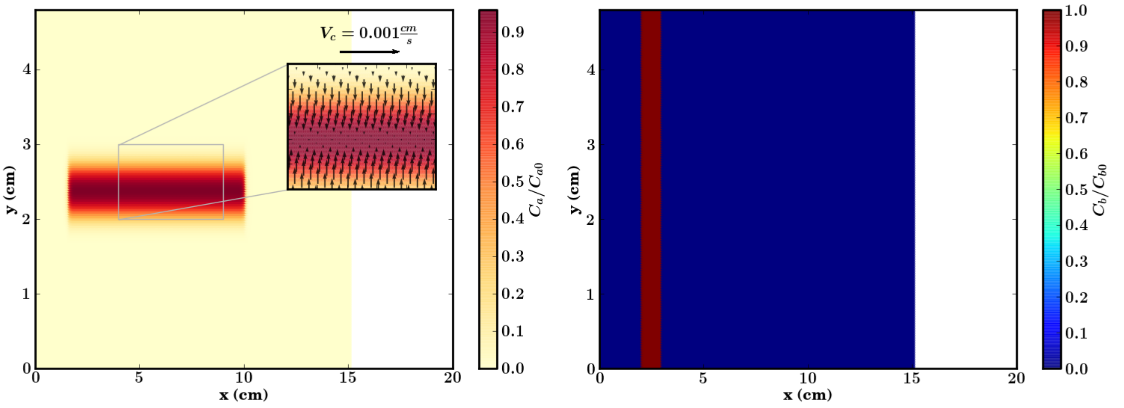

(b) *Initial condition attractant and chemotatic velocity field.*

(c) *Initial condition bacteria.*

Figure 4.7: *Dual layers numerical set up,* 250×150 *particles* $CFL = 0.9$, $\sigma = 3$ *and* $\sigma_{mls} = 4$.

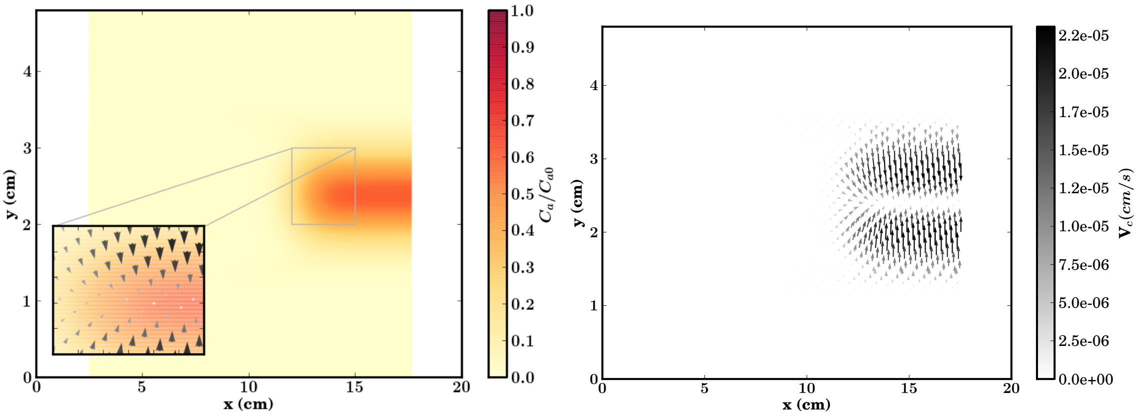

(a) *Attractant concentration.* **(b)** *Chemotactic velocity field.*

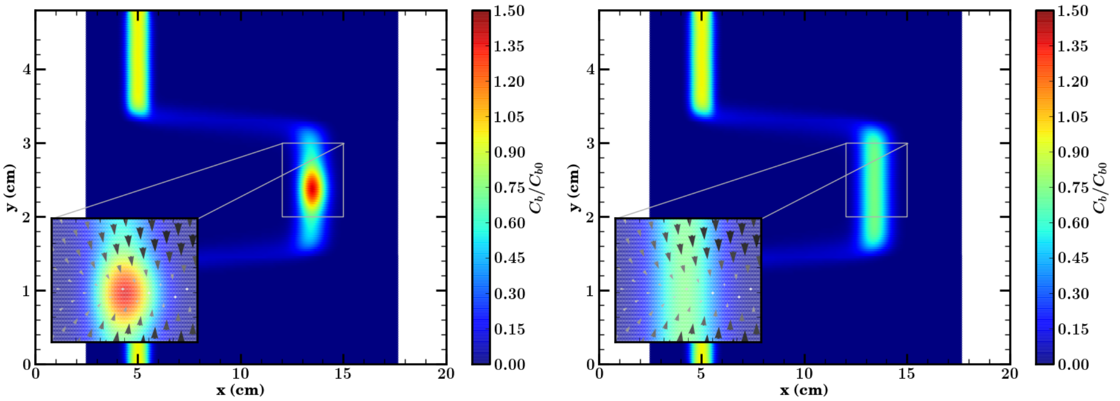

(c) *Bacteria with chemotaxis.* **(d)** *Bacteria without chemotaxis.*

Figure 4.8: *Numerical results for advection-diffusion-chemotactic test case,* $CFL = 9$, $\sigma = 3$, $\sigma_{mls} = 4$.

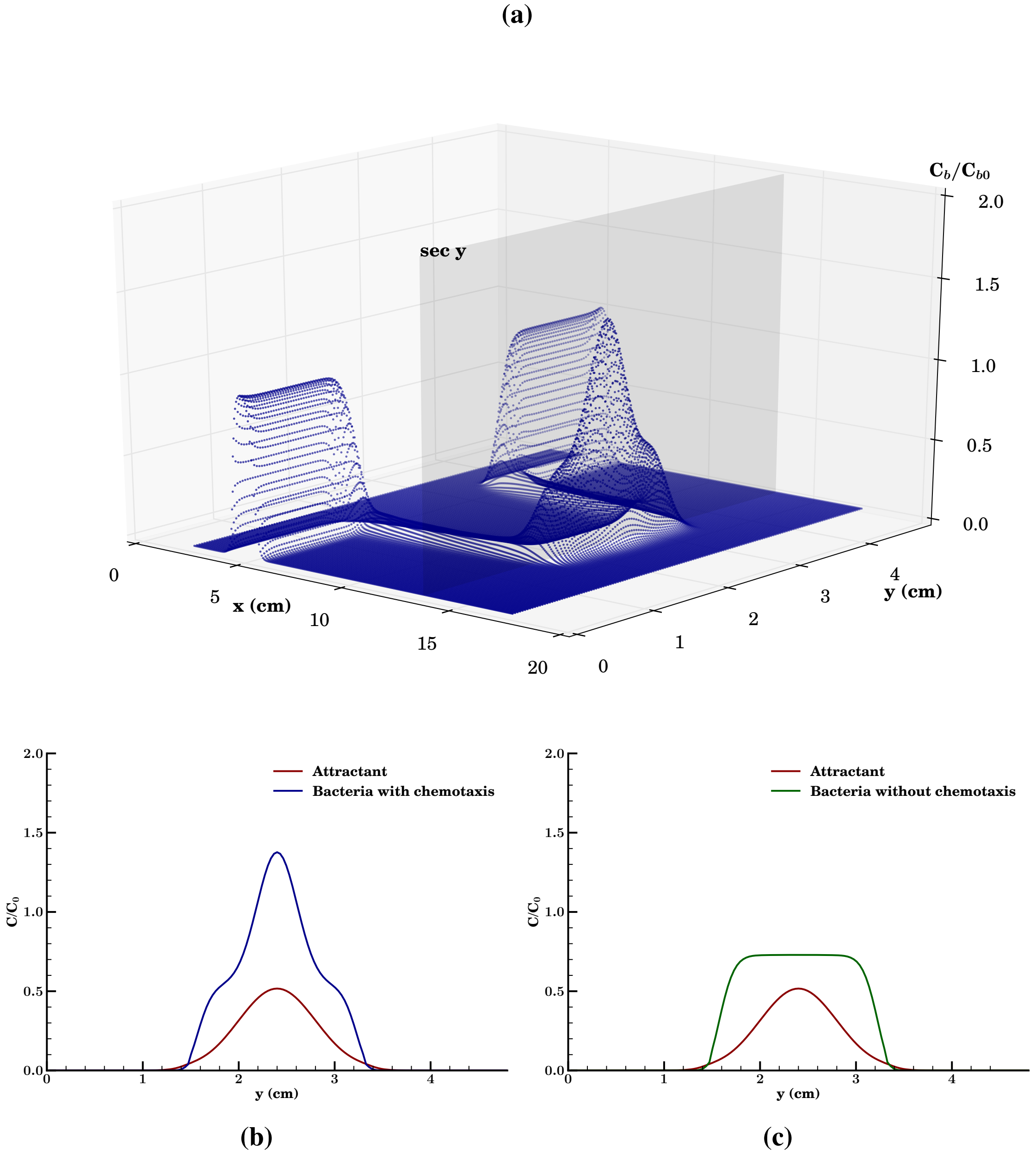

Figure 4.9: *Dual layers numerical results for bacteria concentration at time* $1225s$*,* 250×150 *particles* $CFL = 0.9$*,* $\sigma = 3$ *and* $\sigma_{mls} = 4$*.*

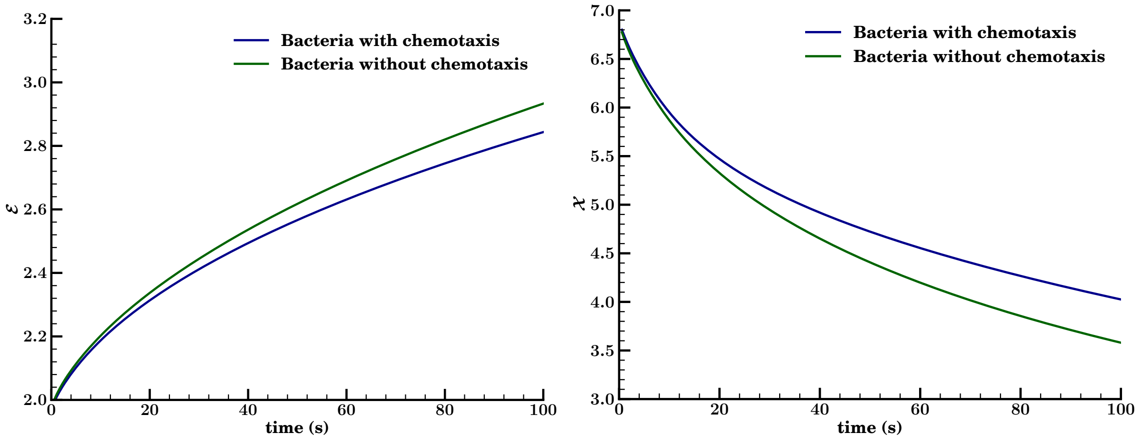

(a) *Dilution index.* **(b)** *Dissipation rate.*

Figure 4.10: *Dissipation rate and dilution index for bacteria with or without the contribution of chemotaxis.*

4.4.3.1 2D advection-diffusion chemotaxis, case 2

In this section, we consider the same initial condition and set-up of the the numerical example shown in section 4.4.3 but with some differences in the flow field and in the initial condition for the attractant concentration. On the contrary of the first test case, we set the inner part with lower permeability k_1 and the outer part with higher permeability k_2. Secondly, the initial diffusion time t_i (Eqn. 4.38) for the attractant is reduced to $80s$ in order to increase the initial attractant gradient and the bacteria chemotactic response. In particular, Fig. 4.11a reports the numerical solution of bacteria concentration at different time step in order to analyze the temporal evolution of bacteria concentration. At initial time step, section y is located along $y-axis$ at the center of bacteria plume and it moves downstream according to velocity fields V_1. As in the test case analyzed in section 4.4.3, the bacteria plumes split in two part: a inner part that moves slowly and a outer part that moves faster. Because of the initial higher gradient of the attractant, the chemotatic bacteria response is more evident. The bacteria produce multiple peaks that increase in time and move to the inner part of attractant plume. The peaks represent the bacterial bands which move according to the chemotactic advective field. This bacterial bands have been already observed in many experimental works [*Keller and Segel*, 1971a; *Rivero et al.*, 1989; *Wang and Ford*, 2009] and here simulated numerically.

(a) *Snapshot of section y in time.*

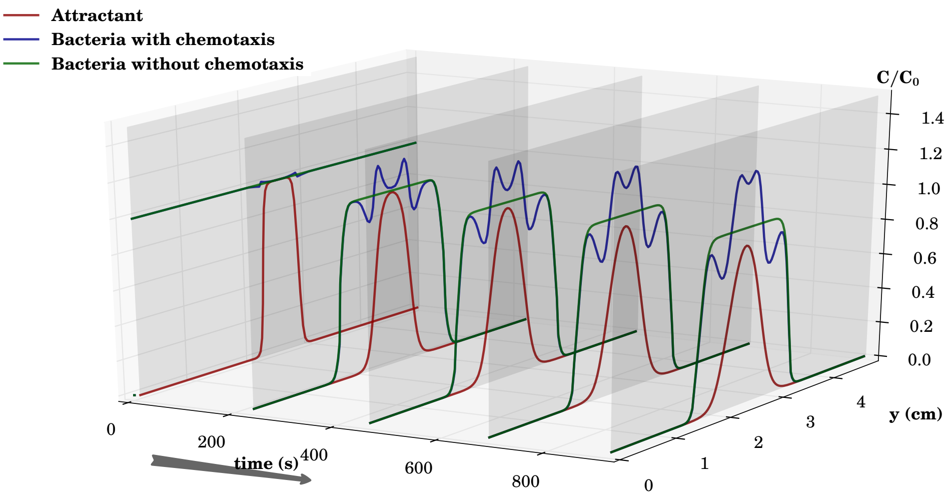

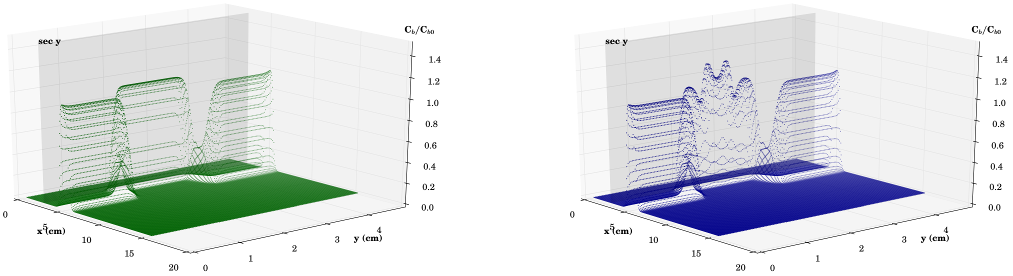

(b) *Bacteria without chemotaxis.* **(c)** *Bacteria with chemotaxis.*

Figure 4.11: *Numerical results for advection-diffusion-chemotactic with intruction test case,* $CFL = 0.9$, $\sigma = 3$, $\sigma_{mls} = 4$.

4.5 Conclusion

In this work we have proposed an alternative formulation of SPH method for the numerical solutions of chemotactic bacteria transport in porous media based on the MWSPH. This scheme takes advantage of the SPH method characteristics in the simulation of solute transport in porous media overcoming its limits for modeling bacteria transport with chemotaxis. As standard SPH scheme is a fully particles method where particles move according the flow field and a kernel interpolation models the mass exchanged between particles due to diffusion. We have show through numerical example that standard SPH can not handle multiple advective fields like in case of chemotaxis. On the other hand MWSPH provides a robust mechanism to incorporate chemotaxis in the SPH.

The MWSPH method combines flux evaluation with high order truly meshfree Moving-Least-Squares WENO polynomial reconstruction. This allows to use only one set of particles that move according to the flow field, and to model the chemotaxis as an advective flux between interacting particles in a relative moving frame. Moreover, the Moving-Least-Squares-WENO reconstruction leads to high order solute gradient concentration evaluations, which is a fundamental characteristic for the assessment of chemotatic velocity. Unlike standard SPH scheme, Moving-Least-Squares-WENO reconstruction is not sensible to particles position and it can reach arbitrary order of accuracy.

We test the new scheme against reference solutions. We present also numerical example to show its applicability for modeling chemotaxis in porous media. The scheme is able to reproduce correctly the bacteria transport in porous media with chemotaxis and to reproduce bacteria band patterns when the physical parameters are proper. The numerical solutions do not show unphysical oscillations and the scheme is stable under CFL conditions.

5 Conclusion

The focus of the research activity has been on a new formulation of the Smoothed Particle Hydrodynamics (SPH) method and its application to solute and microbial transport in porous media. This new formulation has been developed specifically to deal with self sharpening fronts, such as those developing in the transport of cells, bacteria or multicellular organisms capable to develop autonomous motility in the direction of a chemical concentration gradient (attractants) either toward or away from the chemical stimulus. The ability of these organisms to move along the concentration gradients of an attractant is called chemotaxis.

Existing studies suggest that bacteria forms traveling bands reaching velocity comparable to groundwater flow velocity. Experimental and theoretical studies indicated chemotaxis as an important mechanism in a variety of subsurface processes, in addition to its crucial role in biology. In order to obtain an accurate representation of chemotaxis at the continuum scale we propose a new numerical scheme to model advective transport in porous media with anisotropic dispersion which is based on a modification of the standard Smoothing Particle Hydrodynamics method (SPH). The work can be divided up into three parts.

In the first part we develop a new SPH scheme based on Ben Moussa & Vila' s SPH formulation and WENO reconstruction technique. The key idea is to produces a high order accurate reconstruction of the solution using WENO and then evaluate the fluxes at particle interfaces with a Riemann solver. Firstly, we extended WENO originally developed in a Eulerian framework, to a mesh-free Lagrangian framework. We tested two Riemann solvers: the Rusanov flux and the Osher Flux. The use of monotone fluxes together with WENO ensure stability and non oscillations in the solutions i.e. no artificial viscosity term is required. We validate the new scheme with a well known test case: two-dimensional Sod's problem. We emphasize that the solution of the inviscid flow problem is an appropriate test case providing both shock and rarefaction waves. We call this new scheme MWSPH, because it is the combination of the Moving Least Square and WENO within the more general formulation of the Vila & Ben Moussa's SPH.

In the second part we focus on the advection-diffusion equation in heterogeneous porous media. A typical property of most numerical schemes applied to solve the advection-diffusion equation is the intrinsic numerical diffusion. This implies low accuracy when advection dominates diffusion, as occurs in most application to natural heterigeneous media, or leads to unphysical oscillations and negative concentrations in presence of anisotropic diffusion. We extend the MWSPH to approximate advection-diffusion equations with anisotropic diffusion tensor. We demonstrate that the MWSPH, is stable and accurate and that it reduces the occurrence of negative concentrations. When negative concentrations are observed, their absolute values are several order of magnitude smaller compared to standard SPH. Another appreciable characteristic of the new scheme is that it limits spurious oscillations in the numerical solution more effectively than standard SPH. We test the accuracy and the essentially non oscillatory behavior of the MWSPH scheme with a numerical convergence study and by evaluating the range of concentrations obtained with the new scheme for different ratios of anisotropy of the diffusion tensor.

The MWSPH is finally applied to chemotaxis in porous media. The chemotaxis advection flux is solved in the particle moving frame. This means that only one set of particles is used, both for microorganisms and passive solute. The test cases show that this new numerical scheme is mass conservative and with low numerical diffusion, such that it can be used to accurately assess the nonlinear interplay between local dispersion and chemotaxis in porous formations.

Bibliography

Abel, T., rpSPH: A novel smoothed particle hydrodynamics algorithm, *Monthly Notices of the Royal Astronomical Society*, *413*, 271–285, 2011. (cited at page: 13)

Aboiyar, T., E. H. Georgoulis, and A. Iske, Adaptive ader methods using kernel-based polyharmonic spline weno reconstruction, *SIAM J. Sci. Comput.*, *32*, 3251–3277, 2010. (cited at page: 61)

Adami, S., X. Hu, and N. Adams, A conservative {SPH} method for surfactant dynamics, *Journal of Computational Physics*, *229*, 1909 – 1926, 2010a. (cited at pages: 11 and 12)

Adami, S., X. Hu, and N. Adams, A new surface-tension formulation for multi-phase {SPH} using a reproducing divergence approximation, *Journal of Computational Physics*, *229*, 5011 – 5021, 2010b. (cited at page: 11)

Adami, S., X. Hu, and N. Adams, A transport-velocity formulation for smoothed particle hydrodynamics, *Journal of Computational Physics*, *241*, 292 – 307, 2013. (cited at page: 12)

Agossler Albert, A., Moving least-squares: A numerical differentiation method for irregularly spaced calculation points, *Technical report*, Sandia National Labs., 2001. (cited at pages: 24, 69, and 70)

Alt, W., Biased random walk models for chemotaxis and related diffusion approximations., *Journal of Mathematical Biology*, *9*, 147–177, 1980. (cited at pages: 99 and 112)

Aristodemo, F., I. Federico, P. Veltri, and A. Panizzo, Two-phase sph modelling of advective diffusion processes, *Environmental Fluid Mechanics*, *10*, 451–470, 2010. (cited at page: 63)

Avesani, D., M. Dumbser, and A. Bellin, A new class of moving least squares weno-sph schemes, 2014, under review in Journal of Computational Physics. (cited at pages: 64, 66, 67, 100, 108, 109, 110, and 112)

Balsara, D. S., von neumann stability analysis of smoothed particle hydrodynamicsâsuggestions for optimal algorithms, *Journal of Computational Physics*, *121*, 357 – 372, 1995. (cited at page: 12)

Balsara, D. S., and C.-W. Shu, Monotonicity preserving weighted essentially non-oscillatory schemes with increasingly high order of accuracy, *Journal of Computational Physics*, *160*, 405 – 452, 2000. (cited at page: 24)

Barth, T., and P. Frederickson, Higher order solution of the Euler equations on unstructured grids using quadratic reconstruction, *AIAA paper no. 90-0013*, 1990. (cited at page: 24)

Bear, J., *Dynamics of Fluids in Porous Media*, Dover Books on Physics & Chemistry, Dover Publ., 1972. (cited at page: 65)

Bear, J., *Dynamics of Fluids in Porous Media*, Dover Books on Physics and Chemistry, Dover, 1988. (cited at pages: 4 and 5)

Belytschko, T., Y. Krongauz, J. Dolbow, and C. Gerlach, On the completeness of meshfree particle methods, *International Journal for Numerical Methods in Engineering*, *43*, 785–819, 1998. (cited at page: 11)

Ben Moussa, B., On the convergence of sph method for scalar conservation laws with boundary conditions, *Method Appl Anal*, *13*, 29–62, 2006. (cited at pages: 8 and 12)

Ben Moussa, B., N. Lanson, and J. Vila, On the convergence of sph method for scalar conservation laws with boundary conditions, *Int Ser Numer Math*, pp. 31–40, 1999. (cited at pages: 8, 100, and 108)

Boscheri, W., and M. Dumbser, Arbitrary–Lagrangian–Eulerian One–Step WENO Finite Volume Schemes on Unstructured Triangular Meshes, *Communications in Computational Physics*, *14*, 1174–1206, 2013a. (cited at page: 19)

Boscheri, W., and M. Dumbser, Arbitrary–Lagrangian–Eulerian One–Step WENO Finite Volume Schemes on Unstructured Triangular Meshes, *Communications in Computational Physics*, *14*, 1174–1206, 2013b. (cited at page: 13)

Boscheri, W., D. Balsara, and M. Dumbser, Lagrangian ADER-WENO Finite Volume Schemes on Unstructured Triangular Meshes Based On Genuinely Multidimensional HLL Riemann Solvers, *Journal of Computational Physics*, 2014, in press. DOI: 10.1016/j.jcp.2014.02.023. (cited at page: 13)

Boso, F., A. Bellin, and M. Dumbser, Numerical simulations of solute transport in highly heterogeneous formations: A comparison of alternative numerical schemes, *Advances in Water Resources*, *52*, 178 – 189, 2013. (cited at pages: 6, 11, 63, 64, 82, and 100)

Breitkopf, P., H. Naceur, A. Rassineux, and P. Villon, Moving least squares response surface approximation: Formulation and metal forming applications, *Computers & amp; Structures*, *83*, 1411 – 1428, 2005, advances in Meshfree Methods. (cited at page: 8)

Brookshaw, L., A method of calculating radiative heat diffusion in particle simulations, *Astronomical Society of Australia*, *6*, 207–210, 1985. (cited at pages: 63 and 65)

Chen, K. C., R. M. Ford, and P. T. Cummings, Mathematical models for motile bacterial transport in cylindrical tubes, *Journal of Theoretical Biology*, *195*, 481 – 504, 1998. (cited at pages: 3, 101, and 102)

Cheng, J., and C. Shu, A high order ENO conservative Lagrangian type scheme for the compressible Euler equations, *Journal of Computational Physics*, *227*, 1567–1596, 2007. (cited at page: 13)

Cleary, P. W., and J. J. Monaghan, Conduction modelling using smoothed particle hydrodynamics, *Journal of Computational Physics*, *148*, 227 – 264, 1999. (cited at pages: 11, 63, and 65)

Colagrossi, A., and M. Landrini, Numerical simulation of interfacial flows by smoothed particle hydrodynamics, *Journal of Computational Physics*, *191*, 448 – 475, 2003. (cited at pages: 11 and 12)

Deng, L., Y. Liu, W. Wang, W. Ge, and J. Li, A two-fluid smoothed particle hydrodynamics (tf-sph) method for gas-solid fluidization, *Chemical Engineering Science*, *99*, 89 – 101, 2013. (cited at page: 11)

Di Blasi, G., E. Francomano, A. Tortorici, and E. Toscano, A smoothed particle image reconstruction method, *Calcolo*, *48*, 61–74, 2011. (cited at page: 71)

Dilts, G. A., Moving-least-squares-particle hydrodynamicsâi. consistency and stability, *International Journal for Numerical Methods in Engineering*, *44*, 1115–1155, 1999. (cited at page: 12)

Duffy, K., R. Ford, and P. Cummings, Residence time calculation for chemotactic bacteria within porous media, *Biophysical Journal*, *73*, 2930–2936, 1997. (cited at page: 99)

Dumbser, M., Arbitrary high order PNPM schemes on unstructured meshes for the compressible Navier-Stokes equations, *Computers & Fluids*, *39*, 60–76, 2010a. (cited at page: 67)

Dumbser, M., Arbitrary high order {PNPM} schemes on unstructured meshes for the compressible navier-stokes equations, *Computers & Fluids*, *39*, 60 – 76, 2010b. (cited at page: 109)

Dumbser, M., and D. Balsara, High-order unstructured one-step PNPM chemes for the viscous and resistive mhd equations, *Computer Modeling in Engineering & Sciences*, *3*, 301–334, 2009. (cited at page: 67)

Dumbser, M., and W. Boscheri, High-order unstructured Lagrangian one–step WENO finite volume schemes for non–conservative hyperbolic systems: Applications to compressible multi–phase flows, *Computers and Fluids*, *86*, 405 – 432, 2013. (cited at page: 13)

Dumbser, M., and M. Kaëser, Arbitrary high order non-oscillatory finite volume schemes on unstructured meshes for linear hyperbolic systems, *Journal of Computational Physics*, *221*, 693–723, 2007. (cited at pages: 22, 24, 29, and 70)

Dumbser, M., and E. Toro, A simple extension of the osher riemann solver to non-conservative hyperbolic systems, *Journal of Scientific Computing*, *48*, 70–88, 2011a. (cited at pages: 9, 18, and 19)

Dumbser, M., and E. F. Toro, On universal Osher–type schemes for general nonlinear hyperbolic conservation laws, *Communications in Computational Physics*, *10*, 635–671, 2011b. (cited at pages: 18, 19, and 59)

Dumbser, M., M. Kaëser, V. A. Titarev, and E. F. Toro, Quadrature-free non-oscillatory finite volume schemes on unstructured meshes for nonlinear hyperbolic systems, *Journal* *of Computational Physics*, *226*, 204 – 243, 2007. (cited at pages: 8, 22, 24, 29, 59, 61, and 70)

Dumbser, M., D. S. Balsara, E. F. Toro, and C.-D. Munz, A unified framework for the construction of one-step finite volume and discontinuous galerkin schemes on unstructured meshes, *Journal of Computational Physics*, *227*, 8209 – 8253, 2008a. (cited at pages: 8, 24, 59, 61, 70, and 109)

Dumbser, M., C. Enaux, and E. F. Toro, Finite volume schemes of very high order of accuracy for stiff hyperbolic balance laws, *Journal of Computational Physics*, *227*, 3971 – 4001, 2008b. (cited at pages: 8, 24, 59, 61, and 70)

Eisenbach, M., and J. Lengeler, *Chemotaxis*, Imperial College Press, 2004. (cited at page: 1)

Ellero, M., *IUTAM Symposium on Advances in Micro- and Nanofluidics: Proceedings of the IUTAM Symposium on Advances in Micro- and Nanofluidics, Dresden, Germany, September 6-8, 2007*, IUTAM bookseries, Springer, 2009. (cited at page: 11)

Ellero, M., M. Serrano, and P. Español, Incompressible smoothed particle hydrodynamics, *J. Comput. Phys.*, *226*, 1731–1752, 2007. (cited at page: 12)

Engelmann, T., Neue methode zur untersuchung der sauerstoffaussheidung pflanzlicher und thierischer organismen, *Pflugers Arch. Gesamte Physiol. Menschen Tiere*, *25*, 285–292, 1881. (cited at page: 1)

Erban, R., Hans, and G. Othmer, From individual to collective behavior in bacterial chemotaxis, *SIAM J Appl Math*, pp. 361–391, 2004. (cited at pages: 99 and 113)

Español, P., and M. Revenga, Smoothed dissipative particle dynamics, *Phys. Rev. E*, *67*, 026,705, 2003. (cited at pages: 11, 63, 65, and 103)

Fang, J., A. Parriaux, M. Rentschler, and C. Ancey, Improved {SPH} methods for simulating free surface flows of viscous fluids, *Applied Numerical Mathematics*, *59*, 251 – 271, 2009. (cited at page: 11)

Ferrari, A., M. Dumbser, E. F. Toro, and A. Armanini, A new 3d parallel sph scheme for free surface flows, *Computers & Fluids*, *38*, 1203 – 1217, 2009. (cited at pages: 11, 12, 13, 16, 23, 27, 63, 65, 66, 104, 109, and 112)

Ford, R., and R. Harvey, Role of chemotaxis in the transport of bacteria through saturated porous media, *Advances in Water Resources*, *30*, 1608–1617, 2007a. (cited at pages: 99, 102, and 113)

Ford, R. M., and R. W. Harvey, Role of chemotaxis in the transport of bacteria through saturated porous media, *Advances in Water Resources*, *30*, 1608 – 1617, 2007b. (cited at pages: 3 and 6)

Friedrich, O., Weighted essentially non-oscillatory schemes for the interpolation of mean values on unstructured grids, *Journal of Computational Physics*, *144*, 194 – 212, 1998. (cited at page: 22)

Frymier, P. D., and R. M. Ford, Analysis of bacterial swimming speed approaching a solid-liquid interface, *AIChE Journal*, *43*, 1341–1347, 1997. (cited at page: 102)

Gassner, G., F. LÃ¶rcher, and C.-D. Munz, A contribution to the construction of diffusion fluxes for finite volume and discontinuous galerkin schemes, *Journal of Computational Physics*, *224*, 1049 – 1063, 2007. (cited at page: 67)

Gholami, B., A. Comerford, and M. Ellero, A multiscale SPH particle model of the near-wall dynamics of leukocytes in flow, *International Journal for Numerical Methods in Biomedical Engineering*, pp. n/a–n/a, 2013. (cited at page: 11)

Gingold, R. A., and J. J. Monaghan, Smoothed particle hydrodynamics - Theory and application to non-spherical stars, *Mon. Not. Roy. Astron. Soc.*, *181*, 375–389, 1977. (cited at pages: 11, 12, 15, and 63)

Gottlieb, S., and C. wang Shu, Total variation diminishing runge-kutta schemes, *Math. Comp*, *67*, 73–85, 1998. (cited at page: 27)

Herrera, P., Particle and streamline numerical methods for conservative and reactive transport simulations in porous media, Ph.D. thesis, University of British Columbia, 2009. (cited at pages: 5, 63, and 83)

Herrera, P. A., and R. D. Beckie, An assessment of particle methods for approximating anisotropic dispersion, *International Journal for Numerical Methods in Fluids*, pp. n/a–n/a, 2012. (cited at pages: 63, 65, 71, 72, 82, 83, and 85)

Herrera, P. A., M. Massabó, and R. D. Beckie, A meshless method to simulate solute transport in heterogeneous porous media, *Advances in Water Resources*, *32*, 413 – 429, 2009. (cited at pages: ix, 6, 7, 11, 63, 65, 66, 100, 103, and 105)

Herrera, P. A., A. J. Valocchi, and R. D. Beckie, A multidimensional streamline-based method to simulate reactive solute transport in heterogeneous porous media, *Advances in Water Resources*, *33*, 711 – 727, 2010. (cited at pages: 6, 11, 63, and 100)

Hidalgo, A., and M. Dumbser, Ader schemes for nonlinear systems of stiff advection-diffusion-reaction equations, *Journal of Scientific Computing*, *48*, 173–189, 2011. (cited at pages: 67 and 109)

Hockney, R., and J. Eastwood, *Computer Simulation Using Particles*, McGraw Hill, New York, 1981. (cited at page: 23)

Hu, C., and C.-W. Shu, Weighted essentially non-oscillatory schemes on triangular meshes, *Journal of Computational Physics*, *150*, 97 – 127, 1999. (cited at pages: 22 and 24)

Hu, X., and N. Adams, A multi-phase {SPH} method for macroscopic and mesoscopic flows, *Journal of Computational Physics*, *213*, 844 – 861, 2006. (cited at page: 11)

Hu, X., and N. Adams, A constant-density approach for incompressible multi-phase {SPH}, *Journal of Computational Physics*, *228*, 2082 – 2091, 2009. (cited at page: 12)

Ibragimov, A. I., C. J. McNeal, L. R. Ritter, and J. R. Walton, A mathematical model of atherogenesis as an inflammatory response, *Mathematical Medicine and Biology*, *22*, 305–333, 2005. (cited at page: 1)

Inutsuka, S.-i., Reformulation of smoothed particle hydrodynamics with riemann solver, *Journal of Computational Physics*, *179*, 238 – 267, 2002. (cited at page: 13)

Javandel, I., C. Doughty, and C. Tsang, *Groundwater Transport: Handbook of Mathematical Models*, Groundwater Transport: Handbook of Mathematical Models, Wiley, 1984. (cited at page: 83)

Jiang, G.-S., and C.-W. Shu, Efficient implementation of weighted eno schemes, *Journal of Computational Physics*, *126*, 202 – 228, 1996. (cited at pages: 22, 24, and 25)

Johnson, G., and S. Beissel, Normalized smoothing functions for sph impact computations, *International Journal for Numerical Methods in Engineering*, *39*, 2725–2741, 1996. (cited at page: 11)

Käser, M., and A. Iske, ADER Schemes on Adaptive Triangular Meshes for Scalar Conservation Laws, *Journal of Computational Physics*, *205*, 486–508, 2005. (cited at page: 22)

Keller, E. F., and L. A. Segel, Model for chemotaxis, *Journal of Theoretical Biology*, *30*, 225 – 234, 1971a. (cited at pages: 2, 102, 113, and 126)

Keller, E. F., and L. A. Segel, Traveling bands of chemotactic bacteria: A theoretical analysis, *Journal of Theoretical Biology*, *30*, 235 – 248, 1971b. (cited at page: 102)

Kitanidis, P. K., 1994_Kitanidis_the concept_of_dilux_index.pdf, *Water Resources Research*, *30*, 2011–2026, 1994. (cited at pages: 82 and 121)

Le Borgne, T., M. Dentz, D. Bolster, J. Carrera, J.-R. de Dreuzy, and P. Davy, Non-Fickian mixing: Temporal evolution of the scalar dissipation rate in heterogeneous porous media, *Advances in Water Resources*, *33*, 1468–1475, 2010. (cited at page: 121)

Li, S., and W. Liu, *Meshfree Particle Methods*, Springer, 2004. (cited at page: 71)

Libersky, L., and A. Petschek, Smooth particle hydrodynamics with strength of materials, in *Advances in the Free-Lagrange Method Including Contributions on Adaptive Gridding and the Smooth Particle Hydrodynamics Method*, edited by H. Trease, M. Fritts, and W. Crowley, vol. 395 of *Lecture Notes in Physics*, pp. 248–257, Springer Berlin Heidelberg, 1991. (cited at page: 11)

Libersky, L. D., A. G. Petschek, T. C. Carney, J. R. Hipp, and F. A. Allahdadi, High strain lagrangian hydrodynamics: A three-dimensional sph code for dynamic material response, *Journal of Computational Physics*, *109*, 67 – 75, 1993. (cited at page: 11)

Liu, M., and G. Liu, Restoring particle consistency in smoothed particle hydrodynamics, *Applied Numerical Mathematics*, *56*, 19 – 36, 2006. (cited at pages: 12 and 72)

Liu, M., and G. Liu, Smoothed particle hydrodynamics (sph): an overview andÂ recent developments, *Archives of Computational Methods in Engineering*, *17*, 25–76, 2010. (cited at pages: 11, 12, and 71)

Liu, M., G. Liu, and K. Lam, A one-dimensional meshfree particle formulation for simulating shock waves, *Shock Waves*, *13*, 201–211, 2003a. (cited at pages: 11 and 33)

Liu, M. B., G. R. Liu, K. Y. Lam, and Z. Zong, Smoothed particle hydrodynamics for numerical simulation of underwater explosion, *Computational Mechanics*, *30*, 106–118, 2003b. (cited at page: 11)

Liu, W., J. Cheng, and C. Shu, High order conservative Lagrangian schemes with Lax-Wendroff type time discretization for the compressible Euler equations, *Journal of Computational Physics*, *228*, 8872–8891, 2009. (cited at page: 13)

Liu, W. K., S. Jun, and Y. F. Zhang, Reproducing kernel particle methods, *International Journal for Numerical Methods in Fluids*, *20*, 1081–1106, 1995. (cited at page: 12)

Long, T., and R. M. Ford, Enhanced transverse migration of bacteria by chemotaxis in a porous T-sensor., *Environmental science technology*, *43*, 1546–1552, 2009. (cited at pages: 1, 2, 6, 99, 103, 105, and 116)

Long, W., and M. Hilpert, Analytical solutions for bacterial energy taxis (chemotaxis): Traveling bacterial bands, *Advances in Water Resources*, *30*, 2262 – 2270, 2007. (cited at page: 113)

Long, W., and M. Hilpert, Lattice-boltzmann modeling of contaminant degradation by chemotactic bacteria: Exploring the formation and movement of bacterial bands, *Water Resour. Res.*, *44*, 0043–1397, 2008. (cited at page: 2)

Lucy, L., A numerical approach to the testing of the fission hypothesis, *Astronomical Journal*, *82*, 1013–1024, 1977. (cited at pages: 11 and 63)

Luo, J., M. Dentz, J. Carrera, and P. Kitanidis, Effective reaction parameters for mixing controlled reactions in heterogeneous media, *Water Resources Research*, *44*, n/a–n/a, 2008. (cited at page: 5)

Mesibov R., O. G. W., and A. Adler, The range of attractant concentrations for bacterial chemotaxis and the threshold and size of response over this range, *J Gen Physiol.*, *62*, 203–223, 1973. (cited at page: 1)

Monaghan, J., Smoothed particle hydrodynamics, *Annu. Rev. Astron. AStrophys.*, *30*, 543–574, 1992. (cited at page: 23)

Monaghan, J., Sph without a tensile instability, *Journal of Computational Physics*, *159*, 290 – 311, 2000. (cited at page: 12)

Monaghan, J. J., Simulating free surface flows with sph, *Journal of Computational Physics*, *110*, 399–406, 1994. (cited at pages: 11, 16, 23, and 63)

Monaghan, J. J., Smoothed particle hydrodynamics, *Reports on Progress in Physics*, *68*, 1703, 2005. (cited at pages: 11, 12, 16, 23, 27, 33, 63, 65, and 66)

Monaghan, J. J., Smoothed Particle Hydrodynamics and Its Diverse Applications, *Annual Review of Fluid Mechanics*, *44*, 323–346, 2012. (cited at pages: 6 and 11)

Murphy, E. M., and T. R. Ginn, Modeling microbial processes in porous media, *Hydrogeology Journal*, *8*, 142–158, 2000. (cited at page: 4)

Nakshatrala, K. B., M. K. Mudunuru, and A. J. Valocchi, A numerical framework for diffusion-controlled bimolecular-reactive systems to enforce maximum principles and the non-negative constraint, pp. 1–57. (cited at page: 92)

Obi, E.-O., and M. J. Blunt, Streamline-based simulation of advective dispersive solute transport, *Advances in Water Resources*, *27*, 913–924, 2004. (cited at page: 63)

Odell, G., and E. Keller, Traveling bands of chemotactic bacteria revisited, *Journal of Theoretical Biology*, *56*, 243 – 247, 1976. (cited at page: 102)

Olson, M., *Quantification of Bacterial Motility and Chemotaxis in Porous Media Using Magnetic Resonance Imaging (MRI)*, University of Virginia, 2004. (cited at page: 1)

Pedit, J. A., R. B. Marx, C. T. Miller, and M. D. Aitken, Quantitative analysis of experiments on bacterial chemotaxis to naphthalene, *Biotechnology and Bioengineering*, *78*, 626–634, 2002. (cited at pages: 99 and 114)

Pfeffer, W., *Über chemotaktische Bewegungen von Bacterien Flagellaten und Volvocineen*, Untersuch. Bot., Inst. Tubingen, 1887. (cited at pages: ix, 1, and 2)

Porter, M. L., F. J. Valdés-Parada, and B. D. Wood, Multiscale modeling of chemotaxis in homogeneous porous media, *Water Resources Research*, *47*, n/a–n/a, 2011. (cited at pages: 4, 5, and 99)

Press, W. H., B. P. Flannery, S. A. Teukolsky, and W. T. Vetterling, *Numerical Recipes in Fortran: The Art of Scientific Computing*, 2 ed., Cambridge University Press, 1992. (cited at page: 114)

Puri, K., and P. Ramachandran, A comparison of {SPH} schemes for the compressible euler equations, *Journal of Computational Physics*, *256*, 308 – 333, 2014. (cited at page: 13)

Renaut, g.-a., J.-C. Marongiu, J. Leduc, and F. Leboeuf, On the high-order reconstruction for Meshfree Particle Methods in Numerical Flow Simulation, in *2nd ECCOMAS Young Investigators Conference (YIC 2013)*, Bordeaux, France, 2013, in this work, we extend SPH-ALE schemes to high-order. (cited at page: 13)

Rivero, M. A., R. T. Tranquillo, H. M. Buettner, and D. A. Lauffenburger, Transport models for chemotactic cell populations based on individual cell behavior, *Chemical Engineering Science*, *44*, 2881 – 2897, 1989. (cited at pages: ix, 3, 99, 100, 101, and 126)

Roussos, E. T., J. S. Condeelis, and A. Patsialou, Chemotaxis in cancer, *Nature Reviews Cancer*, *11*, 573–587, 2011. (cited at page: 1)

Salamon, P., D. Fernandez-Garcia, and J. J. Gomez-Hernandez, A review and numerical assessment of the random walk particle tracking method, *Journal of Contaminant Hydrology*, *87*, 277–305, 2006. (cited at page: 65)

Segev, R., and E. Ben-Jacob, Generic modeling of chemotactic based self-wiring of neural networks, *Neural Networks*, *13*, 185 – 199, 2000. (cited at page: 1)

Serini, G., D. Ambrosi, E. Giraudo, A. Gamba, L. Preziosi, and F. Bussolino, Modeling the early stages of vascular network assembly, *The EMBO Journal*, *22*, 1771–1779, 2003. (cited at page: 1)

Sod, G., Survey of several finite difference methods for systems of nonlinear hyperbolic conservation laws, *Journal Name: J. Comput. Phys.*, 1978. (cited at pages: 9 and 37)

Srinivasan, G., D. Tartakovsky, M. Dentz, H. Viswanathan, B. Berkowitz, and B. Robinson, Random walk particle tracking simulations of non-fickian transport in heterogeneous media, *Journal of Computational Physics*, *229*, 4304 – 4314, 2010. (cited at page: 65)

Steefel, C. I., D. J. DePaolo, and P. C. Lichtner, Reactive transport modeling: An essential tool and a new research approach for the earth sciences, *Earth and Planetary Science Letters*, *240*, 539 – 558, 2005. (cited at page: 4)

Sudicky, E. A., A natural gradient experiment on solute transport in a sand aquifer: Spatial variability of hydraulic conductivity and its role in the dispersion process, *Water Resources Research*, *22*, 2069–2082, 1986. (cited at page: 6)

Swegle, J., D. Hicks, and S. Attaway, Smoothed particle hydrodynamics stability analysis, *Journal of Computational Physics*, *116*, 123 – 134, 1995. (cited at page: 11)

Tartakovsky, A. M., P. Meakin, T. D. Scheibe, and B. D. Wood, A smoothed particle hydrodynamics model for reactive transport and mineral precipitation in porous and fractured porous media, *Water Resour. Res.*, *43*, W05,437, 2007. (cited at page: 63)

Tindall, M., P. Maini, S. Porter, and J. Armitage, Overview of mathematical approaches used to model bacterial chemotaxis ii: Bacterial populations, *Bulletin of Mathematical Biology*, *70*, 1570–1607, 2008, 10.1007/s11538-008-9322-5. (cited at page: 1)

Tindalla, M., S. Porterb, P. Mainia, G. Gagliaa, and J. Armitageb, Overview of mathematical approaches used to model bacterial chemotaxis i: The single cell, *Bulletin of Mathematical Biology*, pp. 1525–1569, 2008. (cited at page: 2)

Titarev, V., and E. Toro, Finite-volume {WENO} schemes for three-dimensional conservation laws, *Journal of Computational Physics*, *201*, 238 – 260, 2004. (cited at page: 25)

Titarev, V., and E. Toro, ADER schemes for three-dimensional nonlinear hyperbolic systems, *Journal of Computational Physics*, *204*, 715–736, 2005. (cited at pages: 59 and 61)

Titarev, V., P. Tsoutsanis, and D. Drikakis, WENO schemes for mixed–element unstructured meshes, *Communications in Computational Physics*, *8*, 585–609, 2010. (cited at page: 24)

Tompson, A., Numerical simulation of chemical migration in physically and chemically heterogeneous porous media, *Water Resour. Res.*, *29*, 3709–3726, 1993. (cited at page: 63)

Toro, E., *Riemann solvers and numerical methods for fluid dynamics: a practical introduction*, Springer, 1997. (cited at pages: 8, 9, 14, 18, 37, and 59)

Tsoutsanis, P., V. Titarev, and D. Drikakis, WENO schemes on arbitrary mixed-element unstructured meshes in three space dimensions, *Journal of Computational Physics*, *230*, 1585–1601, 2011. (cited at page: 24)

Valdés-Parada, F. J., M. L. Porter, K. Narayanaswamy, R. M. Ford, and B. D. Wood, Upscaling microbial chemotaxis in porous media, *Advances in Water Resources*, *32*, 1413 – 1428, 2009a. (cited at pages: 99, 102, and 103)

Valdés-Parada, F. J., M. L. Porter, K. Narayanaswamy, R. M. Ford, and B. D. Wood, Upscaling microbial chemotaxis in porous media, *Advances in Water Resources*, *32*, 1413 – 1428, 2009b. (cited at pages: 2, 3, 4, 5, and 6)

Vauez-Quesada, A., M. Ellero, and E. Pep, A sph-based particle model for computational microrheology, *Microfluidics and Nanofluidics*, *13*, 249–260, 2012. (cited at page: 11)

Vignjevic, R., and J. Campbell, Review of development of the smooth particle hydrodynamics (sph) method, in *Predictive Modeling of Dynamic Processes*, edited by S. Hiermaier, pp. 367–396, Springer, 2009. (cited at page: 11)

Vila, J. P., On particle weighted methods and smooth particle hydrodynamics, *Mathematical Models and Methods in Applied Sciences*, *09*, 161–209, 1999. (cited at pages: 12, 17, 18, 100, and 108)

Wang, M., and R. Ford, Transverse bacterial migration induced by chemotaxis in a packed column with structured physical heterogeneity, *Environ. Sci. Technol.*, *43*, 5921–5927, 2009. (cited at pages: 1, 2, 6, 99, 120, and 126)

Wang, M., R. Ford, and H. Ronald, Coupled effect of chemotaxis and growth on microbial distributions in organic-amended aquifer sediments: Observations from laboratory and field studies, *Environ. Sci. Technol.*, *42*, 3556–3562, 2008. (cited at pages: 2 and 6)

Ward, S., Chemotaxis by the nematode caenorhabditis elegans: Identification of attractants and analysis of the response by use of mutants, *Proc. Natl. Acad. Sci.*, *70*, 817–821, 1973. (cited at page: 1)

Whitaker, S., *The Method of Volume Averaging*, Theory and Applications of Transport in Porous Media, Kluwer Academic, 1999. (cited at page: 4)

Xu, F., Y. Zhao, R. Yan, and T. Furukawa, Multidimensional discontinuous sph method and its application to metal penetration analysis, *International Journal for Numerical Methods in Engineering*, *93*, 1125–1146, 2013. (cited at page: 33)

Xu, R., P. Stansby, and D. Laurence, Accuracy and stability in incompressible {SPH} (isph) based on the projection method and a new approach, *Journal of Computational Physics*, *228*, 6703 – 6725, 2009. (cited at page: 12)

Xueying, Z., T. Haiyan, K. Leihsin, and W. Chen, A contact sph method with high-order limiters for simulation of inviscid compressible flows, *Commun. Comput. Phys.*, *14*, 2013. (cited at page: 13)

Zhang, G. M., and R. C. Batra, Modified smoothed particle hydrodynamics method and its application to transient problems, *Computational Mechanics*, *34*, 137–146, 2004. (cited at page: 12)

Zhu, Y., and P. Fox, Smoothed particle hydrodynamics model for diffusion through porous media, *Transport in Porous Media*, *43*, 441–471, 2001. (cited at page: 63)

Zhu, Y., and P. J. Fox, Simulation of pore-scale dispersion in periodic porous media using smoothed particle hydrodynamics, *Journal of Computational Physics*, *182*, 622 – 645, 2002. (cited at page: 63)

Zimmera, R. K., and J. A. Riffellc, Sperm chemotaxis, fluid shear, and the evolution of sexual reproduction, *PNAS*, *108*, 2011. (cited at page: 1)

Zuckerman, B. M., and H. B. Jansson, Nematode chemotaxis and possible mechanisms of host/prey recognition., *Annual Review of Phytopathology*, *22*, 95–113, 1984. (cited at page: 1)

Zwillinger, D., *CRC Standard Mathematical Tables and Formulae: Editor-in-chief, Daniel Zwillinger*, CRC Standard Mathematical Tables and Formulae, Taylor & Francis Group, 2003. (cited at page: 69)

Acknowledgments

I deeply thank my supervisors, Prof Alberto Bellin and Prof. Michael Dumbser. ’*You have kept my course true and steady*’. Thank you for having introduced me to the stimulating world of scientific research.

I would like to thank Paulo Andres Herrera Ricci for the stimulating discussions and for the kind during a research period I spent in Santiago.

I warm thanks friends and colleagues from the Department of Civil, Environmental and Mechanical Engineering of the University of Trento.

I also thank all opensource community who donate their time to the creation of free software (as free speech) to made the world a better place where to live.

Specil thank to MCF Trento.

I wish to endless thank my family for all the sacrifices made to allow me to pursue my dreams.